Microfabricated Electromagnetic Flap Actuators And Their Applications

Thesis by
Raanan A. Miller

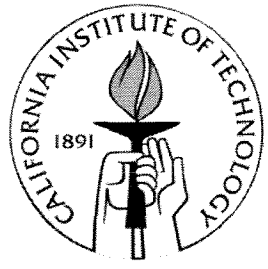

In Partial Fulfillment of the Requirements
for the Degree of Doctor of Philosophy

California Institute of Technology
Pasadena, California

1997

Approved:

.....

Chairman, date

.....

.....

.....

Acknowledgments

I would like to thank my advisor, Professor Yu-Chong Tai, for his guidance and support during my study at Caltech and for his help in overcoming the daunting challenges of doing research. The opportunity to work and learn within his group of talented students, and to observe the high quality standards he demands has been invaluable.

I wish to thank Dr. Geoffrey Burr, Greg Billock and their advisor Dr. Demetri Psaltis for their assistance with the holographic data storage experiments and for many hours spent performing the holographic storage measurements. I would also like to thank Dr. Romney R. Katti for his help and time spent educating me in the field of magnetics.

I thank the fellow members of my group for the assistance and support they provided me over the years. I would like to thank John Wright for his advice, frustration relieving discussions and for proofreading parts of this thesis. I also thank Thomas Tsao who proofread some of this manuscript, Fukang Jiang, Amish Desai, Xing Yang, Wen Hsieh, Charles Grojean who patiently answered my annoying computer questions, Mr. Shuyun Wu, Dr. Chang Liu, and Ken Walsh who at a moments notice was willing to help take some photographs.

I am grateful to Mr. Trevor Roper on whom I could always depend for help in repairing urgently needed equipment and for his politic advice.

I would like to thank my wife, Olga Miller, for her constant encouragement, patience, and support. I am also indebted to her for proofreading this complete manuscript.

Raanan A. Miller
Doctor of Philosophy in Electrical Engineering
California Institute of Technology

Abstract

In this thesis, a new technology which successfully combines silicon bulk micromachining with the electroplating of metal conductors and magnetic materials is presented. This technology has enabled the fabrication of the first bulk micromachined electromagnetic flap actuators. The demonstrated characteristics of these actuators are large size (> 16 mm^2), large forces (> 100 μN), and large (> 60 degrees) deflections. In this technology, silicon bulk micromachining is used to form the mechanical structures of the actuators, and the electroplating of copper and ferromagnetic permalloy provides the electromagnetic actuating components.

The developed actuators are configured in the shape of a flap, consisting of a single crystal silicon plate and on-plate electromagnetic components. The silicon plate, 4 mm × 4 mm × 40 μm, is connected to a substrate via several silicon springs. When the electromagnetic components are activated the silicon plate flaps up and down similar to a butterfly wing. Three types of actuators have been examined and they differ in electromagnetic components. Type-1 actuators have a permalloy layer, the type-2 actuators have copper coils, and the type-3 actuators have both the permalloy and copper coils. The actuators are operated in the presence of an externally applied magnetic field, and the deflections of the flap actuators can be controlled either by varying the external magnetic field strength or by changing the current to the copper coils.

The electromagnetically induced deflections of the actuators are measured and agree well with the design using a combined electromagnetic/mechanical model. Achieved

deflection angles of the type-1 actuators exceed 60 ° at an applied field of around 80 KA/m (1000 gauss). Additional deflection angles of about ± 20 degrees (type-3 actuator) can also be obtained by coil currents of ± 100 mA. As a result, large deflections up to 80 °, together with a large force exceeding 100 μN, have been achieved in the micro devices. Moreover, we have successfully demonstrated these actuators in two applications for scanning mirrors for holographic data storage systems and fiber optic bypass switches. Using the actuators as scanning mirrors, we have demonstrated initial storage of several hundred holograms in a photosensitive crystal. The fiber optic bypass switches using the MEMS flap actuator have much better mechanical performance and lower power consumption when compared to a commercial (Di-Con) fiber optic bypass switch.

Table of contents

List of figures

List of Tables

Chapter 1

Introduction

1.1 Microfabricated MEMS actuators

Silicon micromachining allows the microfabrication of three-dimensional electro-mechanical structures with typical length scales in the micrometer to millimeter range, using technologies similar to those for integrated circuits. Hystorically, silicon micromachining has been divided into two categories; surface and bulk micromachining. Surface micromachining involves the deposition and patterning of successive layers of thin-film material on the surface of a substrate, usually a single crystal silicon wafer. Bulk micromachining, on the other hand, is the microfabrication of mechanical structures directly from the (silicon) substrate by removing undesired silicon. These three-dimensional electro-mechanical structures have many applications for sensors or actuators and when integrated with electronics, produce novel Micro-Electro-Mechanical Systems (MEMS).

An actuator is a device that outputs force and displacement. Common examples of actuators are pumps and motors. For many applications, such as pumps for micro-dose drug delivery, it is desirable for the device to have small physical size for reasons such as ease of use and low power consumption. Conventional actuators, however, are large in size ($> 1\ cm^3$), and often, even if available, small actuators are very expensive.

Therefore, it is believed that silicon micromachining has a unique potential to build actuators down to the micron scale, in large volume and at low cost. Also, because these actuators are fabricated using integrated circuit compatible techniques, they can be integrated with sensors and electronics to form more useful micro-electro-mechanical systems. In these MEMS systems, the electronics receives inputs from the sensors, provides the controlling logic, and sends instructions to the actuators to perform delicate physical tasks.

Research in the field of MEMS actuators started just under ten years ago since both the technology and operation requirements for the actuators are more challenging than MEMS sensors or electronics [1]. The technological challenges are in two areas. The first is to develop actuating mechanisms, including materials and processes which will produce the forces to move the actuators. The second is to integrate these actuating mechanisms into the mechanical structures of the actuators. The challenge then is to ensure that these actuators meet the operating requirements. This means that they have to not only operate in a reliable and repeatable manner, but also be capable of withstanding substantial shock while still providing the specified range of motion without degradation from fatigue or friction.

Today the two most common forms of actuation for MEMS actuators are electrostatic and piezoelectric. Electrostatic actuation is widely used because the electrostatic actuation technology is relatively simple, and has readily enabled the integration of actuators, sensors and electronics on one chip. The actuating principle for the electrostatic actuators is based on Coulomb force, which is produced when an electrical potential difference exists between two parallel conducting plates separated by a gap. This force attracts one plate to the other. In electrostatic actuators these plates are formed by either shaping the bulk silicon or by depositing layers of polysilicon or aluminum. Electrostatic actuators were first developed in the late 1980's and are now sold in commercial products. Among the first electrostatic MEMS actuators developed were micro-motors (1987) [2,3] and comb-drive electrostatic actuators which used polysilicon as the structural material (1989) [4]. In 1996 a micro-mirror array for image projection

developed by Texas Instruments went on the market [5]. While electrostatic actuation is a convenient form of actuation, electrostatic actuators are limited in the amount of force they can produce, and the distance over which this force acts. Typically they deliver forces of less than 10 μN, and produce displacements that are at most tens of microns.

Piezoelectric actuators are the second most common type of MEMS actuators. This type of actuation was investigated for MEMS because the piezoelectric technology has been so successfully used in macro devices. For MEMS piezoelectric devices, however, the piezoelectric material is made into thin-films. When metal electrodes are placed on either side of a piezoelectric dielectric to form a capacitor and subjected to a mechanical stress, the dielectric will generate electric charges, resulting in a voltage across the capacitor. The piezoelectric effect is a reversible phenomenon, which means that applying voltage across the dielectric can produce mechanical stresses (or strains) which can be used to actuate the MEMS devices. Only some dielectric materials are piezoelectric, such as PZT, ZnO, and quartz [6]. Applications of piezoelectric actuators include crystal oscillators, MEMS accelerometers [7], surface acoustic wave generators (SAWs) [8] and bimorph actuators [9]. Piezoelectric actuators typically can produce larger forces than electrostatic actuators at the cost of having only small displacements, or they can generate large deflections but with small forces. The typical displacements for piezoelectric stacks are several microns, but the forces can be as large as mN. If the actuators are configured as bimorphs, large deflections can be produced (greater than 100 μm) but the amount of force generated is very small (in the low μN range) [10]. Piezoelectric technology is more complex than electrostatic technology, but larger actuator deflections can be produced.

1.2 Electromagnetic actuation and electromagnetic actuators

Electromagnetic actuation for MEMS has only recently become the focus of attention in the micromachining community, as it offers many advantages over both electrostatic and piezoelectric actuations. Electromagnetic actuation in MEMS can produce both attractive and repulsive forces which are greater than 100 μN over long ranges (several millimeters) and capable of producing large deflections exceeding 100 μm. At the same time these MEMS electromagnetic actuators can still be integrated with electronics and sensors.

Electromagnetic actuation (reviewed in chapter 2) is produced by the interaction of magnetic fields with either magnetized materials or current-carrying conductors. In the macro world, electromagnetic actuation is one of the most commonly used forms of actuation because of its high efficiency and large power output. Examples of macro-actuators include pumps, motors, solenoids, and relays. For many applications it is desirable to have these actuators miniaturized. However, a mature technology required to make viable micro-electromagnetic actuators has been lacking. A new technology that combines MEMS technology and electromagnetic technology to make micro-electromagnetic actuators then is very attractive.

Previously, there have been some efforts on new micro-electromagnetic technologies and devices, but these demonstrations are limited to surface-micromachining. Examples include nickel linear-actuators and magnetic micromotors [11,12,13,14], polysilicon beams coated with permalloy [15], and thin-film permalloy magnetic flaps [16].

1.3 Electromagnetic MEMS flap actuators

This thesis then presents the first bulk-micromachined electromagnetic MEMS flap actuators and their enabling technology. The mechanical structure of these actuators is formed by selectively removing silicon from a silicon wafer using bulk micromachining techniques, while the electromagnetic components are subsequently added on by electroplating of metals on the micromachined actuator structure. Electroplated materials include copper to form electrical components and permalloy (a nickel/iron alloy) to form the magnetic components. Three types of MEMS flap actuators categorized according to their electromagnetic actuating components have been studied. The first type of actuators (type-1) use only a permalloy layer for actuation. This layer is located on a movable silicon plate which is connected by springs to the bulk silicon (i.e., substrate). In the second type (type-2) of actuator only copper coils are on the plate. The third type (type-3) of actuators then combine both the permalloy layer and copper coils. Photographs of the type-2 and the type-3 actuators are shown in Figures 1-1 and 1-2. It will be shown later that our electromagnetic actuator designs allow large rotation greater than 60 degrees for the type-1 & 3 actuators and displacement exceeding 200 μm with forces greater than 100 μN. Mechanically, the fabricated actuators are also thicker and stronger compared to the surface-micromachined actuators because of the use of single crystal silicon.

The MEMS flap actuators are also amongst the largest MEMS actuators (top view size) fabricated to date. All actuators, except some of the type-2, have a single crystal silicon plate, that is 4 mm wide, 4 mm long, and 30 - 40 microns thick. In the case for some large type-2 actuators, the silicon plate is 4 mm wide, 8 mm long and 30 microns thick. The silicon plate is connected to a silicon support via silicon springs. On the plate then are the electromagnetic components and they are used to control the plate's deflection when the device is in an applied magnetic field.

In fact, the possible large actuator size from this newly developed technology fulfills some needs for millimeter-sized actuators. For example, two applications to which we apply the MEMS flap actuators are described in this thesis and they are laser beam scanners and fiber-optic bypass switches.

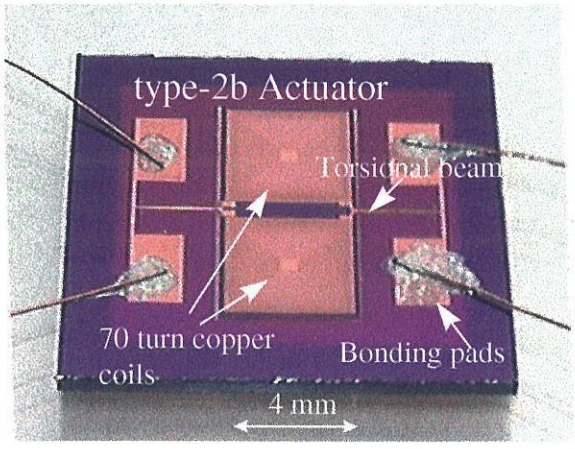

Figure 1-1: Photograph of a MEMS type-2 actuator. The plate shown in the center of the photograph is 4 mm x 8 mm x 30 μm.

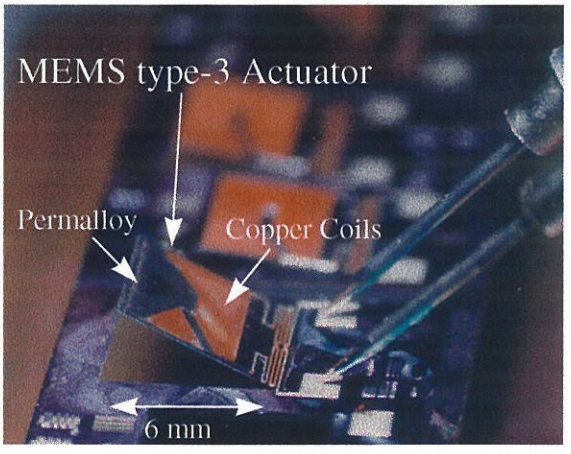

Figure 1-2: Photograph of a type-3 MEMS actuator.

1.4 Overview

In chapter 2, a brief review of magnetostatics and a discussion of the magnetization process for ferromagnetic materials is given. In chapter 3 we describe the technology required to fabricate the electromagnetic flap actuators. This includes the electromagnetic actuating components (electroplated copper, permalloy, and insulators) and the bulk silicon micromachining techniques. In chapter 4 the various actuators that have been fabricated are presented including their fabrication processes. In chapter 5 we investigate the actuators' electromagnetic operation. This includes the deflections of the actuators in response to externally applied magnetic fields and modelling. Finally, chapter 6 describes two applications of the actuators, as scanning mirrors for holographic data storage and fiber-optic bypass switches.

References

[1] H. Fujita, " Future of Actuators and Microsystems," *Sensors and Actuators,* A 5, pp. 105-111, 1996.

[2] W. S. N. Trimmer and K.J.Gabriel, " Design considerations for a practical electrostatic micromotor," *Sensors and Actuators*, A 11, pp. 189 - 206, 1987.

[3] L. S. Fan, Y.C. Tai, and R. S. Muller, " IC-processed Electrostatic Micromotors," *Sensors and Actuators*, A 20, pp. 41-47, 1989.

[4] W. C. Tang, T.-C.H. Nguyen, and R.T. Howe, " Laterally Driven Polysilicon Resonant Microstructures," *Sensors and Actuators*, A 20, pp. 25 - 31, 1989.

[5] E. H. Chiu, C. Tran, T. Honzawa, and S. Numaga, " Design and Implementation of a 525 mm^2 CMOS Digital Micromirror Device (DMD) Display Chip," *IEEE VLSI Conference*, May 1995.

[6] J. Fraden, *AIP Handbook of modern sensors: physics, designs and applications*, American Institute of Physics, New York, 1993.

[7] P.T Moseley and A.J. Crockor, *Sensor Materials*, Institute of Physics publishing, Bristol, 1996, pp. 119-133.

[8] T. G. King and M. E. Peterson et al., " Piezoelectric ceramic actuators: a review of machinery applications," *Precision Engineering*, Vol. 12 (3), pp. 131-135, 1990.

[9] D. J. Peters and B. L. Blackford, " Piezoelectric Bimorph Based Translation Device for Two-Dimensional, Remote Micro Positioning," *Rev. Sci. Instrum.*, Vol. 60, pp. 138-140, 1989.

[10] J.G. Smits, S. I. Dalke, and T. K. Cooney, " The Constituent Equations of Piezoelectric Bimorphs," *Sensors and Actuators*, A 28, pp. 41-61, 1991.

[11] H. Guckel, T.R. Christenson, K.J. Skrobid, and T.S. Jung, " A First Functional Current Excited Planar Rotational Magnetic MicroMotor," *Proceedings, IEEE Micro Electro Mechanical Systems Meeting, MEMS'93*, pp.7-11, 1993.

[12] H. Guckel, T. R. Christenson, T. Earles, and J. Klein," Laterally Driven Electromagnetic Actuators," *Technical Digest, Solid-State Sensor and Actuator Workshop*, Hilton Head, SC, pp. 49-52, 1994.

[13] C.H. Ahn, Y. J. Kim, and M. G. Allen, " A Planar Variable Reluctance Magnetic Micromotor with Fully Integrated Stator and Wrapped Coils," *Proceedings, IEEE Micro Electro Mechanical Systems Meeting, MEMS'93*, pp. 1-6, 1993.

[14] B. Rogge, J. Schultz, J. Mohr, A. Thommes, and W. Menz, " Fully Batch Fabricated Magnetic Microactuators Using A Two Layer LIGA Process," *Proceedings, 8th International conference on Solid-state Sensors and Actuators, Transducers'95*, pp. 320-323, 1995.

[15] J.W. Judy, R.S. Muller, and H.H. Zappe, " Magnetic Microactuation of Polysilicon Flexure Structures," *Technical Digest, Solid-State Sensor and Actuator Workshop*, Hilton Head, SC, pp. 43-48, 1994.

[16] C. Liu, T. Tsao, Y.C. Tai e. al., *Proceedings, IEEE Micro Electro Mechanical Systems Meeting, MEMS'95*, pp. 7-12, 1995.

Chapter 2

Review of Magnetic Material and Magnetostatic Actuation

In this chapter we first review some of the basic concepts related to the magnetization of ferromagnetic materials, in particular permalloy which is the ferromagnetic material we use in our actuators. We also describe some of the equipment used to characterize the permalloy magnetic parameters. Finally, the review of magnetostatic actuation mechanisms is given. The purpose is to describe relations between magnetic forces and the magnetic moment of a ferromagnetic material in a magnetic field, and extend the discussion to current carrying coils.

2.1 Electromagnetic units

One quickly learns when working in electromagnetics that magnetic units can be very confusing. The following is a quotation from a panel discussion on units in magnetism held at the 1994 joint MMM-Intermag conference [1]. "The current practice regarding units in magnetism is a mess. Large fields are given in Teslas, small ones in gauss or

oersteds. Magnetic moments and susceptibility are given in emu...." As a result, one must be very familiar with both CGS and MKS units, and be able to switch between. To avoid confusion, the parameters and definitions presented in the following will be used throughout this thesis. These common electromagnetic parameters are described in Table 2.1 in both CGS and MKS units. Table 2.2 shows how to convert between the CGS and MKS systems.

Parameter	CGS units	MKS units
Magnetic flux density B (magnetic induction)	gauss $B = H + 4\pi M$	webers / meter ^{2} (Tesla) $B = \mu_o H + M$
Magnetic field strength H	oersteds	amperes / meter
Magnetization M	emu / cm ^{3}	webers / meter ^{2}
Magnetic moment m	emu	amperes-meter^2
Permeability (vacuum)	$\mu = 1$	$\mu_o = 4\pi$ x 10 $^{-7}$ weber / amper meter
Magnetic flux ϕ	maxwell	weber (1 volt-sec)

Table 2.1: Units of common magnetic parameters.

Parameter	CGS to MKS	MKS to CGS
B	1 gauss = 10 $^{-4}$ weber / meter ^{2}	1 weber / meter ^{2} = 10 ^{4} gauss
H	1 oersted = 79.6 amperes/ meter	1 ampere / meter = 12.57 x 10 $^{-3}$ oersted
M	1 emu/cm ^{3} = 12.57 x 10^{-4} weber/meter ^{2}	1 weber / meter ^{2} = 796 emu/cm ^{3}
ϕ	1 maxwell = 10 $^{-8}$ weber	1 weber = 10 ^{8} maxwells

Table 2.2: Conversion factors between the CGS and MKS systems.

Regarding the expression for magnetic flux density, B, in table 2.1, one will most probably find from different books different equations relating B, the magnetic flux density, to magnetization, M. In the above, we showed that in CGS and MKS systems these equations look different. Moreover, even in the same unit system the relations are often written in different ways. For the MKS system $B = \mu_o H + M$ is just as likely to be found as $B = \mu_o(H + M)$. Although both definitions can be used, the units of M in the two expressions are different. To keep things consistent, we will use $B = \mu_o H + M$ since this allows the magnetization to have units of Tesla.

2.2 Ferromagnetic materials and the magnetization process

Ferromagnetic materials are made of one or more combinations of the following three elements, Nickel (Ni), Cobolt (Co), and Iron (Fe). In this thesis we concentrate on permalloy which is the ferromagnetic material we use in the flap actuators. Permalloy, originally a Bell Labs trade name, is the name commonly used for alloys made of nickel and iron. The most widely used permalloy composition is $Ni_{80}Fe_{20}$ [2].

All ferromagnetic materials have a magnetization associated with them. This magnetization can be traced to the spontaneous parallel alignment of electron spins and orbits in the material [3]. For simplicity, let's look at a single electron with a circular orbit around a nucleus as shown in Figure 2-1. This orbiting electron produces a magnetic moment, as described in [4], which is normal to the plane defined by the orbiting electron. Since in a given material there are many electrons, each will produce a magnetic moment and the vector sum of all the moments in the material will generate a total magnetic moment for the material. The magnetization of this material is then the net magnetic moment normalized to the volume V of the magnetic material, i.e., $\mathbf{M} = \mu_0 \frac{\mathbf{m}}{V}$, where μ_o is the permeability of air. In general, the net magnetic moment should also include moments produced by electron spins and moments produced by the spin of the nucleus. If all the magnetic moments produced are aligned in the same

direction, the net magnetization of the material is called the saturation magnetization, $\mathbf{M_s}$. In most materials the orbiting and spin moments tend to cancel out each other so they show only weak magnetic effects (small net magnetic moment). However, in ferromagnetic materials the orbiting and spin moments align with each other, and the material shows a net magnetic moment and magnetization.

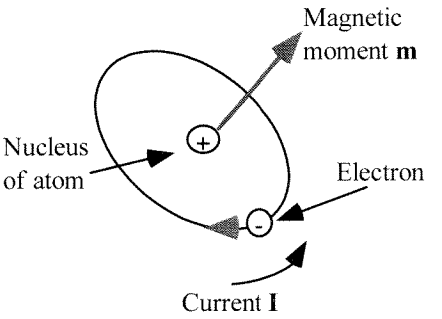

Figure 2-1: Schematic showing magnetic moment produced by electron orbiting about atom nucleus.

This implies that a ferromagnetic material should have a net magnetization associated with it at all times. In reality it is possible for the net magnetization of ferromagnetic materials to be zero. This can be explained using a more complete model for ferromagnetic materials developed by Weiss [5,6]. He stated that rather than being uniformly magnetized throughout, ferromagnetic materials are broken into small regions, called domains, which are each uniformly magnetized to the saturation magnetization of the material M_s. The magnetization vectors of each domain, however, can be randomly oriented so that the net magnetization of the whole sample is zero.

Energy balance is usually employed to explain domains and the magnetization of ferromagnetic materials in response to externally applied fields. In the following we will treat the magnetization process somewhat qualitatively and a more complete discussion is provided in [2]. A ferromagnetic material has a net energy associated with it and will

rearrange itself in order to minimize this energy. A dominant energy in a ferromagnetic material is the magnetostatic energy which is associated with the leakage of magnetic flux into the surrounding air [7]. This energy can be minimized if the flux leakage is minimized. This is achieved when the material breaks up into domains, as shown in Figure 2-2 and 2-3. In Figure 2-3d the domains have arranged in a way that a closed magnetic flux path is formed in the material and leakage becomes smaller. Energy balance also determines how many domains are formed. The material will divide into domains only until the energy required to form a new domain wall is greater than the accompanying reduction in magnetostatic energy [7]. A domain wall is the interface, or transition region, between two adjacent domains.

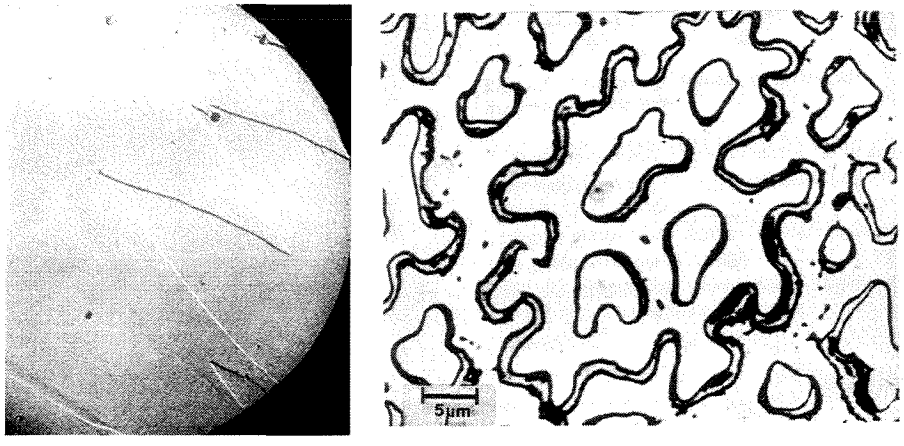

(a) (b)

Figure 2-2: Domains in ferromagnetic materials. (a) Domains formed in a permalloy sample [8]. (b) Basal plane domain structure of a hexagonal SmCo5 crystal. The regions delineated by the domain walls are alternately magnetized into and out of the plane of the photograph [7].

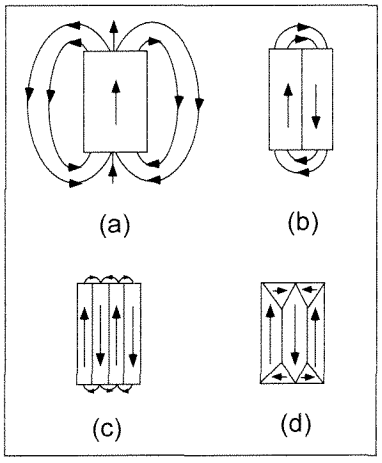

Figure 2-3: Reduction of magnetostatic energy due to flux leakage by formation of domains. (a) Single domain, showing significant flux leakage. (b) Breaking up into two domains reduces flux leakage. (c) Further reduction of flux leakage. (d) Finally by introducing closure domains flux leakage almost completely eliminated.

With the concept of domains in hand, we can better understand the mechanisms of magnetization. We will concentrate here, on the magnetization process for permalloy. To magnetize the permalloy an external magnetic field is applied. This field supplies an energy known as the *applied field energy* to the permalloy, and causes the domains whose magnetization vectors are aligned closest to the applied field direction to grow at the expense of domains that are less favorably oriented. This produces a net magnetization in the permalloy. Figure 2-4 shows a schematic of the magnetization process for permalloy. The net magnetization, which we will simply call magnetization, of the permalloy in Figure 2-4 is plotted in the M-H curve of Figure 2-5. The major magnetization steps for the permalloy of Figure 2-4 are described in the following. We start with a permalloy sample that has been demagnetized, so the permalloy has no net magnetization when no field is applied. Once a small field is applied the domain aligned closest with the field direction begins to grow, as shown in Figure 2-4b, producing a net magnetization of the permalloy. For fields smaller than H_1, defined in Figure 2-5, the domain growth is reversible so that if the field is reduced the magnetization will go back to its previous value along the curve A-B-C shown in Figure 2-5. As the applied field is further increased the aligned domain will continue to grow, but for fields between H_1 and

H_2 in Figure 2-5, the domains will grow in an irreversible manner so that if the applied field strength is reduced, the magnetization will no longer go back to its previous value. This is because the domain walls get "caught" on various structural and crystallographic obstacles in the permalloy. When a field greater than H_2 is applied, the magnetization of the permalloy will rotate to align with the applied field, as shown in Figure 2-4d. The magnetization will rotate reversibly until the field is increased above H_s. In the region above H_s, which is called approach to saturation, the magnetization is non-reversible. When the field is increased further above H_s, the magnetization will eventually saturate and no further increase in the magnetization will be achieved. When saturated, the permalloy is uniformly magnetized and there is only one domain. If the applied magnetic field is reduced after saturating the permalloy, the magnetization will follows the new curve CDE. The curve tracing the magnetization as a function of the applied magnetic field is called an M-H loop, Figure 2-6a, and can be generated for all ferromagnetic materials.

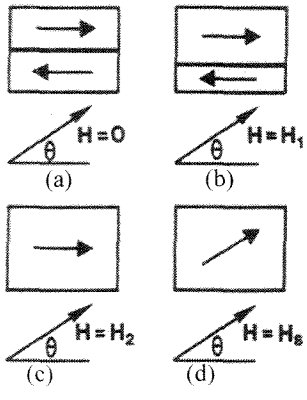

Figure 2-4: Changes in domains with increased applied field [7].

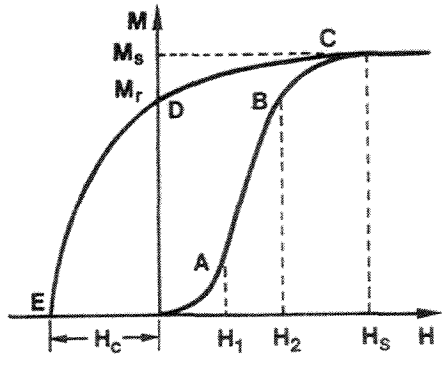

Figure 2-5: Initial magnetization curve for permalloy with the simple domain structure of Figure 1-2. Note the hysteresis is shown by the curve CDE [7].

The M-H loop is a useful tool to characterize ferromagnetic materials. Some of the important parameters that can be identified from the M-H plot are H_c and M_r. The field H_c is known as the intrinsic coercive force or simply intrinsic coercivity and is defined as

the field required to bring the magnetization of a ferromagnetic material to zero. The intrinsic coercivity is highly dependent on the particular magnetic material and provides a valuable tool to categorize and analyze ferromagnetic materials. The remnant magnetization M_r, see Figure 2-5, is the magnetization remaining in a material after it has been saturated and then the applied field has been reduced to zero.

While the M-H loop is a useful way to characterize magnetic materials, in practice it is easier to measure the B-H loop of a ferromagnetic material. B-H loops include the contribution of the externally applied field to the flux density B in the material. The most evident difference between the M-H and B-H loops is that B does not saturate, but continues to increase due to the increasing contribution from H, as shown in Figure 2-6b. At this point we should introduce another coercivity, this time for the B-H loop. In this case the coercivity is defined as the applied field required to bring the magnetic flux density to zero. For permalloy, there is a negligibly small difference between the intrinsic coercivity and the coercivity so we will not distinguish between them for the remainder of this thesis.

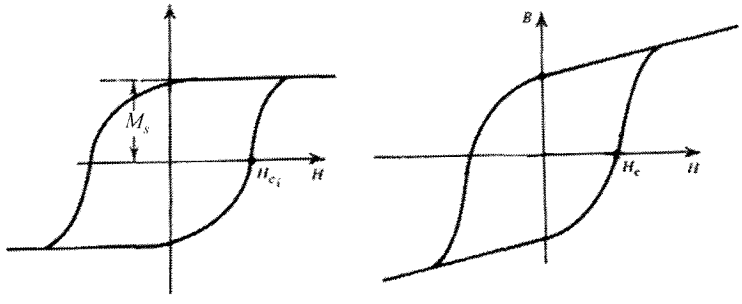

(a) (b)

Figure 2-6: (a) M-H loop, the magnetization saturates at high field values. (b) B-H loop showing that the magnetic flux density does not saturate at high magnetic fields.

As mentioned previously, during the magnetization process the applied field moves the domain walls through the material against various micro-structural and

crystallographic obstacles. The magnitude of the field required to do this determines whether the ferromagnetic material is classified as magnetically hard or soft [2,7]. Soft ferromagnetic materials, Figure 2-7, are defined as those in which large changes in magnetic flux density, or magnetization, can be produced by very small fields. The typical coercivity of soft magnetic materials is small and they usually have very small remnant magnetizations. Permalloy is a soft magnetic material, with a small coercivity of around 0.05 Oe, and it is saturated at relatively low fields. Hard magnetic materials on the other hand are characterized by high coercivity and high remnant magnetization The most convenient parameter to describe the ease with which a soft ferromagnetic material can be magnetized by an external field H is the magnetic permeability μ, which is defined as the ratio of the flux density in the material to the external field

$$\mu = B/H \qquad (2.1)$$

In soft ferromagnetic materials the B-H loop is often linear in the region about H = 0, and the permeability in this region can be approximated as the slope of the B-H loop. In general, however, this approximation is not valid, since the permeability actually varies with values of B and H.

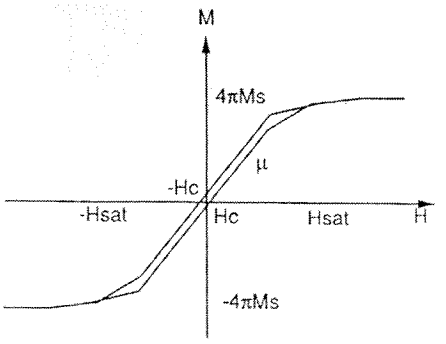

Figure 2-7: M-H loop characteristic of a soft magnetic material.

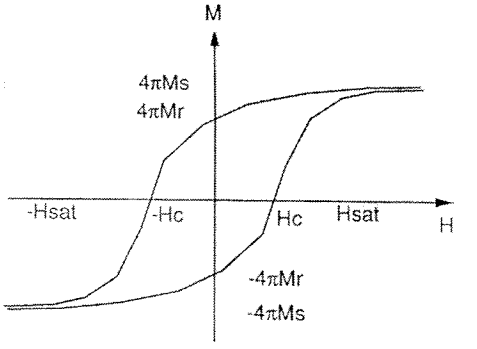

Figure 2-8: Typical M-H loop of a hard magnetic material.

Now let's switch gears and talk about a phenomenon which has important consequences on magnetic measurements, namely the demagnetizing effect. Magnetic poles are produced by the divergence of magnetization [9] and act as sources for

magnetic fields. When a ferromagnetic material is magnetized by an external magnetic field, H_e, magnetic poles are produced. These poles generate a magnetic field in the material which acts in the opposite direction to the magnetization, as shown in Figure 2-9. This magnetic field is called the demagnetizing field H_d, and is proportional to the magnetization which creates it, i.e.,

$$H_d = \frac{N_d M}{\mu_0} \tag{2.2}$$

where N_d is the demagnetizing factor and M is the magnetization. N_d depends on the shape of the body, and can be calculated exactly only for an ellipsoid. For a 3-D object the magnetization can be broken into components which lie along the x, y, and z axis. The demagnetizing fields produced along these axis are related to the magnetization by demagnetizing factors along these axis, as indicated in the above equation. The thing is that the sum of the demagnetizing factors along all three axis of a ferromagnetic material is always equal to one, i.e., $N_x + N_y + N_z = 1$ in MKS units. It is experimentally determined that the shorter the length of the ferromagnetic material along a particular axis, the higher the demagnetizing factor along this axis. The importance of the demagnetizing factor and field is in how it affects the measurements used to characterize ferromagnetic materials. In general, the magnetic flux inside a ferromagnetic material is given by $B = \mu_0 H + M$, where H is the total field inside the material. Earlier we said that the B-H loops and M-H loops were plots of magnetization or flux density as a function of applied magnetic field. We assumed that the applied external magnetic field, H_e, was the same field as inside the magnetic material, but if there is a demagnetizing field in the material, this is not true. In that case the magnetic flux density is $B = \mu_0 (H_e - H_d) + M$, where H_e is the applied external field and H_d is the demagnetizing field. So plotting B vs. H_e is not the true B-H loop, rather we should plot B vs. $H_{total} = H_e - H_d$. Only then will we obtain a true measure of the coercivity, permeability, and saturation magnetization of the material. The permalloy films used in the actuators have a maximum thickness of about 20 μm along the z axis. This is so much smaller than the length and width in the x and y directions, which are about 3 mm, so that in the plane we can approximate $N_x \approx N_y$

≈ 0. In this case, the external magnetic field is approximately the field inside the permalloy in the x-y plane. Note that the demagnetizing factor and field are important concepts and further discussion can be found in [10].

In ferromagnetic thin-films the net magnetic moment tends to align along certain directions, or axis, in the material. This preferential alignment of the net moment along a particular axis depends on how we produce and deposit the film, and also on the geometrical shape of the film. For permalloy this is called uniaxial anisotropy [11] where the magnetization tends to prefer to align about one single axis of the material. This axis is called the easy axis. The hard axis is the axis normal to the easy one, and it requires higher fields to magnetize the ferromagnetic material along it [2].

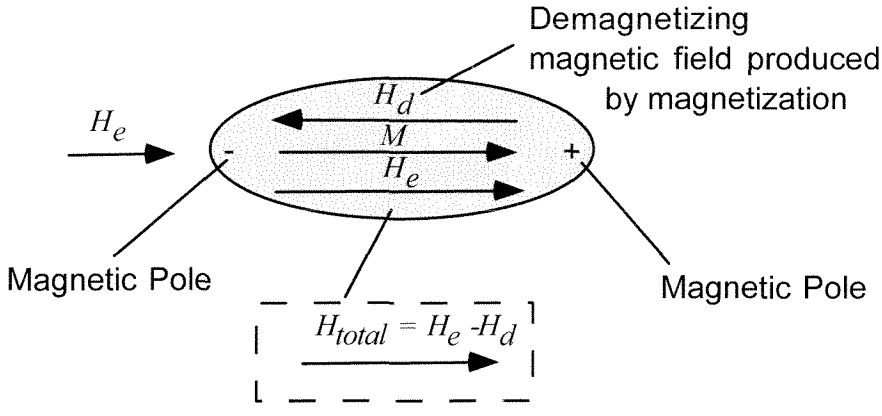

Figure 2-9: Magnetic fields inside an elliptically shaped ferromagnetic material.

2.3 Methods for measuring magnetic properties

The Hysteresis Loop Tracer is designed to provide a B-H loop trace of a given magnetic sample. Magnetic fields are produced in the loop tracer by two sets of Helmholtz coils, as seen in Figure 2-10, which provide uniform time varying magnetic fields. A pair of pickup coils, also called search coils, shown schematically in Figure 2-11, detect the induced flux of the sample and a computer control unit stores the hysteresis loop data.

Caution must be exercised when using this measurement method particularly for small samples. First, if the sample is shorter than the pickup coil length, the magnetic flux reading will not be the total flux generated in the sample. Second, the geometry of the sample has a great influence on the shape of the B-H loop. This is more significant the smaller the sample and is due to the demagnetizing effect.

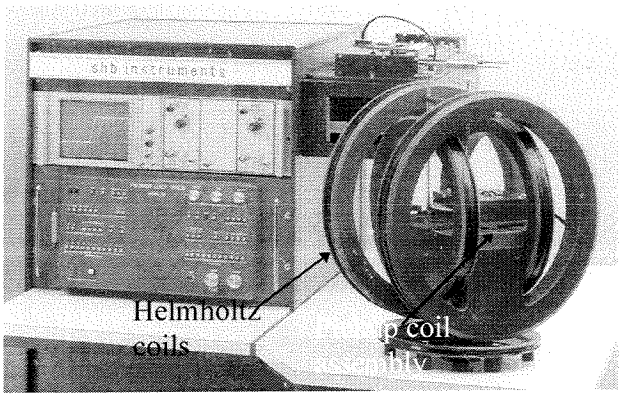

Figure 2-10: SHB 108 Hysteresis Loop Tracer system.

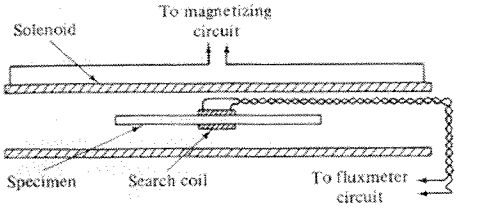

Figure 2-11: Schematic showing concept of B-H loop measurement system.

VSM stands for vibrational sample magnetometer. It is used to measure the magnetic moment of a sample. It is a simple, relatively inexpensive, yet precise measurement method. The VSM is most often used to characterize hard magnetic materials. However, it also provides an accurate way to determine the saturation magnetization of soft ferromagnetic samples. A conceptual schematic showing the VSM setup is given in Figure 2-12. The sample is vibrated perpendicularly to a constant, uniform magnetizing field, and this produces an oscillating magnetic field which induces a voltage in the

stationary detection coils which are shown in Figure 2-12 as 7. From measurements of this voltage, the magnetic properties of the sample are deduced. A second voltage is induced in a similar stationary set of reference coils by a reference sample, which is a small permanent magnet or an electromagnet. The reference sample is attached to the same support as the measurement sample. It allows noise effects to be subtracted out of the measurement.

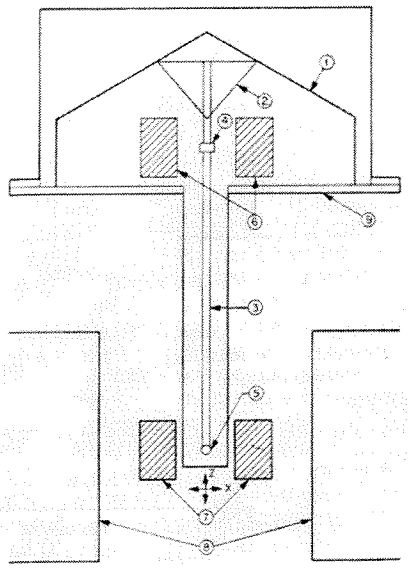

Figure 2-12: (a) Simplified schematic of VSM. (1) loud-speaker transducer (2) conical support (3) drinking straw (4) reference sample (5) sample (6) reference coils (7) sample coils (8) magnet poles (9) metal container.

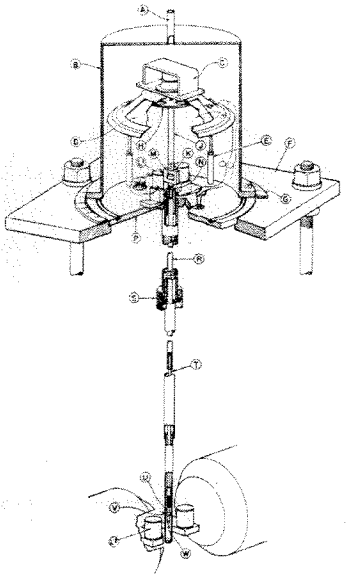

Figure 2-13: Detailed mechanical construction of vibrating sample magnetometer [12].

The Squid Magnetometer uses a Superconducting Quantum Interference Device (liquid helium cooled amplifier) which provides the magnetometer a magnetic flux sensitivity and dynamic range unavailable in other magnetometers. The sample is moved through a magnetic field generating a signal which is picked up and amplified by the squid device. The squid provides a measure of the magnetic moment as a function of the applied magnetic field and works for both soft and hard ferromagnetic materials.

2.4 Magnetostatics

In this section, we analyze the magnetic forces and torques which act on a bar magnet and a current loop in a magnetic field. Later in this thesis we borrow from this analysis to model the forces and torques which act on the permalloy layers, and copper coils, which are deposited on the flap actuators.

A magnetized bar magnet of magnetization M and magnetic moment **m** can be modeled as a magnetic dipole with poles $+Q$ and $-Q$ which are separated from each other by the length L of the magnet [9, 13]. The pole strengths Q are given by

$$Q = \frac{MA}{\mu_o} \tag{2.3}$$

where A is the cross sectional area of the magnet, and μ_0 is the permeability of free space [9]. Further discussion of magnetic poles, which are produced due to the divergence of the magnetization at the ends of the magnet, can be found in [9]. When a magnetic pole of strength Q (Amperes-meter ≡ Am) is brought into a magnetic flux density B (webers/meter^2), the force F (Newton) acting on the magnetic pole is [2]

$$F=QB \tag{2.4}$$

Therefore, if we examine the bar magnet in a uniform magnetic flux density B, as shown in Figure 2-14, two equal but opposite forces will be acting on the poles. The net translational force will be zero, but the result of the force couple will be a torque given by

$$T = -F\,L\sin\theta = -QBL\sin\theta \qquad (2.5)$$

Here, Q is the magnetic pole strength, B is the magnetic flux density, L the length of the magnet which is also the distance between the poles, and θ is the angle between the magnetic moment of the magnet and the direction of the magnetic flux density.

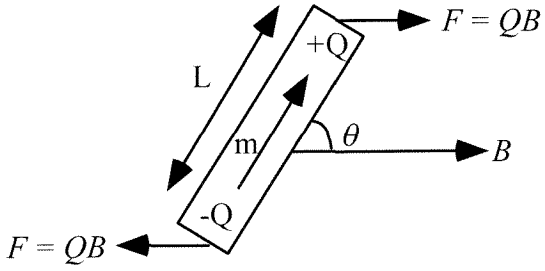

Figure 2-14: A bar magnet under the action of a force couple in a uniform magnetic field.

The torque produced will act to rotate the bar magnet so that the magnetic moment aligns with the direction of the magnetic flux density. Substituting equation (2.3) into equation (2.5), we get the following expression for the magnetic torque,

$$T = -MVH\sin\theta \qquad (2.6)$$

Here V is the volume of the bar magnet, and H is the applied magnetic field strength. However, we can also relate the torque to the magnetic moment of the bar magnet, since the magnetization is related to the magnetic moment of the ferromagnetic material by [14],

$$M = \mu_0 \frac{m}{V} \qquad (2.7)$$

where V is volume of the bar magnet, m is its magnetic moment, and μ_o is the permeability of free space. Substituting equation (2.7) into equation (2.6) gives

$$T = -mB\sin\theta \tag{2.8}$$

which in vector notation can be written as

$$\mathbf{T} = \mathbf{m} \times \mathbf{B} \tag{2.9}$$

So in general, the torque acting on a magnetic moment **m**, produced by any ferromagnetic material, in a uniform magnetic flux density, **B,** is given as the cross product of these two vectors.

In the uniform field the forces acting on the poles cancel so there is no net translational force. In order to translate the magnet, it is therefore necessary to have a gradient in the flux density, in other words, a non-uniform field. If we assume the magnetic flux density has a gradient in the x-direction of $\frac{\partial B_x}{\partial x}$, then the net translational force along the x-direction can be written as

$$F_x = QB_1 - QB_2 \tag{2.10}$$

Here B_1 is the value of the magnetic flux density at location 1 and B_2 is the value of the magnetic flux density at location 2, as shown in Figure 2-15. Equation (2.10) can be rewritten as

$$F_x = QL\frac{\partial B_x}{\partial x} \tag{2.11}$$

where L is the length of the magnet. Substituting equations (2.3) and (2.7) into equation (2.11) yields a relation for the force in the x-direction, as a function of the magnetic moment of the magnet.

$$F_x = m\frac{\partial B_x}{\partial x} \tag{2.12}$$

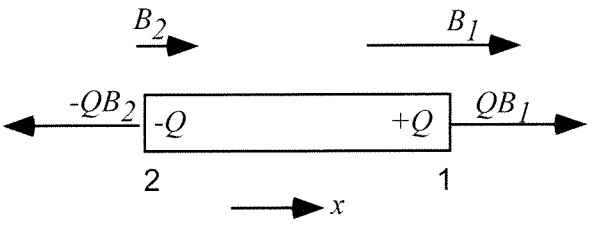

Figure 2-15: A magnet under the action of translational force in a gradient magnetic field.

As we discussed in section 2.2 the source of the magnetization and the net magnetic moment in ferromagnetic materials is the sum of many magnetic moments produced by individual electrons orbiting and spinning about the nucleus of an atom. An electron spinning in an orbit around the nucleus of an atom is equivalent to a tiny current loop, so we expect a current loop in a magnetic field also to have a magnetic moment. How this magnetic moment comes about, and what forces act on this current loop when it is placed in a magnetic field, will be discussed in the following.

We start by examining a wire placed in a uniform magnetic flux density. As soon as current flows through the wire, a force will act on the wire. An expression for the force on an element of the wire is given by [16],

$$\mathrm{dF} = IB\,dL\sin\theta \qquad (2.13)$$

where I (Amperes) is the current in the wire, dL (meters) is the length of the conductor element, and B (Tesla) is the magnetic flux density. In vector notation this equation, called the motor equation, can be written as [15]

$$\mathbf{dF} = (\mathbf{I} \times \mathbf{B})\,dL \qquad (2.14)$$

When the wire with current flowing is formed into a loop and is placed parallel to a uniform magnetic field, forces are produced which generate a torque to rotate the loop. For a square current loop of side length L in a uniform magnetic field **H** (magnetic flux density **B)** with a current I, the force on any element dL of the loop is given by equation (2.132). If the (unit) normal $\hat{\mathbf{n}}$ to the plane of the loop is at an angle θ with respect to **B**, as shown in Figure 2-16, the turning force F_t (perpendicular to the plane of the loop) is

$$F_t = 2ILB \sin\theta \qquad (2.15)$$

and the torque

$$T = F_t \frac{L}{2} = IL^2 B \sin\theta \qquad (2.16)$$

However, L^2 is the area of the loop, so $L^2 = A$, and the torque expression can be rewritten as

$$T = IAB \sin\theta \qquad (2.17)$$

The product IA has the units of A-m^2, the same as for a magnetic moment in a ferromagnetic material, so if we identify $m = IA$, then equation (2.17) and has the same form as equation (2.8). We therefore define $m = IA$ as the effective magnetic moment of the current loop, and the torque expression becomes

$$T = mB \sin\theta \qquad (2.18)$$

where θ is the angle between the normal to the plane of the loop and the direction of B. If the loop has N turns, the magnetic moment becomes $m = NIA$. This can be written in vector notation, where the magnetic moment is the vector $\mathbf{m} = \hat{\mathbf{n}}\, m$, and where the unit vector $\hat{\mathbf{n}}$ is perpendicular to the plane of the loop, in the direction given by the right-hand rule. The vector notation for a torque acting on any shape of current loop is

$$\mathbf{T} = \hat{\mathbf{n}}\, m \times \mathbf{B} = \mathbf{m} \times \mathbf{B} \qquad (2.19)$$

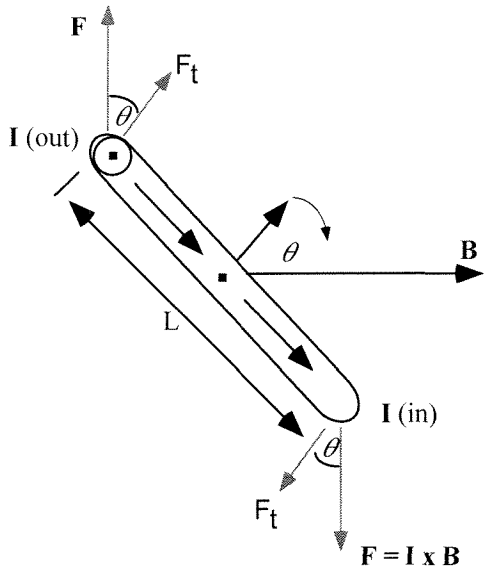

Figure 2-16: Side view of current loop in magnetic field B experiencing a torque, **T**, tending to align its normal, **n**, with **B.**

The forces acting on the current loop in a uniform magnetic flux density cancel so there is no net translation force acting on the loop. A translation force is produced when the current loop is placed in a non-uniform magnetic field. The force on a coil in a non-uniform magnetic field in the x-direction, as shown in Figure 2-17, has the same form as the expression for the force on a bar magnet and is given as

$$F_x = m\frac{\partial B_x}{\partial x} \tag{2.20}$$

However, here $m = IA$ is the effective moment produced by the current loop [16].

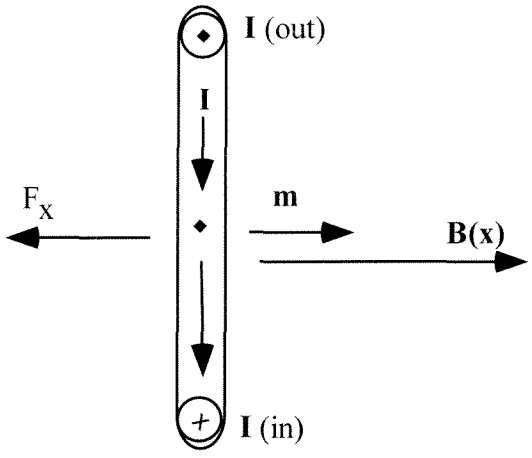

Figure 2-17: Current loop in a non-uniform magnetic flux density experiencing a translational force F_x.

2.5 Summary of definitions

B-H and M-H loops are used to describe and characterize magnetic materials. The B-H loop is a plot of the amount of magnetic flux density generated by a magnetic material when subjected to particular applied magnetic fields. The M-H loop, on the other hand, is a plot of the magnetization of the material as a function of the applied magnetic field.

Saturation magnetization (M_s) is the maximum magnetization (magnetic moment, normalized to volume) obtainable in a given magnetic material.

Remnant magnetization (M_r) is the magnetization (magnetic moment normalized to volume) remaining in a material after a saturating magnetic field has been applied and removed.

Coercivity (H_c) is the field needed to reverse the magnetization of a sample. It can also refer to the field necessary to reduce the magnetization of a sample to zero.

Permeability (μ) Is a parameter which describes the "ease" with which a soft ferromagnetic material can be magnetized by an external field H. It is defined as the ratio of the flux density in the material, B, to the external field, H, that produces it. i.e., $\mu = B/H$.

Magnetocrystalline anistoropy is a preferential alignment of the magnetization corresponding to a particular crystal orientation of the material.

Shape anisotropy is the preferential alignment of the magnetization along a longer axis of a material based simply on its geometry. As an example, a polycrystalline specimen that is spherical in shape, will magnetize to the same extent in any direction at a given applied field. But if it is non spherical, it will be easier to magnetize it along a long axis than a short axis.

Soft and hard materials Magnetic materials are typically classified as either magnetically hard or magnetically soft. Soft magnetic materials are defined as those in which very large changes in the magnetic flux density (or magnetization) can be produced by very small fields or as $\frac{\mu_o H_C}{M_S} << 1$. Hard magnetic materials are characterized by high coercivities and high remnant magnetizations or as $\frac{\mu_o H_C}{M_S} >> 1$ hard.

Magnetic domains In the demagnetized state ferromagnetic materials are divided into small regions called domains. Each domain is spontaneously magnetized to the saturation value Ms, but the direction of magnetization of the various domains are such that the specimen as a whole has no net magnetization.

References

[1] R. Goldfarb, "Panel Discussion on Units in Magnetism," *Joint MMM-Intermag conference*, Albuquerque, NM, 1994.

[2] B. D. Cullity, *Introduction to Magnetic Materials*, Addison-Wesley Publishing company, Reading Massachusetts,1972.

[3] J. Smit and H.P.J. Wijn, *Ferrites*, N.V. Philips Gloeilampenfabrieken, Eidhoven Holland, 1959, pp. 6-14.

[4] B. D. Cullity, *Introduction to Magnetic Materials*, Addison-Wesley Publishing Company, Reading Massachusetts, 1972, pp. 85-88.

[5] P. Weiss, "L-Hypothese du Champ Moleculaire et la Propriete ferromagnetique," *Journal de Physique*, 4th Series, Vol. 38, 1931, pp. 66-690.

[6] S. Chikazumi, *Physics of Magnetism*, John Wiley & Sons, Inc., New York, 1964, pp. 113-127.

[7] R. A. McCurrie, *Ferromagnetic Materials: structure and properties*, Academic Press, San Diego, 1994.

[8] M. Prutton, *Thin Ferromagnetic Films*, Buttersworths, Washington D.C. 1964

[9] J. D. Kraus, *Electromagnetics*, McGraw-Hill, New York, 1973, pp. 319-323.

[10] B. D. Cullity, *Introduction to Magnetic Materials*, Addison-Wesley Publishing Company, Reading Massachusetts, 1972, pp. 49 - 65.

[11] B. D. Cullity, *Introduction to Magnetic Materials*, Addison-Wesley Publishing Company, Reading Massachusetts, pp. 233-245.

[12] S. Foner, " Versatile and Sensitive Vibrating-Sample Magnetometer," *The review of Scientific Instruments*, Vol. 30 (7), pp. 548 - 557.

[13] S. Chikazumi, *Physics of Magnetism*, John Wiley & Sons, Inc, New York, 1964, pp. 3-7.

[14] B. D. Cullity, *Introduction to Magnetic Materials*, Addison-Wesley Publishing Company, Reading Massachusetts, 1972, p. 5.

[15] J. D. Jackson, *Classical Electrodynamics*, John Wiley & Sons Inc., New York, 1962.

[16] J. D. Kraus, *Electromagnetics*, McGraw-Hill, New York, 1973, pp 219 -229.

Chapter 3

Technology Requirements for Electromagnetic Flap Actuators

In this chapter we discuss the technology we have established at Caltech to enable the fabrication of the electromagnetic flap actuators. This technology involves electroplating, insulator deposition and patterning, and silicon etching. We describe how to prepare electroplated copper and permalloy (NiFe) films that meet the MEMS actuator requirements. We also discuss how to form and etch seedlayers, which are conductive metal layers onto which the above metals are electroplated, and describe the various types of insulators used and methods for preparing them. Finally, we consider some ways to etch single crystal silicon, since the mechanical structure of these actuators is formed from it.

3.1 Electroplating

The process of electroplating, also called electrodeposition, is one in which current is carried from an anode to a cathode across an electrolyte, depositing a substance at the cathode [1]. Electroplating is widely used in many applications and devices since it is inexpensive, relatively fast and allows the formation of thick structures (more than 10 μm thick). Electroplating is used in such applications as metal finishing, and in disk-drive inductive thin film head fabrication.

3.1.1 Fundamentals

According to Farady's law, the weight of metal deposited at the cathode, or dissolved from the anode, is proportional to the quantity of current supplied, and also to the chemical equivalent weight of the metal. The equivalent weight of a metal is its atomic weight w, divided by the valence, z, of the ion from which discharge is taking place. The quantity of current that deposits one equivalent weight of the metal is called the Faraday, F, which equals 96,500 coulombs. The quantity of metal deposited W_t (in grams) is

$$W_t = \frac{It}{96{,}500} \times \frac{w}{z} \tag{3.1}$$

where I is the current applied to the bath and t is the deposition time in seconds [2]. Note, W_t is also equal to the weight of the metal removed from the anode.

In practice, there are deviations from Farady's law mostly due to unproductive simultaneous electrode reactions (i.e., hydrogen gas formation), and generation of heat due to power dissipated in the bath. To quantify these deviations two terms known as cathode efficiency and anode efficiency are defined. The cathode efficiency, I_{effc}, is defined as

$$I_{effc} = \frac{W_d}{W_t} \times 100 \tag{3.2}$$

where W_d is the weight of metal actually deposited, and W_t is the weight of metal calculated from the quantity of current passed. The efficiency with which the anode dissolves is called the anode efficiency, I_{effa}, and is given by a similar expression

$$I_{effa} = \frac{W_r}{W_t} \times 100 \tag{3.3}$$

Here W_r is the weight of metal actually removed from the anode, and W_t is the weight of metal calculated from the quantity of current passed. Note the cathode and anode efficiencies are given as a percentage. By adjusting the plating bath conditions, the

cathode and anode efficiencies can be maximized. Higher cathode and anode efficiencies lead to better quality deposits, and reduce the power consumption of the bath.

While the amount of metal deposited and the efficiency with which it is electroplated are important parameters to control, it is also necessary to ensure that the metal is uniformly distributed on the work piece. The metal distribution on the cathode is determined by the distribution of electric field lines at the cathode. These field lines tend to concentrate near the edges of the cathode and result in locally higher plating rates (typically 10% - 20% of current is concentrated on the edges). To ensure that the work piece is uniformly plated, a thief is used. A thief is a conducting region that is placed around the perimeter of the work piece. The thief attracts the higher density of field lines and ensures that the whole work piece has a more uniform field and current distribution.

Although we have discussed how the current supplied to the plating bath determines the amount of metal electroplated, the actual plating mechanism is really governed by potential differences. When a metal is placed in a solution of its own ions, it develops a potential. In the case of copper, two reactions take place to produce this potential, equations (3.4) and (3.5).

$$Cu \rightarrow Cu^{2+} + 2e \qquad (3.4)$$

$$Cu^{2+} + 2e \rightarrow Cu \qquad (3.5)$$

Initially one reaction may occur faster than the other, but this in turn increases the rate of the second reaction until an equilibrium is established. In equilibrium atoms go into the solution as ions at the same rate as ions are deposited as atoms. In this equilibrium state a charge separation occurs which is called a double layer. This double layer (Figure 3-1a) occurs when a small but measurable number of excess positive cations confront an equal number of negatively charged anions at the electrode-solution interface [2]. If the ionization is initially faster, the metal becomes negatively charged relative to the solution; if the deposition is initially faster, the metal becomes positively charged relative to the

solution. The resulting potential of the metal is called the equilibrium potential (Figure 3-1b). Some metals (e.g., Cu, Ag, Au) possess relatively little tendency to pass into solution as ions, and therefore they have positive potentials, while other metals (e.g., Na, Zn, Fe) form ions readily and they have negative potentials. An expression for the equilibrium potential is given by the Nernst equation, equation (3.6),

$$E = E_o - \frac{RT}{ZF} log\, Q \qquad (3.6)$$

where E is the equilibrium potential, E_o is a constant for the metal and is called the "standard potential," R is the gas constant, T is the absolute temperature, Z is the charge on the ion, F is the faraday, and Q is the reaction quotient [3].

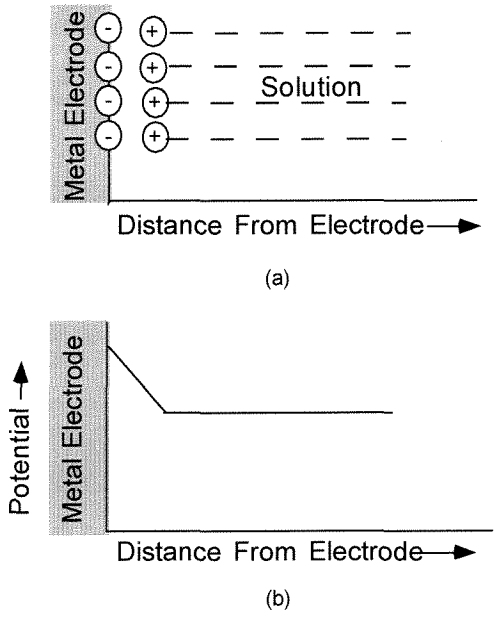

Figure 3-1: (a) Schematic showing double layer near metal electrode. (b) Schematic showing potential as a function of distance from electrode. The potential of the metal electrode is its equilibrium potential.

If we take two copper electrodes and apply a sufficiently large voltage across them, copper will deposit at the negative electrode while copper will be removed from the

positive electrode. The voltage necessary for the electroplating process to occur is the sum of the overvoltage at the cathode and the overvoltage at the anode. Overvoltage is defined as the potential difference between the equilibrium potential of the metal electrode, and the potential at which metal is deposited at or dissolved from metal electrode. The overvoltage observed at an electrode is really a combination of three overvoltages, a concentration overvoltage, an ohmic overvoltage, and an activation overvoltage [1].

The concentration overvoltage is due to the fact that near the electrodes the concentration of ions is locally different from the bulk solution. This concentration, according to the Nernst equation, changes the potential of the electrode. At the cathode, concentration overvoltage is produced by the depletion of depositing ions in the immediate vicinity of the cathode so that the ion concentration in the immediate vicinity of the cathode is less than in the bulk. According to the Nernest equation, this will cause the cathode potential to be more negative. Concentration overvoltage at the anode is produced by essentially similar concentration changes but in the opposite direction.

Ohmic overvoltage occurs when an electrode is covered with a poorly conducting film such as a layer of oxide or grease. The resistance of this layer is higher than the bath, and requires a significant increase in the applied voltage to keep the plating process operating.

Activation overvoltage [2] is determined by the slowest step in the electroplating process. This process begins with the hydrated ion in the bulk of the solution and ends with the metal atom forming part of the deposit on the cathode. Each step has a different rate of reaction. The slowest step dictates the overall rate. The slowness of the step is equivalent to a "resistance" offered to the progress of the plating process. This is reflected in the observed overvoltage. For most metals, called reversible electrodes, activation overvoltage is quite small and can usually be neglected unless the current density is very large. For some metals, called irreversible metals, such as iron, cobalt, and nickel, the overvoltage is large. For example, for nickel the equilibrium potential Eo = - 0.25V; therefore, we expect to deposit nickel from a nickel salt solution with a 1 gram ion/liter concentration of Ni^{2+}, when the cathode potential reaches about -0.25V.

Instead we have to apply a potential between -0.4V and -0.5V in order to compensate for the activation overvoltage.

In conclusion, in order to achieve electroplating, the voltage we apply between the anode and cathode must be sufficient to meet both the anode and cathode overvoltages. In practice, the voltage applied between the anode and cathode is usually higher. This is due to the fact that the quantity of metal deposited is proportional to the current supplied, and the electroplating time. To reduce the plating time while still attaining the desired deposit thickness, we must increase the applied current. Since the current is proportional to the voltage applied, increasing the current means increasing the applied voltage above the cathode and anode overvoltages. The applied current, however, can not be increased indefinitely. Above a certain range the current leads to a reduction in plating efficiency and a degradation of the quality of the deposit, and this range depends on many parameters [3]. So in practice, parameters such as the amount of current applied, the amount of agitation of the bath, the temperature and *pH* of the bath as well as the constituents in the bath must be experimented with and fine tuned in order to achieve the desired electrodeposit.

3.1.2 Copper Electroplating

The copper plating recipe we use is listed in table 3.1. The bath consists of a mixture of copper sulfate, water and sulfuric acid. The copper sulfate provides the copper ions, which are plated at the cathode, while the sulfuric acid assists in the corrosion of the anode and helps to replenish the copper ions in the plating solution. The sulfuric acid increases the conductivity of the solution, and reduces the anode and cathode overvoltages, and also serves to prevent precipitation of basic salts [4].

The concentration of copper sulfate in the plating solution is not critical, as long as its concentration is greater than 60 g/l. In this range, changing the concentration only slightly affects the resistivity of the solution, and the overvoltages of the anode and cathode. A concentration of less than 60 g/l of copper sulfate results in a decreased

cathode efficiency. Changes in sulfuric acid concentration have a much greater effect on the solution conductivity and anode and cathode overvoltage. For example, specific conductivity is nearly doubled when the concentration of sulfuric acid is raised from 50 to 100 g/l. Cathode overvoltage decreases when a small amount of sulfuric acid is added to a solution of copper sulfate, but increases as the acid concentration is increased until a maximum is reached at about 50 g/l. Although the overvoltage is higher at this concentration, the deposited copper tends to have higher grain refinement which is often desirable [4].

In many plating applications additional chemicals such as brightening agents and levelers are used to further improve the surface quality of the copper. Their use, however, must be evaluated carefully for each application since they can produce undesirable characteristics as well. Thiourea is found to be effective in leveling deposits plated at low current densities. As an example a surface roughness of 0.6 μm RMS is smoothed to 0.3 μm RMS in a 25 μm thick copper plate. The grain-refining and brightening effects of thiourea are attributed to its absorption in the copper deposits which effects the crystal nucleation. The problem with using thiourea is that it makes the electrodeposit more brittle. By combining Thiourea with naphthalene disulfonic acid, the embrittling effect can be reduced. However, these additives tend to increase the intrinsic stress of the copper deposits. For applications, where thick deposits are necessary, low stress copper is much more important than reducing its roughness. Also, brightners make the bath more susceptible to contamination, and it should be replaced often. By comparison, the copper electroplating bath we use can last up to 6 months.

Figure 3-2 shows a schematic of the electroplating bath we built. The anode sits on the bottom of the tank. The cathode, a holder into which the silicon wafer is placed, lies above facing the anode. A stirring paddle moves between the anode and cathode and replenishes the solution in the double layer. Good quality copper deposits are obtained with sheet resistivities of 1.7 μΩ-cm, close to that of bulk copper (1.67 μΩ-cm). The plating is done at room temperature and the optimal plating rate for the copper is found to be 0.1 μm/min which corresponds to a current density of 10 mA/cm^2. Figure 3-3 shows a

photograph of electroplated copper conductors which are 12 μm thick. Figure 3-4 is a scanning electron microscope (SEM) picture of one of the conductors and gives a measure of the copper roughness.

Electroplating recipe:

1)	Start with 8 liters water then add		
2)	Copper Sulfate	CuSO4•5H20	250g/liter
3)	Sulfuric Acid	H2SO4	50g/liter

Table 3.1: Copper electroplating solution recipe.

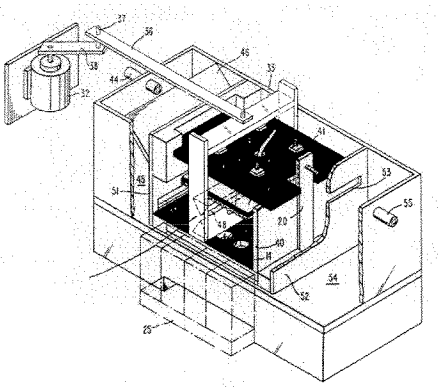

Figure 3-2: Conceptual schematic of copper electroplating tank.

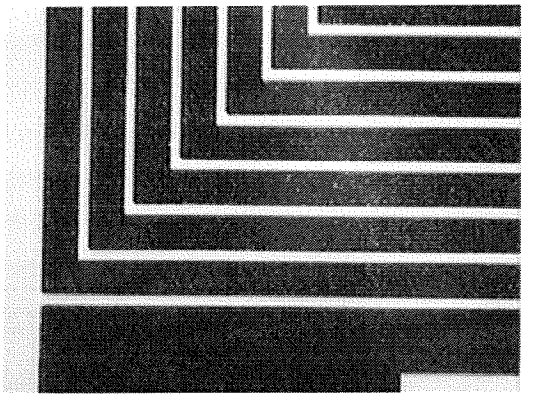

Figure 3-3: Good quality electroplated copper lines (J = 10 mA/cm^2).

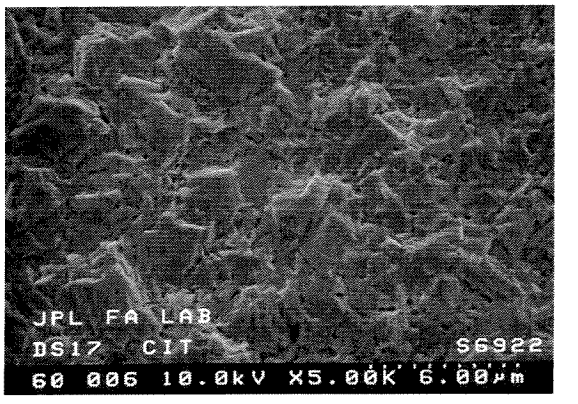

Figure 3-4: SEM of copper line. RMS roughness ~ 1 μm.

3.1.3 Permalloy Electroplating

In this work we are concerned with electroplating thick films which have good compositional uniformity and high saturation magnetizations. In general, however, the thicker the films the more difficult it becomes to control their properties. The electroplating recipe we use for the permalloy bath is shown in Table 3.2 and allows precise control of the deposition properties.

The recipe lists many chemicals; their purpose in the bath will now be discussed [5,6]. The electroplating solution contains cations of the metal to be plated, anions to provide the most advantageous deposition conditions, and additives for special purposes. In alloy plating, the composition of the plated material depends on the ratio of the reducible cations in the region near the cathode (depletion region). In the case of permalloy plating, iron is more readily reduced than nickel. So the ion ratios of Fe to Ni are kept small relative to the atom ratio desired in the plate. To improve the deposition conditions, anions are added to the bath. These include sulfamate, which allows electroplating with high current efficiencies and reduces the amount of hydrogen that is evolved at the cathode. The chloride ion enhances the anode dissolution, reducing the dissolution problem prevalent in high nickel content anodes.

There are several types of additives used in the bath. The first type of additives known as nonreducible cations increase the solution conductivity. In this bath we use sodium although potassium can also be used. Sodium increases the solution conductivity, and the salt from which it is derived is known as a "supporting electrolyte." A second type of additive is the *inorganic compound.* One example is boric acid which is a buffering agent. The buffering agent provides *pH* control and is very important in acid baths where hydrogen competes with the metal ions for reduction, and where plating mechanisms are affected by *pH.* The buffering takes place at the cathode so a much greater range of solution *pH* is tolerable. A third type of additive is the organic

compound. Its roles include wetting agent for better cathode and anode behavior (to minimize cathode pitting), leveling, brightening, and stress reduction. A common stress reducer added to the permalloy bath is sodium saccharin. The replenishing solution listed in table 3.3 is used to maintain a relatively constant concentration of iron ions in the solution, as well as ensure that the *pH* of the solution is maintained at around 2.7 ± 0.05.

Electroplating recipe:

1)	Start with 3.75 liters DI water then add as follows:		
2)	146.25g NiCl2•6H20	(39g/liter)	(9.7g/l Ni++) (green color)
3)	61.125g NiSO4•6H20	(16.39g/liter)	(4g/l Ni++)
4)	93.75g H3BO3	(25g/liter)	(buffer agent keeps ph at 2.7)
5)	5.625g Sodium Saccharin	(1.5g/l)	(stress reducer)
6)	93.75g NaCl	(25g/l)	
7)	Wait at least several hours preferably 1 day to let chemicals mix		
8)	Now adjust PH to 2.8 by adding 8 drops of H2SO4 (98%)		
	(a PH greater than 3.0 will oxidize Fe++ and make it Fe+++)		
9)	5.25g FeSO4•7H2O	(1.4g/l)	(0.28g/l Fe++)

Table 3.2: Recipe for permalloy electroplating solution.

1) $FeS0_4 \bullet 7H_2O$	5 g
2) HCl	50 ml
3) H_2O	50 ml

Table 3.3: Replenishing (make-up) solution.

A photograph of the permalloy plating tank is shown in Figure 3-5. Its design is basically the same as the copper plating tank, except that a permanent C-shaped magnet is located around the tank. The permanent magnet induces a crystalline anisotropy in the permalloy, to improve the permalloy quality. The anode lies at the bottom of the tank and

the cathode, which holds the wafer to be electroplated, is placed above it. A stir-paddle moves between the cathode and anode at about 30 rpm.

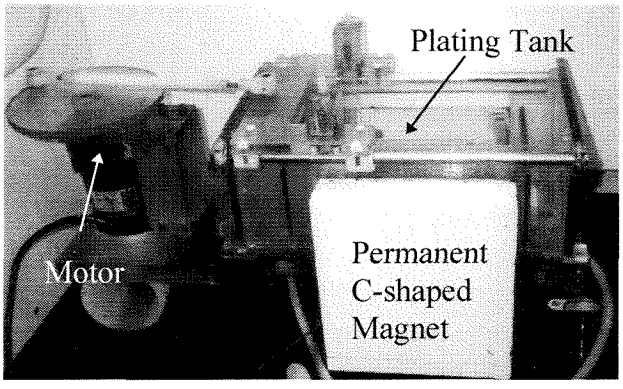

Figure 3-5: Photograph of permalloy electroplating tank.

Figure 3-6 shows an SEM picture of permalloy electroplated using this tank. The permalloy shown is electroplated on top of photoresist and closely follows the contours of the resist. The surface roughness of a 4 micron thick permalloy layer is shown in Figure 3-7. It was plated at a current density of 10 mA/ cm^2, and has an average surface roughness of about 100 nm.

We investigated the magnetic properties of the permalloy using a hysteresis loop tracer. To characterize the permalloy we made 1 cm x 1 cm x 4 μm test samples which were electroplated at different rates. In the characterization of the permalloy samples, the demagnetizing effects were neglected, because the lengths and widths of the permalloy layers are so much greater than the thickness. The samples were plated at current densities ranging from 10 mA/cm^2 to 25 mA/cm^2, and then measured in a BH-loop tracer. Figure 3-8 shows the resulting traces. The current density affected the plating rate which ranged from 0.066 μm/min at 10 mA/cm^2 to 0.26 μm/min at 25 mA/cm^2. From Figure 3-8, it is evident that at the low plating rates the flux density produced by the permalloy has a linear relationship with applied field, up to saturation. For the samples plated at the higher rates, this relationship is nonlinear. The second observation from these measurements is that the permalloy plated at 10 mA/cm^2 has a clearly definable easy and hard axis which is due to crystalline anisotropy induced by the magnetic fields present

during the electroplating process. The permalloy films deposited at the higher current densities, however, do not exhibit any anisotropy (i.e., the B-H loop looks the same in all directions). Further we observe that as the plating current density is increased, the applied magnetic field, H_{sat}, required to saturate the permalloy increases. For a current density of 10 mA/cm^2 H_{sat} is ~ 400 A/m (5 Oe), while at a current density of 25 mA/cm2 H_{sat} is ~ 4140 A/m (52 Oe). The coercivity of the permalloy plated at 10 mA/ cm2 is around 80 A/m (1 Oe). For comparison the tabulated value of standard 80-20 permalloy is around 4 A/m (0.05 Oe). Although our coercivity is higher, when one considers the magnitude of the applied fields we use (greater than 1000 A/m), the coercivity is not of great concern. The y-axis of the BH-loop is uncalibrated since our samples are smaller than the length of the pickup coil. To calibrate the y-axis a VSM measurement must be performed. Such a measurement was not performed on these samples because of our very restricted access to a VSM. However, we did do VSM measurements on the actuators presented later in this thesis .

To conclude, we found that the permalloy we have electroplated is well suited for our applications. We also observed that by changing the plating rates we could tailor the permalloy properties to our requirements.

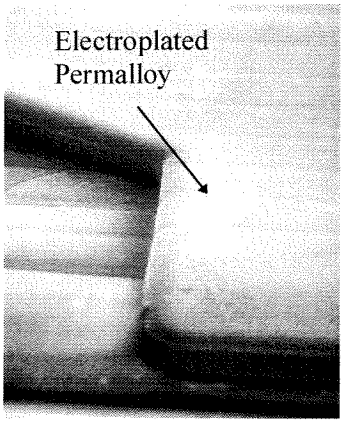

Figure 3-6: SEM showing electroplated permalloy on top of photoresist insulated copper coils.

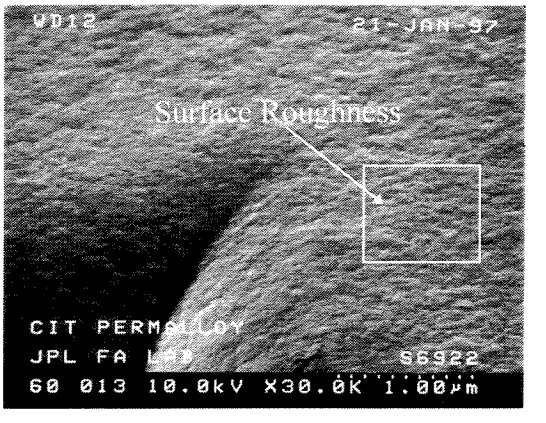

Figure 3-7: Close up view of electroplated permalloy showing surface roughness.

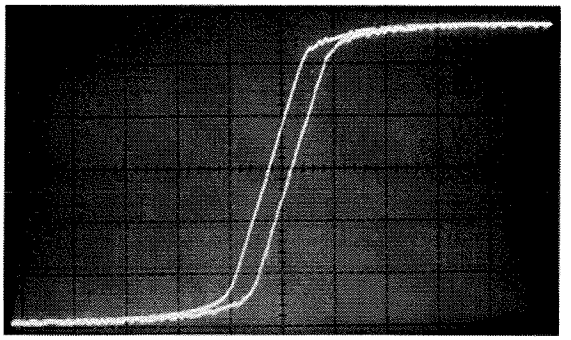

(a) Sample 1: Easy Axis:
Horizontal axis: 398 A/m / div
(5 Oe / div) Vertical axis: Uncalibrated

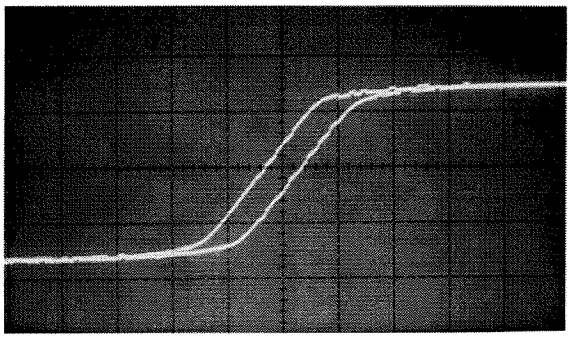

(b) Sample 1: Hard Axis:
Horizontal axis: 398 A/m / div
(5 Oe / div) Vertical axis: Uncalibrated

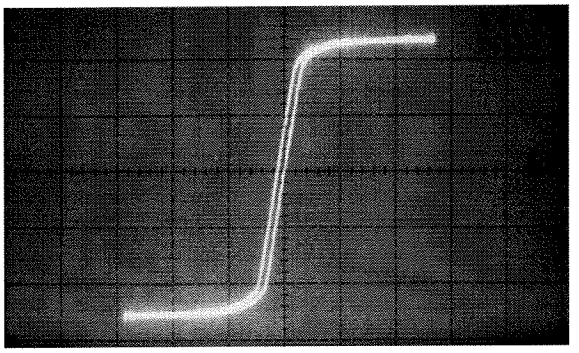

(c) Sample 2: Horizontal axis: 796 A/m /div
(10 Oe / div) Vertical axis: Uncalibrated

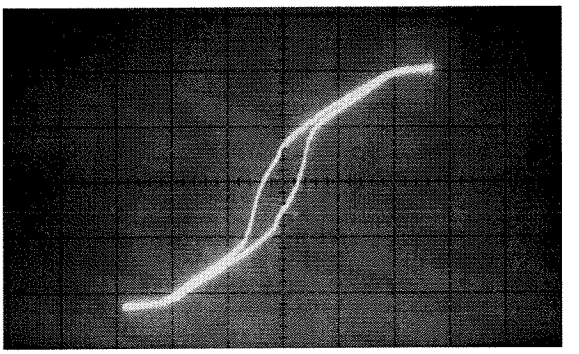

(d) Sample 3: Horizontal axis: 796 A/m /div
(10 Oe / div) Vertical axis: Uncalibrated

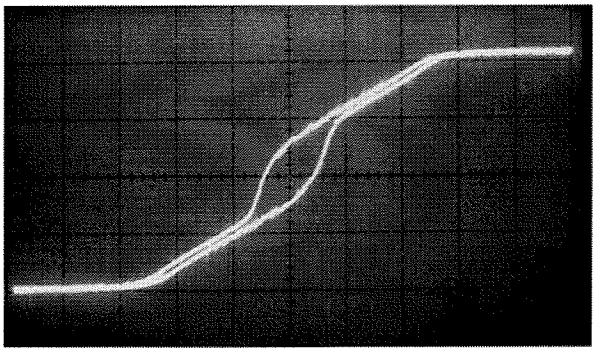

(e) Sample 4: Horizontal axis: 1.6 KA/m /div
(20 Oe / div) Vertical axis: Uncalibrated

Figure 3-8: B-H loops for samples plated using the following conditions:

Sample #	Current Density	Plating Rate	Deposit Thickness
1	10 mA/cm^2	0.066 μm/min	4 μm
2	15 mA/cm^2	0.15 μm/min	4.4 μm
3	20 mA/ cm^2	0.2 μm/min	3.75 μm
4	25 mA/cm^2	0.25 μm/min	3.9 μm

3.2 Seedlayers

A seedlayer is a metal layer which serves as the cathode onto which the electroplated metal is deposited. Two types of seedlayers are used in the fabrication of the electromagnetic actuators: a Chrome/Copper seedlayer and a Titanium/Copper seedlayer.

These seedlayers are chosen since they are easily deposited and provide a good substrate on which to electroplate copper and permalloy. Copper is used because it is highly conductive and provides uniform plating, by ensuring a small potential drop across the electroplated wafer. However, its adhesion is poor to the substrates commonly used in fabricating the actuators. These substrates include silicon, silicon dioxide, silicon nitride, and photoresist. To ensure the coppers adhesion to these substrates, an adhesion metal is placed in between the copper and substrate. In our case the metals used are chrome or titanium. These metals adhere well to the copper and to the various substrates described above.

The seedlayers are typically formed on silicon wafers by either evaporation or sputter deposition. Sputter deposition is preferable, since the deposition temperature is low. However, our facilities limit us only to evaporation. The evaporation process involves placing the wafer to be coated in a vacuum chamber together with a metal source. The metal source is then heated, until its atoms evaporate and deposit on the wafer, producing a thin sheet of metal on the wafers.

Chrome / Copper seedlayer

The typical chrome/copper seedlayer we use is formed by evaporating a 100 A thick chrome layer on top of which a 800 - 1000 A copper layer is evaporated. In order to prevent the copper from oxidizing in the air, a second layer of chrome (100A thick) can be evaporated on top of the copper, forming a "sandwich" structure. Note: this top chrome layer should be removed prior to electroplating.

The advantages of using chrome is that it makes an excellent adhesion layer to SiO_2, Si_xN_y (silicon nitride), Si, and Photoresist. This is particularly important when thick electroplated metal layers, with large stresses, are deposited. When compared to titanium

the adhesion of chrome is better. The disadvantage of chrome as an adhesion layer is that it is difficult to selectively wet etch without attacking other metals present. Chrome, especially in contact with copper, tends to form a protective oxide layer. This layer makes the selective etching of chrome difficult. A more complete discussion of chrome etching will be provided in section 3.2.1.

Titanium / Copper seedlayer

The titanium/copper seedlayer is formed by evaporating a 100 A thick titanium layer followed by an evaporation of an 800 - 1000 A copper layer. The advantage of using titanium as an adhesion layer is that its selective wet etching is very easy. Although, like chrome it grows an oxide layer, this layer does not prevent its etching. The disadvantage of using titanium is that its adhesion is not as good as chrome. Electroplated permalloy layers thicker than 15 μm can be easily peeled off.

3.2.1 Selective metal etchants

Several recipes that allow the selective wet etching of the seedlayers while minimizing the etching of the electrodeposited material are presented in the following.

Copper etching

The extent to which an acid ionizes determines its strength. Acetic acid tends to ionize only to a limited extent. The equilibrium equation of acetic acid in water is shown in equation (3.7).

$$CH_3COOH + H_2O \Leftrightarrow H_3O^+ + CH_3COO^- \qquad (3.7)$$

This ionization can be increased by diluting the acid. The following two recipes etch the copper seedlayer uniformly, and rapidly, while etching the electrodeposited copper at virtually the same rate. Note, neither copper recipe attacks permalloy.

	Recipe	Etching time for 800 A copper
Copper etching recipe #1:	100ml H_2O 5ml Acetic Acid 5ml H_2O_2	30 - 45 sec
Copper etching recipe #2:	100ml H_2O 1ml Acetic Acid 1ml H_2O_2	1 - 2 min

Table 3.4: Etching recipes for copper seedlayer.

Titanium etching:

Titanium and titanium oxide layers are easily removed in many etchants. Two etchants we use are shown in table 3.5. A slow controllable etch can be performed using diluted HF, while a very rapid etch is achieved with ammonium hydroxide.

	Recipe	Etching time for 100 A titanium
Slow titanium etch #1:	100ml H_2O 1ml 48% concentrated HF	approximately 1 min (immediately after color has changed to almost a dull gray)
Fast titanium etch #2:	1 part ammonium hydroxide 1 part hydrogen peroxide 6 parts DI water	Fast

Table 3.5: Etching recipes for titanium seedlayer.

Chrome etching:

A commercial chrome etchant can be used in cases where chrome must be etched but there are no metals other than gold present. When metals such as copper or permalloy are

present, the most desirable selective etchant is hydrochloric acid (HCl). The higher the concentration of HCl, the more easily the etching takes place. However, the etching is also less controllable, and at these high concentrations other metals may also be attacked. Sometimes etching can not be achieved, no matter what the concentration. In these cases, a rod of aluminum can be placed in contact with the chrome; this depassivates the chrome allowing etching to proceed.

	Recipe	Etching time for 100A chromium
Transene chrome mask etchant:	commercial product	~ 40 sec
Chrome etchant #1:	100 ml H_20 50 ml HCl	Fast once etching begins (< 30 sec)

Table 3.6: Etching recipes for chrome seedlayers.

3.3 Insulator technology

Insulators are materials which do not permit currents to flow through them. They are used in the semiconductor industry and in MEMS devices to prevent electrical shorting between various conducting layers. The insulators, and the processes used to form them, must be compatible with the conducting layers they are insulating. For example, metal conducting layers can't be coated with insulators which form at temperatures above the melting point of the metal.

Most semiconductor and MEMS devices use silicon as a substrate layer on top of which layers of conductors are deposited. Silicon itself, however, conducts electricity so an insulating layer is often required between it and the subsequent conducting layers. Fortunately, there are many insulating materials which can be used. The simplest insulator is thermal silicon dioxide, which is formed by oxidizing silicon. Silicon oxidation involves heating the silicon to temperatures around 1100 °C in the presence of oxygen or water. When oxidation is performed for several hours, a thin (several 1000 A

thick) layer of oxide is grown on top of the silicon surface. This layer provides excellent electrical insulation. Other insulators can also be used, and they include silicon nitride which is deposited at temperatures of around 800 °C by low pressure chemical vapor deposition [7], low temperature oxide which will be discussed in section 3.3.2, and photoresist.

The conducting layers deposited on top of the silicon are often metals such as aluminum, copper, and gold. The range of insulators that can be used to insulate them is more restricted because of thermal considerations. The deposition temperature of the insulator must be below the melting point of the metal, but often should be much below this. The deposition temperature of the insulator on a metal should be minimized, as heating the metal produces thermal strain, proportional to temperature, in the metal. This thermal strain can cause the metal to buckle or tear away form the layer beneath.

The most common insulators for metals are photoresist which is used in the disk drive industry, and low temperature oxide, used in the semiconductor industry. Other insulators such as silicon dioxide or aluminum oxide can be deposited by sputter deposition. Sputter deposition is a process where a target, a mount holding the material to be deposited, is placed above a silicon wafer in a vacuum chamber. A beam of ions is directed towards the target and dislodges some of the material's atoms, coating the wafer beneath.

The semiconductor industry uses low temperature oxide for insulation to cover thin (less than 1000A) metal, usually aluminum, conductors. Low temperature oxide is chosen because it isquite easy to deposit and pattern, and the conductors used are thin because the typical operating currents are small. The disk-drive industry uses photoresist to insulate between multiple layers of copper coils in their inductive read/write heads. Photoresist is used because it is readily available and simple to process. Relatively thin conductors, about 1 micron thick, can again be used because the required currents are small.

The deflections of the flap actuators, presented in this thesis, are proportional to the currents supplied. Therefore, relatively large currents (at least 100 mA) are desired. This

means that the power dissipated in the conductors is large, unless the cross-sectional area of the conductors is made large. Because of limited real-estate on the actuators, only the thickness of the conductors can be increased. Increasing the thickness of the conductors means that the insulators now must be thicker in order to provide good step coverage. Step coverage is the term used to describe how a material covers a second material configured in the form of a step. In this thesis we use copper conductors and two insulating materials, photoresist and low temperature oxide. These insulators are used in significantly thicker configurations to provide the necessary step coverage.

As a starting insulation material we chose photoresist, because it is simple to work with and does not require complicated equipment or techniques to process, and we were able to successfully fabricate several devices using it. However, we found that it was not thermally stable enough when high currents (above 100 mA) were passed through the conductors. Also, its lack of thermal stability during processing required tedious baking and cooling to prevent it from cracking, so low temperature oxide was the insulating material we next considered. It has excellent thermal stability, but we were concerned that we would not have sufficient step coverage. As we found out, we can easily insulate steps 4 micron high and clearly have the room to cover steps at least up to 10 microns high. In the following we present more detailed discussions on photoresist and low temperature oxide.

3.3.1 Photoresist

Photoresist is a photosensitive material which is used as a patternable masking agent to protect certain regions of a second material while the unprotected regions are etched. It is also used to form molds for electroplating. Usually it is removed once the etching or electroplating steps are complete, but it can also be used as a permanent structural dielectric layer. Photoresist is used as an insulator because the processing and patterning are simple. Also it can be used to planarize rough surfaces by reflowing the photoresist at temperatures above 120 °C. Reflowing is essentially melting the photoresist, causing it to flow from elevated regions into valleys to produce an overall flatter surface.

Conventional optical photoresists are three-component materials. These components are a matrix material (resin), a sensitizer (inhibitor), and a solvent [8]. The matrix material serves as a binder, and establishes the mechanical properties of the film. It provides the resist film with its adhesion and etch resistance, and other film properties such as thickness, flexibility, and thermal flow stability. The sensitizer is a photoactive compound, which reacts to UV radiation, and the sensitizer gives the resist its developer resistance and radiation absorption properties. The purpose of the solvent is to keep the photoresist in a liquid state until it is applied to the substrate being processed. Much of the solvent is removed when the photoresist is spun on to the wafer, and the remainder is removed during baking. If the photoresist is baked for sufficiently long times and at sufficiently high temperatures, the photoresist will fully polymerize the matrix material. The photoresist will then act as an excellent dielectric which can remain as part of a permanent device structure.

The photoresists we use are AZ 4400 and AZ 4620. These are positive photoresist made by Hoechst. Positive photoresists have a sensitizer which, when exposed to UV light, weakens the matrix material allowing it to be removed in developer. These photoresists have exceptional transparency which allows 6 -15 μm films to be exposed with 200 - 400 mJ/cm^2; they also have broad spectral sensitivity and superior response to exposure sources ranging from 310 - 436 nm. These photoresists are suitable for contact, proximity or projection printing, and have good thermal stability compared to other makes of photoresist [8].

As mentioned previously the photoresist is used for insulation between layers of copper or permalloy on the flap actuators. A special baking process is carried out on the photoresist to reduce its thermal sensitivity during processing, and when large currents are passed through the conductors. In this baking process (table 3.7) the wafer is slowly heated from room temperature to 190 °C, baked at this temperature for a period of two hours, and then slowly cooled back down to room temperature. Slow heating and cooling allows some of the thermally induced strain in the photoresist to relax, preventing the photoresist from cracking. Once the photoresist has been through the high

temperature bake, it can withstand a subsequent heating up to about 170 °C without cracking or deforming. Stability of the resist, however, can not be ensured when more than two layers of insulators are used. To apply two insulators the high temperature bake of the second insulator must be done only to a maximum temperature of 170 °C. The photoresist is not able to take more than two high temperature cures; after more than two cures it cracks.

Ramp 90 => 190 °C (2 hours)
leave at 190 °C 2 hours
Cool 190 °C => room temperature (4 hours)

Table 3.7: High temperature baking recipe for AZ photoresist.

A new photoresist [9,10] recently developed at IBM T.J. Watson research center is SU-8. This resist is versatile, it allows high-aspect ratios, can be coated in very thick layers, up to about 1 mm, and is a negative resist sensitive to UV light in the 400 nm range. It is attractive for use in the MEMS flap actuators because it is reputedly more thermally stable than AZ photoresist (with a T_g greater than 200 °C when fully cured). Careful investigation of SU-8 is necessary to determine if indeed it can be used reliably in the fabrication of the MEMS flap actuators.

3.3.2 Low Temperature Oxide (LTO)

While photoresist can be used as an insulator for the flap actuators, its inherent thermal instability does not make it the optimal insulation material. We now explore LTO, low temperature oxide, which makes a much better insulator.

Low temperature oxide (LTO) films are basically silicon dioxide films, but they can be deposited at temperatures between 300 and 450 °C, not the 1000 - 1200 °C required for thermal SiO_2. They make excellent insulators despite the fact that their quality is

somewhat inferior to thermal silicon dioxide. They exhibit lower density than thermal SiO_2 and substantially higher etch rates in buffered hydrofluoric acid solutions, but because of their low deposition temperature, they are suitable as insulators for metals such as aluminum and copper. The deposition temperature is too high, however, for permalloy. At this temperature, the stress in the permalloy is very high and the permalloy curls or pulls off the substrate.

Low temperature oxide is formed by low-pressure-chemical-deposition (LPCVD). Chemical vapor deposition (CVD) is defined as the formation of a non-volatile solid film on a substrate by the reaction of vapor phase chemicals (reactants) that contain the required constituents [11]. A CVD process occurs as follows, a given composition and flow rate of reactant gases and dilutent inert gases are introduced into a reaction chamber. The gas species move to the substrate and the reactants are adsorbed on the substrate. The adatoms undergo migration and film-forming reactions and finally the gaseous by-products of the reaction are desorbed and removed from the reaction chamber. If the CVD deposition is done at low pressure (LPCVD), it is found that better uniformity and step coverage are achieved, and the quality of the film is also better with less particulate contamination. The low pressure increases the diffusivity of the reactant gas molecules so that mass-transfer to the substrate does not limit the film growth rate, rather the film growth rate is determined by the surface reaction rate.

Low temperature deposition of SiO_2 is achieved by reacting silane, SiH_4, with oxygen to form undoped SiO_2 films, as shown in equation (3.8), at temperatures between 350 °C - 450 °C.

$$SiH_4 + O_2 \Rightarrow SiO_2 + 2\,H_2 \qquad (3.8)$$

The deposition conditions for LTO are given in table 3.8. The deposition temperature is kept to a minimum possible, in order to minimize the heating of the metal layer. Note, at this temperature the deposition rate is lower when compared to LTO deposited at 450 °C. Figure 3-9 is an SEM picture showing a cross-sectional view of two copper conductors insulated from each other by an LTO layer. The LTO layer appears as a black line. This

picture shows the excellent step coverage achievable with LTO. The LTO is 1.6 microns thick and covers a 4.5 μm thick layer of copper. The step coverage is excellent, in fact, a thinner LTO insulation film could have been used to cover this copper step.

	Temperature	Silane flow rate	O2 flow rate	deposition rate
LTO deposition	380 °C	42.8 sccm	31.0 sccm	0.48 μm/hr.

Table 3.8: LTO deposition parameters.

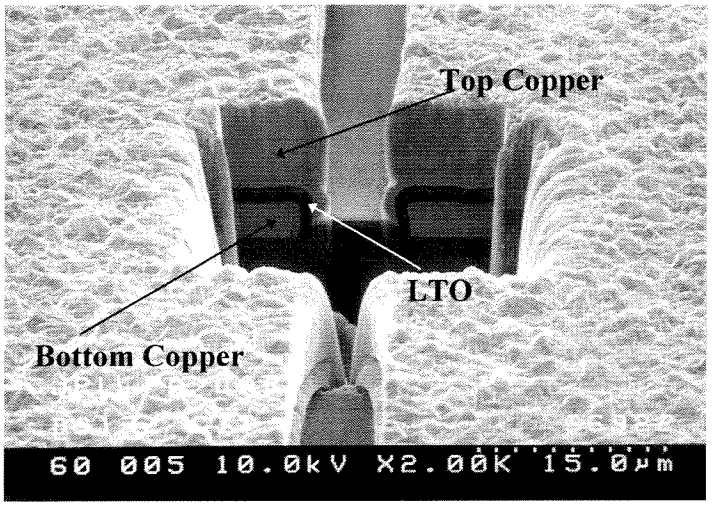

Figure 3-9: Cross-section of two copper conductors, showing "sandwiched" insulating LTO layer.

3.4 Bulk silicon micromachining

The mechanical structures of the electromagnetic flap actuators are carved out of silicon wafers. This process of selectively removing silicon from the wafer bulk is know as bulk silicon micromachining. The silicon can be removed by two methods, either wet chemical etching or dry etching. As the name implies, wet chemical etching uses liquids to etch the silicon while dry etching uses gasses.

Wet etching is commonly used because it is a low cost, reliable, high throughput process. The major steps in the etching process involve the diffusion of the reactant to the reacting surface, followed by a chemical reaction at the surface, and then the diffusion of the reaction products away from the surface. In order to etch only selective regions of a silicon wafer, a mask is used. The mask is a material applied to the wafer, which is not attacked by the silicon etchant, and protects the silicon under it from being etched. The silicon regions not protected by the mask are etched when the wafer is placed into the etchant. Once the silicon etching is complete the mask material is removed.

The wet silicon etchants are divided into two basic types, isotropic wet etchants and anisotorpic wet etchants. Isotropic wet silicon etchants etch the silicon at a uniform rate in all directions while the anisotropic wet silicon etchants etch certain crystallographic planes of the silicon faster than others. Isotropic silicon etchants are usually made of mixtures of nitric acid and hydroflouric acid with acetic acid often added to dilute and buffer the etchant. The limitation of isotropic etchants is that they can not be used to define features less than about 3 μm wide, and mechanical structures that are formed have rounded corners and curved walls. For many mechanical devices straight, vertical, walls and sharp corners are desired. For example, a silicon micromachined rectangular waveguide should have straight side walls and sharp corners, but by using isotropic etching only a rounded cavity can be formed. Anisotropic silicon etching enables formation of straight walls which form along the <111> crystal plane of the silicon. This is because silicon has a diamond lattice structure in which the silicon atoms in the <111> planes have more atomic bonds than in the <100> or <110> planes. The anisotropic etchants as a consequence can etch more easily through the <100> and <110>, so these planes get etched while the <111> plane can remain.

Anisotropic etching is used in the fabrication process of the flap actuators to form a thin (25-50 μm) silicon membrane. To form the membrane, a silicon dioxide mask covers the wafer except at certain regions. In these regions the silicon is exposed and etched in an anisotropic etchant to form the membrane. The types of anisotropic etchants used will be discussed in detail in section 3.4.1. There are two ways to control the

thickness of the membrane. One is simply by controlling the silicon etching time, knowing the rate of the etching. The other is to use a boron etch stop layer so that etching is virtually terminated when the etch stop layer is reached. A boron etch-stop layer is a heavily (around 10^{20}) boron-doped silicon layer. This layer is etched very slowly, compared to undoped silicon, by certain anisotropic etchants. By burying a boron layer at a certain depth below the top surface of a silicon wafer and etching the silicon from the bottom side of the wafer, a membrane can be formed. The thickness of the membrane depends on how deeply the boron is buried beneath the top of the silicon wafer. Formation of a membrane using the boron etch stop method is simple, since the silicon on the bottom side of the wafer will be etched until the boron etch stop layer is reached. Once the boron layer is reached, etching will virtually stop and the membrane is automatically formed without the requirement for careful time control. Membranes formed using boron etch stop layers have smoother bottom surfaces than timed etched wafers, and the membrane uniformity is also much better. Once the membrane is formed, the boron etch stop layer is often removed, since its presence increases the stress in the membrane. To etch the boron etch stop layer, an isotropic silicon etchant is used (1 part HF : 3 parts Nitric acid : 8 parts Acetic acid). This etchant is slightly modified from the standard silicon etchants, so that it etches boron doped silicon much faster than undoped silicon.

Since features less than 3 microns wide and more than 3 microns deep can not be formed using isotropic etchants, and anisotropic etchants depend on the crystalline orientation of the wafer, a different etching method, known as dry etching, was developed. It enables finer control of the etching process, without dependence on the crystalline orientation of the wafer. While there are many dry etching processes, we concentrate here on reactive ion etching, which allows anisotropic silicon etching using a gas. The reactive ion etching process will be discussed in section 3.4.2. It is used in this thesis to carve the spring and plate structures of the flap actuators from the silicon membrane.

3.4.1 Wet anisotropic silicon etchants

The three anisotropic etchants we use to fabricate the actuators are ethylene-diamene-pyrocatachol (EDP), potassium hydroxide (KOH), and tetramethyl- amonium-hydroxide (TMAH).

EDP - [12] is an organic etchant which contains ehylenediamene, water, pyrocathechol, and pyrazine as a catalist. This mixture is found to etch silicon when heated to temperatures around 100 °C (for the type-F solutions). The ratio of etching rates for the different planes are $R_{<100>}:R_{<110>}:R_{<111>} = 17:10:1$. The advantages of using EDP over other anisotropic etchants are that a heavily doped boron layer provides an excellent etch stop, $R_{Si} : R_{(B+ \text{ doped Si})} = 500:1$. EDP does not attack most metals and it etches SiO_2 very slowly. SiO_2, which is easily formed, can be used as a mask ($R_{SiO2}:R_{si<100>} = 1:1000$). Unfortunately, EDP is undesirable since it is known to cause cancer and its anisotropy is not as high as that of KOH, so perfectly vertical walls can't be made.

KOH- [13] is an inorganic alkaline etchant, easily handled, and much safer than EDP. Concentrations of 30 - 60% wt of KOH diluted in water are normally used. At lower concentrations the surface becomes rough and a white residue deposits on the silicon unless isopropyl alcohol is added. For our applications low concentrations (around 20%) are desired since the etching at these concentrations is more controllable. The recipe for the KOH etchant we use is given in table 3.9.

The KOH etching selectivity of the <100> and <110> planes to the <111> planes is much higher than for EDP which enables highly vertical walls to be formed in the silicon. Handling of KOH is much simpler than EDP because the chemical is relatively safe. A disadvantage of using KOH is that it attacks SiO_2 much faster than EDP making it more difficult to use SiO_2 as a masking material ($R_{SiO2}:R_{si<100>} = 1:200$). The KOH solution also attacks boron-doped silicon much more rapidly than EDP, so boron etch stop layers are not nearly as effective in this case. Finally, most metals are attacked in KOH, so they must be protected during the etching process.

	Composition	Temperature	Etching Ratio	Etch Rate (100)
KOH etch	1.44 l KOH (45%) 1.45 l water 0.05 l isopropyl alcohol	58 °C	<100> /<111> 400 : 1	24 μm / hr

Table 3.9: KOH etching parameters.

TMAH- [14] is also an alkaline inorganic etchant. It is typically used in concentrations between 5 - 40% and at temperatures ranging from 60 to 90 °C. The selectivity between the <100> and <111> planes, shown in table 3.10, is not as high as that of KOH but better than EDP. However, it has a higher selectivity over silicon dioxide when compared to both EDP and KOH (R_{SiO2}:$R_{si<100>}$ =1:5000), so silicon dioxide makes a very effective masking material. TMAH, like KOH, is a much safer etchant than EDP.

	Composition	Temperature	Etching Ratio <100> /<111>	Etch Rate (100)
TMAH etch	1500 ml 25% TMAH 1000 ml DI water	90 °C	20 :1	45 μm/hr

Table 3.10: TMAH etching parameters.

3.4.2 Reactive ion etching

Reactive ion etching is an anisotropic dry etching process where gasses rather than wet chemicals are used for etching. We choose the gases based on the reactive species they form when they are excited into a plasma. To excite the gases into a plasma, an rf signal is applied between two electrodes across the gas. The reactive species produced in the plasma then chemically react with the material to be etched, in our case silicon, producing volatile products. If one of the electrodes is grounded, while the other is left floating, the plasma becomes positively charged, while the floating electrode becomes

negatively charged. The potential difference between the plasma and the negatively charged electrode attracts the ions from the plasma. The ions bombard the negative electrode and when a wafer is placed on this negative electrode, it too will be bombarded by the ions. So the RIE uses two mechanisms to etch. One is physical etching of the silicon due to bombardment of the silicon by ions produced in the plasma. The other etching mechanism is a chemical reaction between the reactive ion species and the wafer material. Reactive ion etching is highly anisotropic, and etching can be controlled very precisely, which makes it easy to do VLSI as well as MEMS patterning. For our application reactive ion etching is used to define the spring and flap structures, Figure 3-10, and the silicon is etched in a combination of SF_6 and O_2 gasses; the two recipes used are listed in table 3.11.

RIE Si etch	SF6 : % O2 (sccm) (sccm)	Incident Power	Etch Rate
Recipe #1	1.794 : 2.3	600 W	3000 A/min
Recipe #2	1.391 : 4.32	600 W	1 μm/min

Table 3.11: RIE etching recipes.

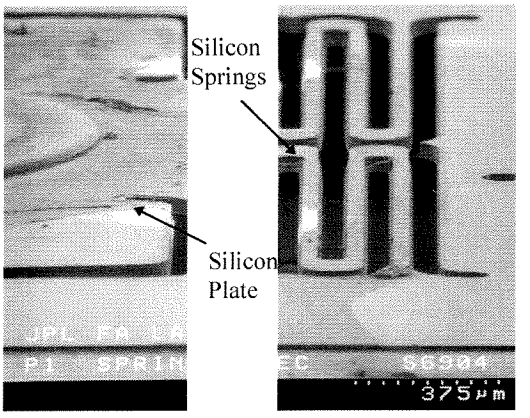

(a) (b)

Figure 3-10: (a) SEM showing part of RIE etched silicon plate.
(b) SEM showing RIE etched silicon springs.

References

[1] J. B. Mohler, *Electroplating and Related Processes*, Chemical Pub. Co., New York, 1969.

[2] W. Blum and G.H. Hogaboom, *Principles of Electroplating and Electroforming 3rd ed.*, McGraw-Hill, New York, 1949.

[3] D. B. Hibbert, *Introduction to Electrochemistry*, Macmillan Press LTD, London, 1993.

[4] F. A. Lowenheim, *Modern Electroplating*, John Wiley & Sons, Inc., Second Edition, 1963.

[5] I. W. Wolf, "Electrodeposition of Magnetic Materials," *Journal of applied physics supplement,* Vol. 33 (3), 1962.

[6] N. C. Anderson and C. R. Grover, Jr., "Electroplating of nickel-iron alloys for uniformity of nickel/iron ratio using a low density plating current," *United States Patent # 4,279,707*, July, 1981.

[7] S. Wolf and R. N. Tauber, *Silicon Processing for the VLSI Era Vol.1*, Lattice Press, 1986.

[8] AZ photoresist product catalogue, Hoechst AG.

[9] N. C. LaBianca, J. D. Gelorme, et al., "High Aspect Ratio Resist Chemistry for MEMs Applications," *Proceedings, Fourth International Symposium on Magnetic Materials, Processes, and Devices*, Vol. 95 (18), pp. 386-392, 1996.

[10] M. Despot and H. Lorenz et. al., "High-Aspect-Ratio, Ultrathick, Negative-Tone Near-UV Photoresist for MEMs Applications," *Proceedings, IEEE Micro Electro Mechanical Systems Meeting, MEMS'97*, pp. 518-522, 1997.

[11] S. wolf and R. N. Tauber, *Silicon Processing for the VLSI Era Vol.1*, Lattice Press, 1986, pp. 407 - 458.

[12] R. M. Finne and D. L. Klein, "A Water-Amine-Complexing Agent System for Etching Silicon," *J. Electrochemical Society*, pp. 965-970, September, 1967.

[13] K. Bean, "Anisotropic Etching of Silicon," *IEEE Transactions on electron devices*, Vol. 10(25), pp. 1185-1191, 1978.

[14] U. Schnakenberg, W. Benecke, and B. Lochoel, "NH4OH-based Etchants for Silicon Micromachining," *Sensors and Actuators vol. A21-A23* , pp. 1031-1035, 1990.

[15] W.R. Runyan and K.E. Bean, *Semiconductor Integrated Circuit Processing Technology*, Addison-Wesley Publishing Company Inc., New York, 1990, pp. 269.

Chapter 4

Design and Fabrication of the Flap Actuators

Many applications require mm-sized actuators. These include laser beam scanners and large displacement switches which are discussed in chapter 6. It is very attractive to fabricate these actuators using micromachining techniques because of the inherent benefits associated with MEMS. However, relatively few mm sized MEMS actuators have been built so far. This is due to the lack of actuation technologies which are capable of deflecting such large sized devices, and also because the fabrication of these large mm sized devices is more complicated than for smaller devices, in terms of maintaining flatness and uniformity throughout the device. The MEMS flap actuators developed in this thesis target the mm range and are made possible by electromagnetic actuation.

The actuators developed are larger than 16 mm^2 and can be divided into three types according to the electromagnetic actuating components they include. The first type of actuators (type-1) use a permalloy layer for actuation. This layer is located on a movable silicon plate which is connected by springs to the bulk silicon. In the second type of actuators (type-2), the permalloy layer is replaced by planar copper coils capable of conducting currents. Finally, the third type (type-3) of actuators combine a permalloy layer with planar copper coils.

4.1 Permalloy-only actuators

4.1.1 Design

The type-1 actuators consist of silicon micromachined flaps onto which layers of permalloy are electroplated. Two designs of these permalloy-only actuators have been developed. They differ in the geometric configuration of the permalloy layers, which are used to induce the magnetic actuation. The mechanical structure of both these actuators consists of a single-crystal silicon plate, 4 mm × 4 mm × 0.04 mm, tethered to the bulk silicon substrate by two serpentine springs.

The type-1a actuator shown in Figure 4-1 has a 3 mm × 3 mm permalloy layer located on the bottom side of the plate, and a permalloy mesh structure which sits along the perimeter of the top side of the plate. The purpose of the mesh structure is to constrain the actuator to deflect only above the substrate. In this actuator most of the top surface is free of permalloy and can serve as a high quality mirror reflector. The type-1b actuator, shown in Figure 4-2, has a simpler design; it only has a 3 mm × 3 mm permalloy layer which is located on the top side of the plate.

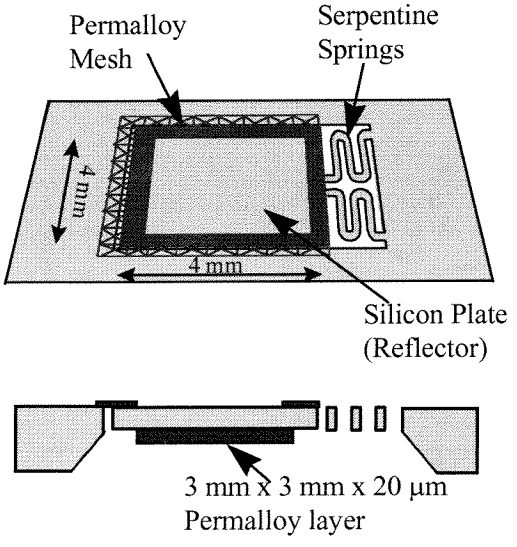

Figure 4-1: (a) Type-1a actuator
(b) Cross-sectional view of type-1a actuator.

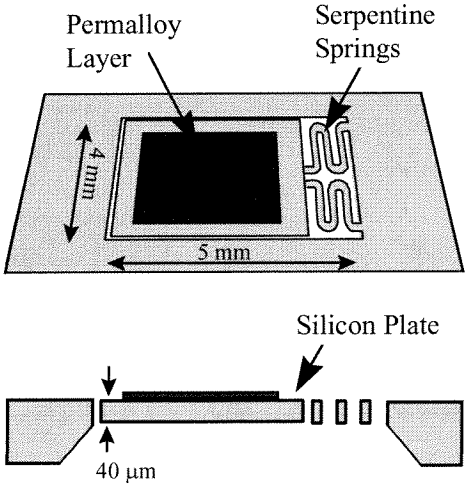

Figure 4-2: (a) Type-1b actuator
(b) Cross-sectional view of

type-1b actuator.

4.1.2 Fabrication

Here we discuss the fabrication steps, shown in Figure 4-3, for the permalloy only actuator denoted as type-1a in the previous section. The fabrication steps involved in making the type-1b actuator are a subset of the type-1a actuator steps. Processing begins with the formation of a 40 μm thick silicon membrane which will become the silicon plate and springs. We start with a <100> silicon wafer which is oxidized and coated with photoresist. The photoresist is patterned to expose a rectangular region of the oxidized wafer. The silicon dioxide in the opened area is then etched in buffered hydrofluoric acid exposing the bulk silicon. An ethylene-diamine pyrocatechol (EDP) bath anisotropically etches the exposed silicon to form a 40 μm thick epitaxial silicon membrane. Etching is halted by a buried boron etch-stop layer. In this process the silicon dioxide acts as a mask during the bulk silicon etching. In the next step the boron layer is removed and a new oxide layer is grown. A Ti/Cu seedlayer is then evaporated on the bottom side of the silicon plate, a photoresist mold is formed on top of it, and 20 μm of permalloy is electroplated. The photoresist and seedlayer are stripped using the etchants described in chapter 3. A second Ti/Cu seedlayer is evaporated this time on the top side of the mirror, and a 10 μm permalloy mesh structure is electroplated. This mesh extends beyond the intended 4 mm x 4 mm borders of the plate.

Freeing of the actuator from the substrate requires two steps. First, in the areas outside the plate region the permalloy mesh is detached from the silicon substrate by etching away the underlying oxide layer with a buffered HF etch. Then, the plate and springs are lithographically patterned on the membrane, and free-released by reactive-ion-etching (RIE). In this RIE step, the silicon under the permalloy mesh is also etched so as to free the mirror from the substrate. The mesh remains overhanging the edge of the freed plate, and serves two purposes. First it constrains the actuator to deflections above the plane. Second, the mesh improves the shock resistance of the actuators, which allows actuators with softer springs, hence larger deflections at lower magnetic

fields. In the case when the actuator is to be used as a scanning mirror, a thin, 200 nm layer of aluminum is evaporated on the top surface of the silicon plate.

The fabrication steps for the type-1b actuator involve only the formation of the 40 μm thick membrane, followed by a single deposition of a 5 μm thick permalloy layer on the front surface of the plate. This is followed by an RIE etch to define and release the actuator plate and springs. Additional process details are provided in appendix A.1. Figure's 4-4 and 4-5 show the fabricated type-1 mirrors deflected due to externally applied magnetic fields.

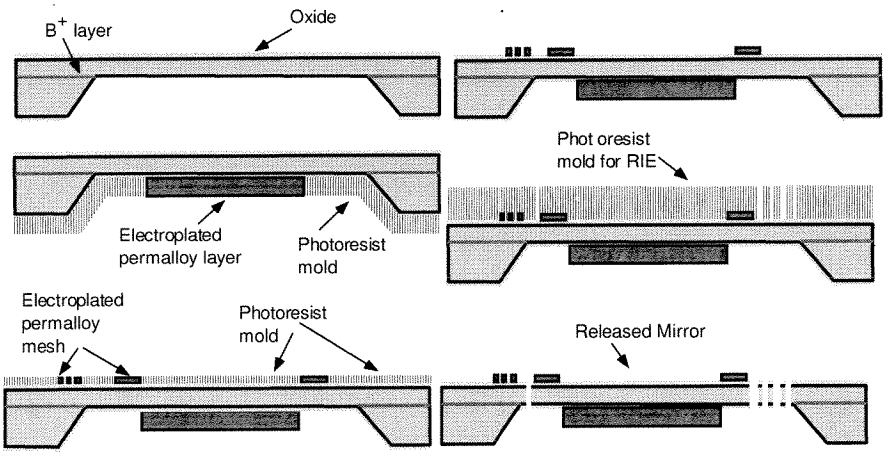

Figure 4-3: Type-1a actuator fabrication steps.

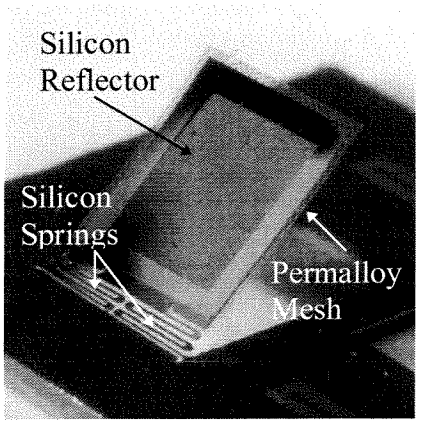

Figure 4-4: Photograph of deflected type-1a actuator.

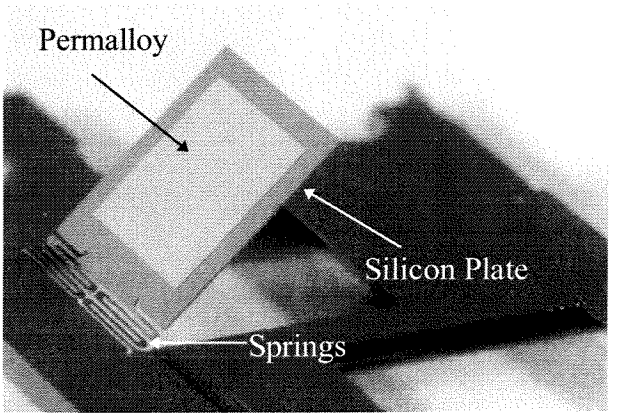

Figure 4-5: Photograph of deflected type-1b actuator.

4.1.3 Processing issues

There are several issues worth mentioning concerning the fabrication of the type-1 actuators. The first relates to permalloy in the presence of hydrofluoric acid. The release step for the permalloy mesh of the type-1a actuator requires that the oxide under the mesh be undercut. During this process the permalloy is exposed to hydrofluoric acid for a relatively prolonged time (around 10 min). It is found that if the oxide is etched in a hydrofluoric acid diluted only in water, the permalloy is attacked and becomes pitted in less than 5 minutes. If only buffered hydrofluoric acid is used instead to etch the oxide, the permalloy withstands the etchant for much longer (at least 20 min).

The second issue pertains to reactive ion etching of the actuator spring and plate structure. In order to ensure that the entire actuator structure is released at the same time, the photoresist pattern defining the plate and spring must have equal amounts of silicon exposed. If the amount of silicon exposed during RIE is different at different locations of the actuator, then over-etching in some regions of the actuator will occur. Even using a uniform photoresist pattern RIE over etching still occurs. Figures 4-6 through 4-8 show a careful examination of the RIE etch results for a type-1b actuator. A portion of the spring is cut out using ion milling, as shown in Figure 4-6. It is turned bottom side up so that the bottom surface of the spring can be examined. Figure 4-8 shows an enlarged view revealing many small pits. The pits, the result of over etching, are undesirable because they weaken the silicon spring structure and reduce the surface quality of the silicon plate when used as a mirror. For the case of the type-1a actuator, the over-etching is even more severe than for the type-1b actuators. In this case, to separate the silicon plate from the rest of the membrane, the RIE etching must be done not only in the exposed silicon regions but also where the silicon is covered with the permalloy mesh. The silicon regions covered with permalloy must be undercut from the side, which takes a long time and exposes the bottom side of the plate and springs to the etchant for long periods of times, producing extensive pitting. To eliminate the pitting a photoresist layer can be coated on the bottom side of the membrane prior to RIE etching. The photoresist then

protects the underside from being attacked and provides, once the photoresist is removed, a smooth silicon surface.

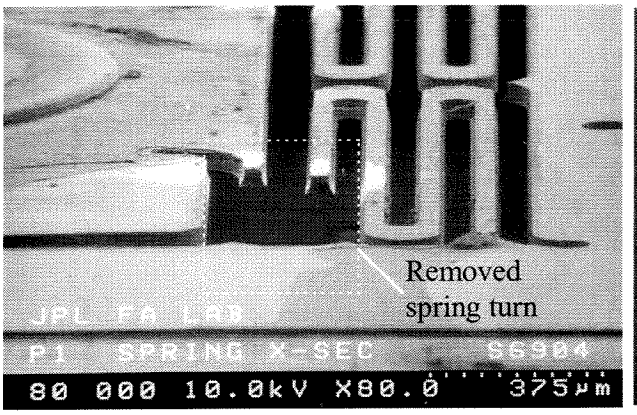

Figure 4-6: Silicon plate and spring with part of the spring ion milled off.

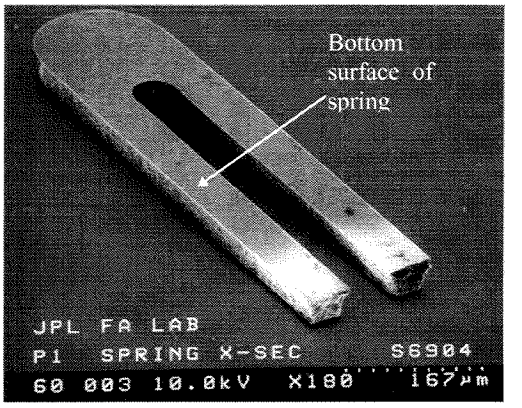

Figure 4-7: Part of spring detached from actuator and flipped bottom side up.

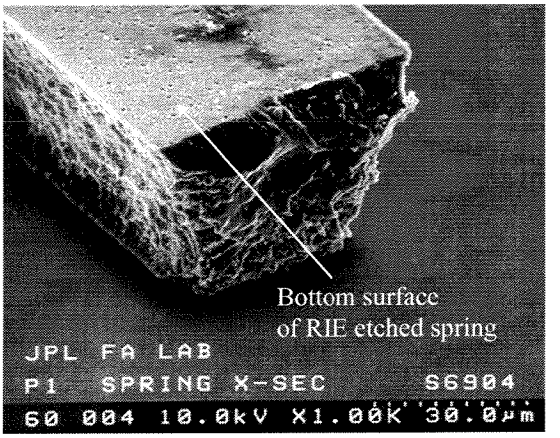

Figure 4-8: Enlarged view, showing damaged bottom surface of RIE etched spring.

4.2 Coil-only actuators

The type-1 actuators previously described, however, require an external electromagnet to generate the variable magnetic fields. These electromagnets are large (at least 3 cm × 2

cm × 2 cm) and have high power consumption. For applications requiring low power (less than 100 mW) and small package size (~ 2 cm^3), actuators utilizing on-board planar coils are more desirable. For this design, a small permanent magnet can be used to generate a fixed field, while actuation is provided by mA currents passed through on-board coils. An additional advantage of these actuators is their ability to be individually addressed in an array. If a fixed external field is applied to an array of these actuators, an individual actuator can be addressed by supplying current only to this actuator.

4.2.1 Design

Two types of coil-only actuators have been developed, a cantilever-type actuator (type-2a), and a torsional-type actuator (type-2b). The mechanical structure of the cantilever-actuator is a silicon plate, 4 mm × 4 mm × 25 μm, supported by four (25 μm thick, 40 μm wide) silicon cantilever beams, as shown in Figure 4-9. The four beams provide redundancy to allow actuator operation even if one or two of the beams break. The electromagnetic actuating component, a 70-turn planar double copper coil, electroplated in two layers, sits on the bottom side of the silicon plate. A hardbaked layer of photoresist is used as an insulator between the coil layers.

The torsional-type actuator, designed for increased shock resistance, shown in Figure 4-10, consists of a clamped-clamped beam (8 mm × 80 μm × 30 μm) supporting two (4 mm × 4 mm) 30 μm thick silicon plates symmetrically arranged. A set of 70-turn double coils, insulated with LTO, is located on the bottom side of each plate. On the top side of each plate a micromachined mirror is attached (Figure 4-9c). The fabrication steps for the mirror will be discussed in chapter 6. Although the mirror is not an integral part of the actuator, the actuators are characterized with these mirrors mounted. When we refer to the type-2a or type-2b actuators, we are referring to the actuator and mirror assemblage.

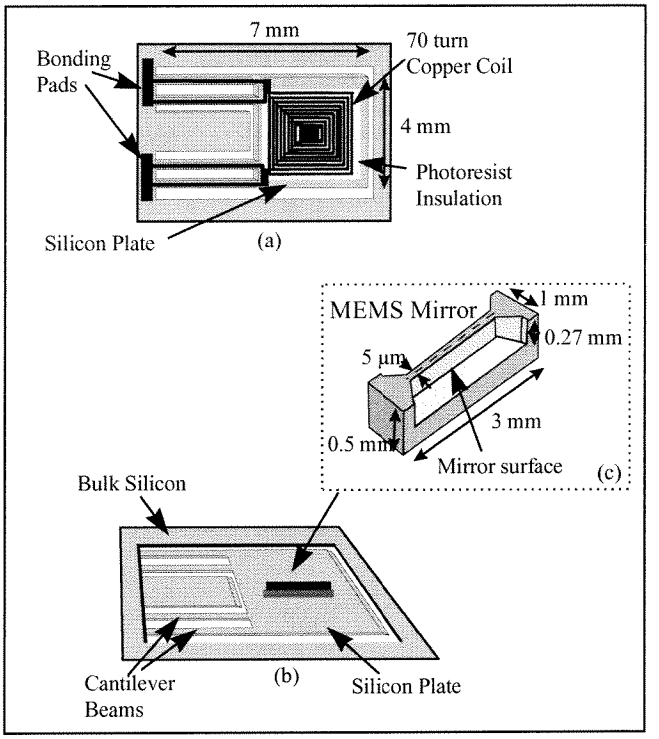

Figure 4-9: (a) Bottom view of cantilever type actuator (type-2a). (b) Side view of type-2a actuator. (c) MEMS mirror which is mounted to the top surface of the silicon plate.

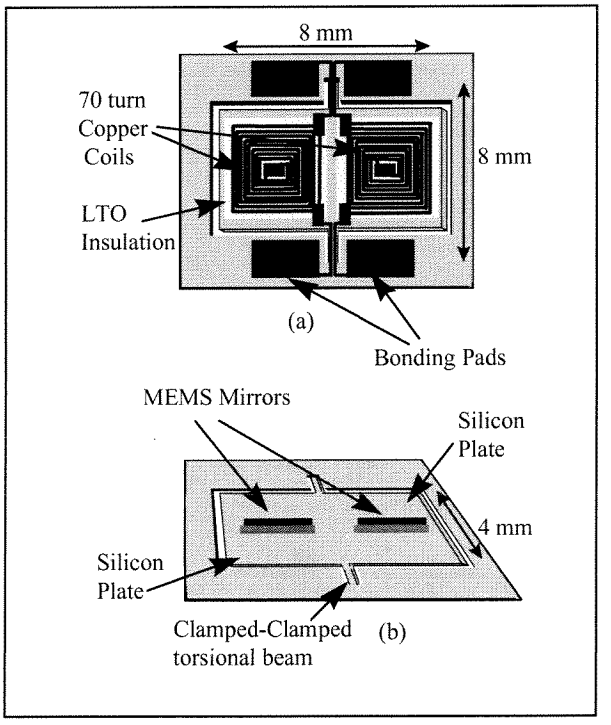

Figure 4-10: (a) Bottom view of torsional type actuator (type-2b). (b) Side view of the type-2b actuator with mounted mirrors.

4.2.2 Fabrication

The fabrication steps for both torsional and cantilever coil-only actuators are very similar and illustrated in Figure 4-11. The only differences are in the dimensions, geometric configuration of the devices, and the insulation material used between the coils. The first step in the fabrication process is to oxidize a double side polished <100> silicon wafer with a 2 μm thick oxide layer. Then the oxide layer on the back of the wafer is patterned and etched in the region where the silicon membrane is desired. The exposed silicon is etched in KOH at 58 °C for 24 hours until a membrane 30 μm thick is produced. Once the membrane is formed, the oxide is stripped, and a 2000 angstrom layer of LPCVD Silicon Nitride (Si_xN_y) is deposited on both sides of the wafer for electrical insulation. Next a chrome/copper seedlayer is evaporated on the top side of the membrane and coated with AZ 4400 photoresist which is patterned to form a mold for the first layer of 30 turn copper coils. 3 - 6 μm thick copper coils are electroplated. After that the photoresist and seedlayer are stripped. The next step is to use either 10 μm of photoresist, or LPCVD LTO (Low Temperature Oxide, 1.6 μm) to insulate the coils. In the case of photoresist insulation, the contact hole, connecting the first layer of coils with the second layer of copper, is patterned in the photoresist, and is hardbaked. In the case of LTO insulation the contact hole must be etched in the LTO after it has been deposited. Once the insulation is in place and a contact opened, a second seedlayer is evaporated and coated with photoresist. The resist is patterned to form a mold for the second layer of copper coils. The coils are then electroplated 8-16 μm thick and the photoresist and seedlayers removed. Finally, the wafer is coated with a thick layer of photoresist which is patterned to define the actuator and expose the nitride layer. The exposed nitride and silicon beneath it are RIE etched to release the actuators. The photoresist is removed, in photoresist stripper, and the micromachined mirrors are attached to the top of the silicon plate. Further process details are presented in appendix A.2. Figures 4-12 and 4-13 show the fabricated type-2 actuators.

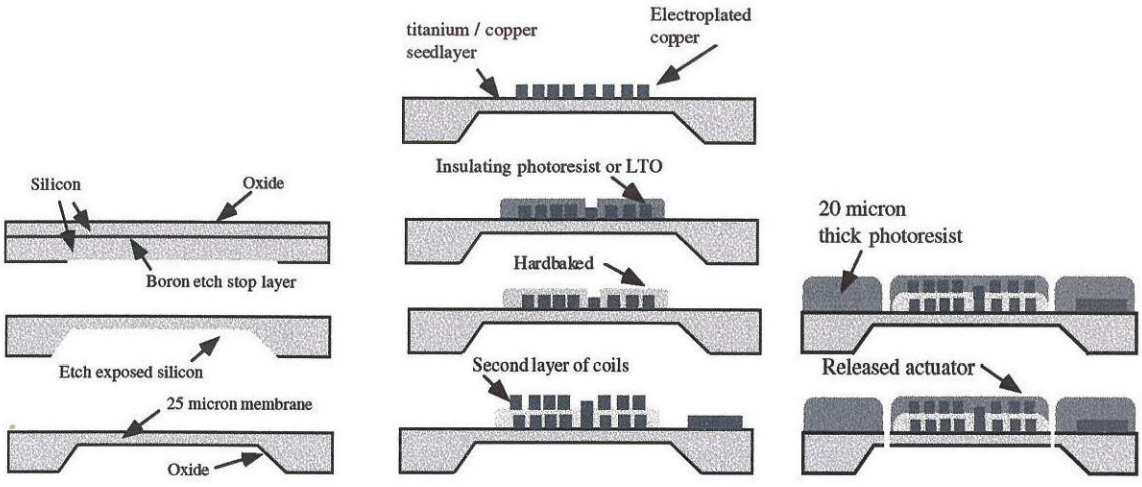

Figure 4-11: Type-2 actuator fabrication steps.

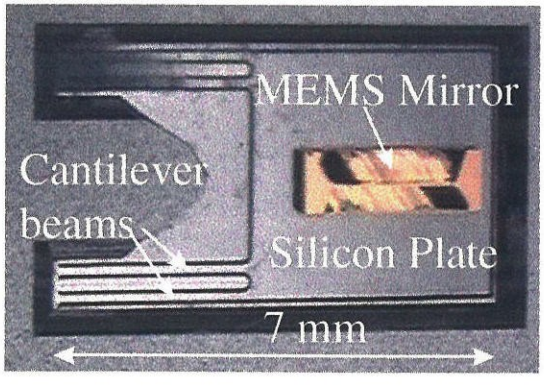

Figure 4-12: Fabricated type-2a actuator.

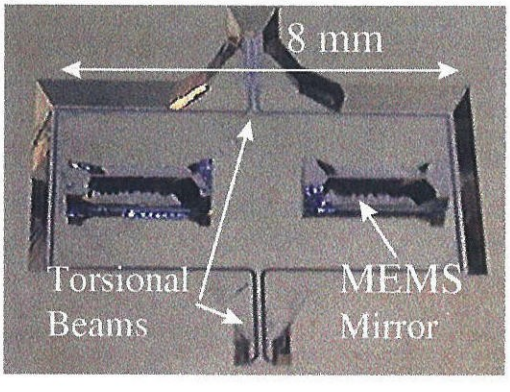

Figure 4-13: Fabricated type-2b actuator.

4.2.3 Processing issues

Although photoresist has been used successfully in the type-2a actuators, it is not the ideal insulation material for the flap actuators. If photoresist is used, extreme care must be taken to prevent the resist from cracking during processing. When photoresist is in contact with metal, and this structure is subjected to heating and cooling over short times,

the photoresist may crack. This is due to the strains, and stresses, produced in the photoresist, due to the difference in thermal expansion coefficients of the metals and photoresist. If the photoresist metal structure is instead slowly heated and cooled, the strains and stresses can relax to a greater extent, and the photoresist won't crack. To prevent the resist from cracking during thermal evaporation, the metal should be evaporated at the slowest rate possible (approximately, 0.1 A/sec for titanium).

Replacing the resist with LTO makes the process more robust. However, one must be careful to ensure that the contact hole, via, between the bottom conductor and the top conductor is free of LTO. This poses a difficulty since LTO is for the most part transparent. The best method I have found to ensure that the via is free of LTO is to dip it for a short time (10- 20 sec) in a copper etchant. The indication that all the LTO has been removed is that the color of the bottom copper conductor in the via becomes bright brown-gold from a dull-dark brown.

In the type-2 actuator fabrication process we replace the EDP anisotropic etchant with KOH because KOH is a much safer chemical to use. In the case of EDP we use a buried boron-doped etch stop layer. When the EDP reaches this layer etching effectively stops. This makes the processing very simple since all we do is place the wafer in the etchant and come back when all the boron etch stop layer is exposed (i.e., we automatically end up with a smooth surface). Using KOH is more difficult since the control of the membrane is done by timing the etch. As the thickness of the membrane approaches the target thickness, we must repeatedly remove the wafer from the etchant and measure its thickness until the desired thickness is achieved.

4.3 Coil and permalloy actuators

4.3.1 Design

The third type of actuators developed combine both a copper coil and a permalloy layer on the silicon plate. This enables the type-3 actuators to be operated in a more versatile way. By varying the external magnetic field strength, coarse control of the

actuator can be achieved. Fine control is accomplished by adjusting the onboard coil currents.

The type-3 actuator, shown in Figure 4-14, consists of a silicon plate 4 mm × 4 mm × 0.04 mm in size tethered to the bulk silicon substrate by two serpentine springs, similar to the type-1 actuators. On the top side of the plate are the electromagnetic components which consist of a 30-turn copper coil and a layer of thin-film permalloy (NiFe) both of which are used to provide the actuation forces.

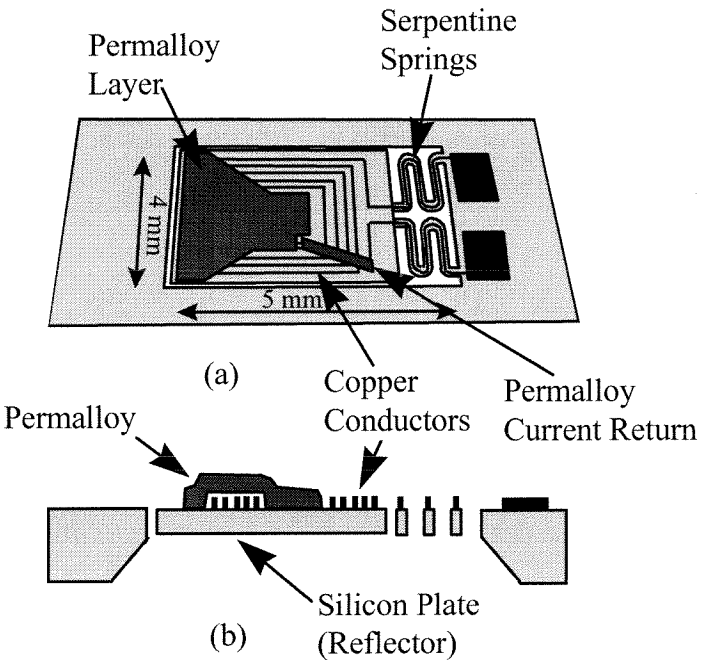

Figure 4-14: (a) Top view of type-3 actuator.
(b) Cross-sectional view of type-3 actuator.

4.3.2 Fabrication

The fabrication steps for the type-3 actuators, illustrated in Figure 4-15, also involve the formation of a 40 μm thick membrane as described for the type-1 mirrors. A Ti/Cu seedlayer is evaporated on the top side of the membrane. A photoresist mold is formed, and a 30-turn planar copper coil is electroplated (9 μm thick). Next an

insulating photoresist layer is coated, patterned and hard-baked. A Ti/Cu seedlayer is again evaporated, a photoresist mold is formed and an 11 μm thick permalloy layer electroplated. Here, a small piece of permalloy (as shown in Fig. 4-14a) serves as a current return path when current is provided to the coil. Finally a thick layer of photoresist is coated and the spring and plate structures are photo-lithographically defined. The exposed oxide layer is removed in buffered hydrofluoric acid, and the silicon beneath it is reactive-ion-etched to free-release the mirror. Further process details are provided in appendix A.3. Figure 4-16 shows a photograph of a deflected type-3 actuator.

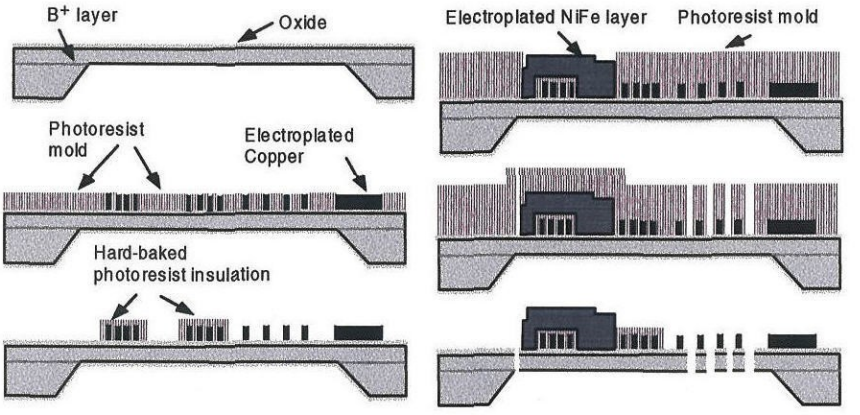

Figure 4-15: Fabrications steps for the type-3 actuator.

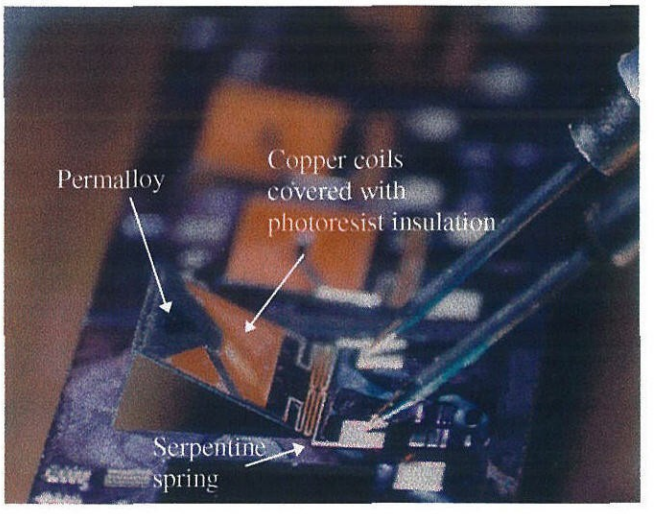

Figure 4-16: Photograph of actuated type-3 actuator.

4.4 Conclusion

The fabrication processes for three types of MEMS electromagnetic actuators have been described, and several processing issues pertaining to their fabrication discussed. From a technological point of view, several new issues also arise from the incorporation of magnetic thin film materials into silicon bulk micromachining. Magnetic forces in microactuators are proportional to the volume of magnetic material. Therefore, micro-actuators generally require thick layers of magnetic material if a large magnetic force is desired. This, however, introduces stress and adhesion problems. Also, care must be taken that the thermal cycling or chemical etching used in the micromachining process does not damage the magnetic materials. Finally, magnetic properties such as remnant magnetization, saturation field, and coercivity of the films may need to be optimized for the specific requirements of the device.

Chapter 5

Actuation Theory and Experiments

Use of the flap actuators in practical applications requires that their operation be fully characterized. Here we have investigated the static and dynamic operation of these actuators in both uniform and non-uniform magnetic fields. For simplicity we first analyzed the actuators' performance in uniform magnetic fields, and only then investigated the actuators in their real operating conditions, non-uniform fields. We also developed theoretical models based on classical electromagnetic theory to describe the actuators' deflections, and when we compare these models to experimental measurements, the two are found to agree well.

5.1 Permalloy actuation

Here we investigate the deflection of the flap actuators with a permalloy actuating layer (type-1 and type-3 actuators), as they respond to external magnetic fields of different strengths. These deflections are caused by forces and torques, which result from the interaction between an external magnetic field and the magnetic moment induced in the permalloy layer. In this thesis we call this kind of actuation permalloy actuation.

Permalloy actuation principle

When a layer of permalloy is placed in a magnetic field it becomes magnetized and develops a magnetic moment **m**. The interaction between the magnetic moment and field then produces a torque which rotates the permalloy so that the moment aligns with the direction of the applied field, as shown in Figure 5-1. In the case of a non-uniform magnetic field, schematically shown in Figure 5-2, in addition to the torque on the permalloy, a translational force proportional to the gradient of the magnetic field is also produced.

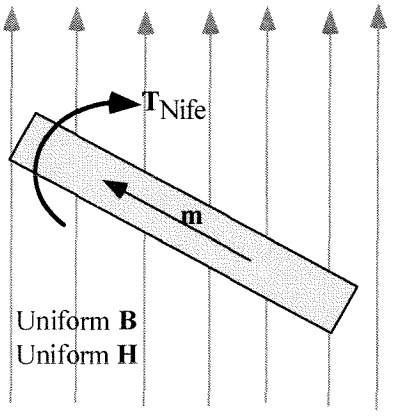

Figure 5-1: Torque acting on permalloy in a uniform field.

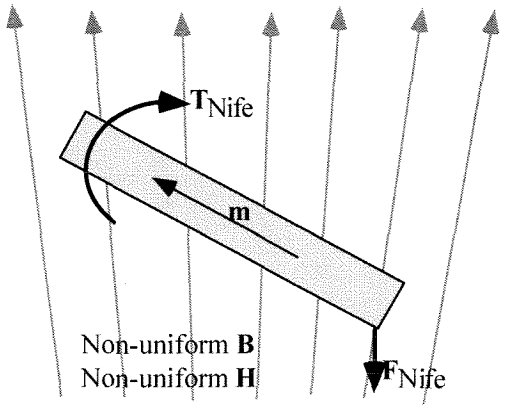

Figure 5-2: Torque and force on permalloy in a non-uniform field.

5.1.1 Static actuation in a uniform magnetic field

Experimental setup

The deflection measurements for the type-1 and type-3 actuators are carried out using the setup shown in Figure 5-3. A CCD camera with a microscope attachment is connected to a TV monitor. A custom built C-shape magnet is used to provide uniform magnetic fields which have magnetic flux variations in the gap of less than 4 gauss. When the actuator is placed in the gap of the electromagnet, and a current applied to the electromagnet, the magnetic field produced causes the actuator to deflect to an angle

proportional to this field. To measure the actuators' deflection angle versus the applied field, the applied field strength is increased incrementally from zero and the corresponding deflection angle of the actuator is measured from the TV monitor. To accurately measure the magnetic fields produced by the electromagnet, a flux sensor is positioned next to the actuator in the gap. Note, it is critical to "initialize" the permalloy before conducting this experiment. What we mean by "initializing" is to apply a field sufficient to saturate the permalloy, and then bring the field to zero. Initialization ensures that the initial magnetization state of the permalloy is known.

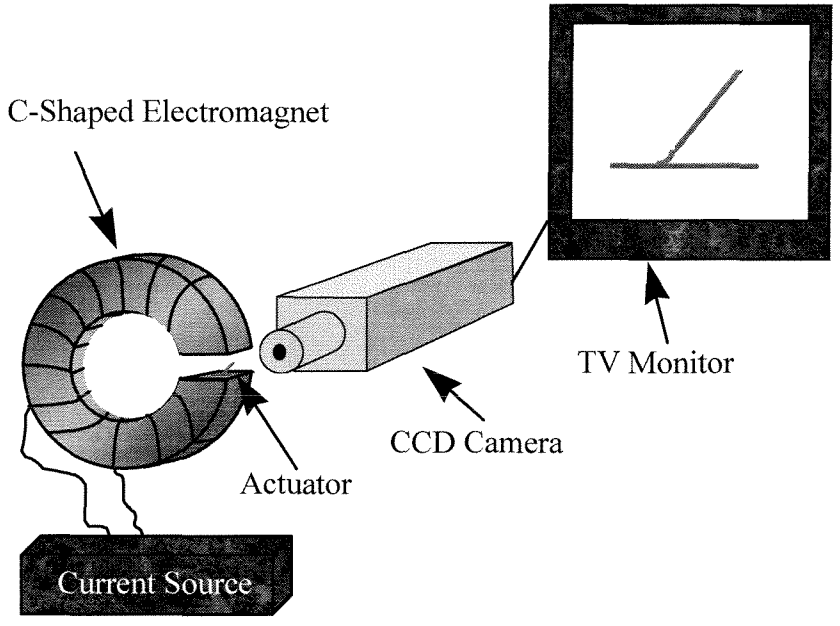

Figure 5-3: Experimental setup used to measure actuator deflections in uniform fields.

To experimentally determine the spring constant of a particular actuator, we have built a load-beam-tester[1]. This device is shown in Figure 5-4. The load-beam-tester consists of a load-cell, which measures gram-forces ranging from -5 g to +5 g at a resolution of 1 mg, and a micrometer connected to a linear voltage displacement transducer (LVDT) which measures the micrometer displacements. To measure an

[1] The author wishes to thank Wen Hsieh for designing and building the load beam tester.

actuator's spring constant, a probe, shown in Figure 5-5, is brought into contact with the actuator's silicon plate. The actuator is mounted on a holder, shown in Figure 5-6, and then the holder is placed on top of the load-cell. The load cell is attached to a micrometer stage so that the actuator's elevation towards the probe can be regulated. The probe pushes on the silicon plate of the actuator exerting a force on the load-cell which is recorded. From the displacement and force measurements, along with knowing the exact position at which the probe is contacting the plate, the spring constant for the actuator can be determined.

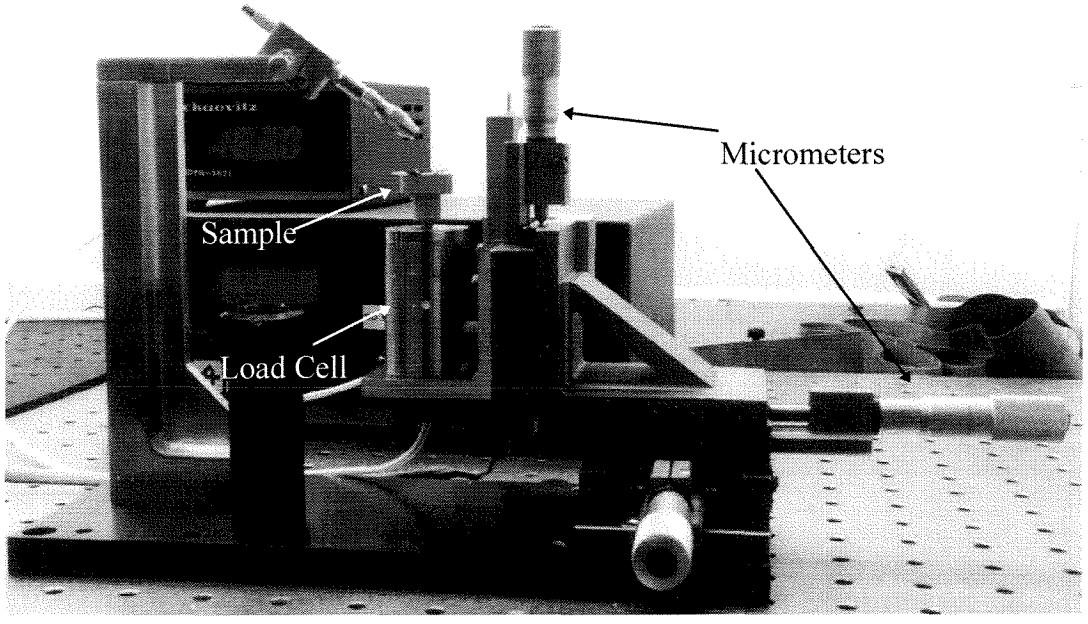

Figure 5-4: Spring constant measurement system - load beam tester.

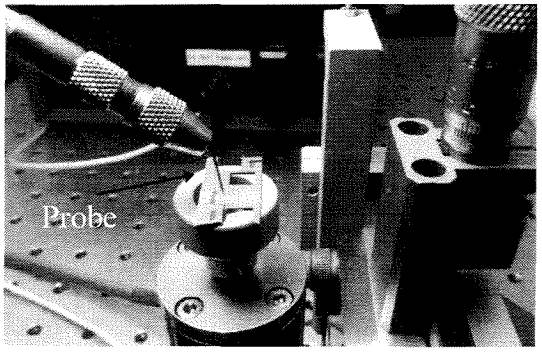

Figure 5-5: Photograph showing probe used to apply force to the actuator.

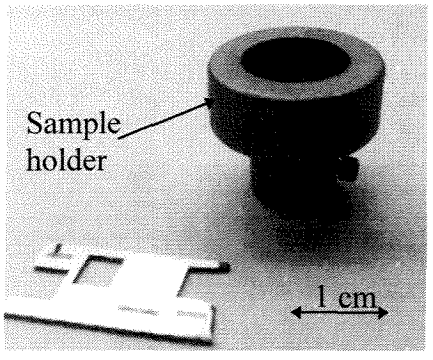

Figure 5-6: Holder used to mount the actuator onto the load-cell.

Measurements and theoretical model

The experimental data is attained by placing the actuator in a C-shaped electromagnet shown in Figure 5-3, and applying a current to the electromagnet. This produces the uniform magnetic field, $\boldsymbol{H}_{ext}$, which is perpendicular to the substrate surface of the actuators. The magnetic field induces an out-of-plane deflection of the actuator plate. Figure 5-7 shows the measured deflection angles for three different types of actuators as a function of the externally applied magnetic field. Note, no current is supplied to the on-board coils of the type-3 actuator during this experiment.

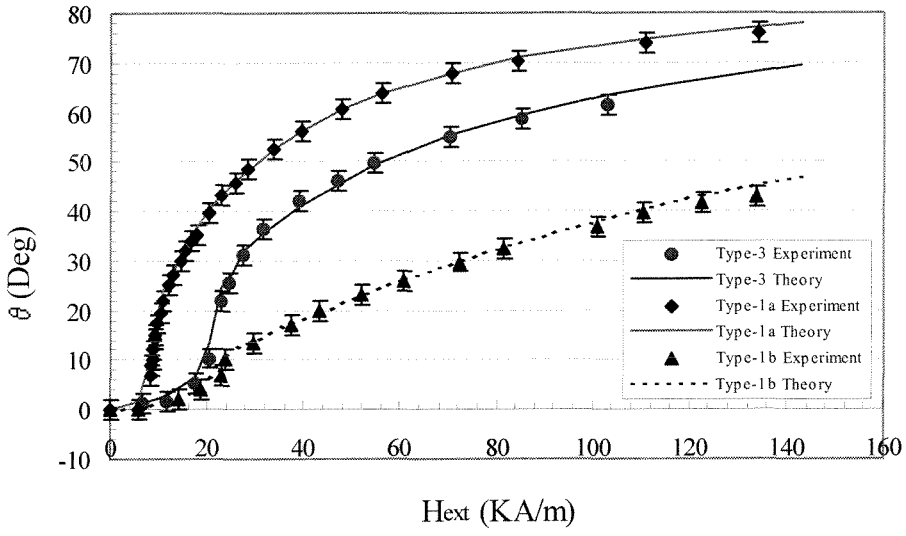

Figure 5-7: Actuator deflection angle versus applied (uniform) magnetic field.

The deflection of each of the three actuator types is modeled using the torque balance principle. Shown in Figure 5-8 are the torques acting on the actuator. T_{NiFe} is the torque caused by the interaction of the magnetic field and the permalloy, and T_{spring} is the restoring torque of the spring. The permalloy torque T_{NiFe} [1,2] for each of the three actuators is produced by the interaction of the external magnetic flux density, $\boldsymbol{B}_{ext}$, with the magnetic moment $\boldsymbol{m}_{NiFe}$ in the permalloy layer of each actuator

$$T_{NiFe} = | \boldsymbol{m}_{NiFe} \times \boldsymbol{B}_{ext} | = V_{NiFe} M_{NiFe} H_{ext} \sin (90 - \theta) \qquad (5.1)$$

where $V_{NiFe} = 2.06\times10^{-10}$ m^3 is the volume of the permalloy for the type-1a actuator, $V_{NiFe} = 6.3\times10^{-11}$ m^3 is the permalloy volume for the type-1b actuator, and $V_{NiFe} = 7.26\times10^{-11}$ m^3 is the volume of permalloy for the type-3 actuator. The external magnetic field, H_{ext}, is given in A/m, θ is the deflection angle of the flap relative to the substrate and M_{NiFe} is the magnetization of the permalloy induced by H_{ext} cos (90° – θ). The permalloy torque (in N-m) is then counterbalanced by the restoring torque of the spring

$$T_{spring} = K\,\theta \qquad (5.2)$$

where the measured torsional spring constant K is equal to 7.67×10^{-8} Nm/deg for the type-1a actuator, $K = 1.1\times10^{-7}$ Nm/deg for the type-1b actuator, and $K = 4.2\times10^{-8}$ Nm/deg for the type-3 actuator, and θ is the deflection angle of the actuators. Equations (5.1) and (5.2) are the governing equations for the operation of the actuators and the theoretical model generated using these equations is shown in Figure 5-7 (solid and dashed lines). Note, that the experimental data is explained well by the theoretical model. The magnetization as a function of applied field, $M_{NiFe}(H_{ext})$, was determined experimentally by B-H loop (Figures 4.8, 4.9, 4.10) and vibrating sample magnetometer (VSM) measurements performed on the permalloy layer of each particular actuator. The B-H loop gives the shape of the $M_{NiFe}(H_{ext})$ curve, while the VSM measurement determines the saturated magnetization (M_s) [5]. The saturation magnetization is 0.96 Tesla for the type-1a actuator, 0.84 Tesla for the type-1b actuator and 0.78 Tesla for the type-3 actuator. Since the thickness of the permalloy layer is much smaller than the length, the demagnetizing effect in plane along the length of the permalloy is neglected.

The theoretical and experimental data of Figure 5-7 for the type-3 actuator is plotted again in Figure 5-12. The dashed curve is a plot of the theoretical model assuming $M_{NiFe} = M_{sat}$ for all values of H. From the value of the field at which this curve and the experimental data diverge, the field required to saturate the permalloy, H_{sat}, can be determined. H_{sat} is simply the component of H_{ext} along the plane defined

by the permalloy film, at the divergence point, so H_{sat} =25472 cos (90° – 30°) = 12.736 KA/m (160 Oe). This value is consistent with the value directly read from the BH-loop (Figure 5-11).

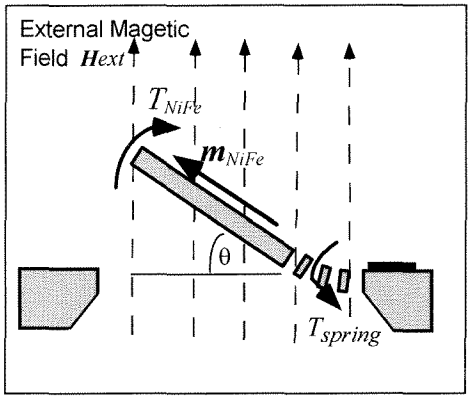

Figure 5-8: Schematic showing torque model.

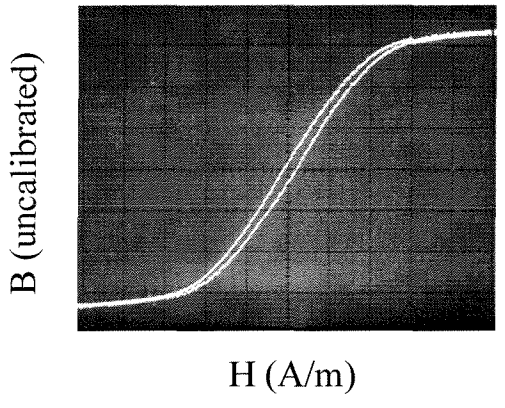

Figure 5-9: BH-loop of type-1a actuator (horizontal axis 1.6 KA/m per div. (20 Oe/div.))

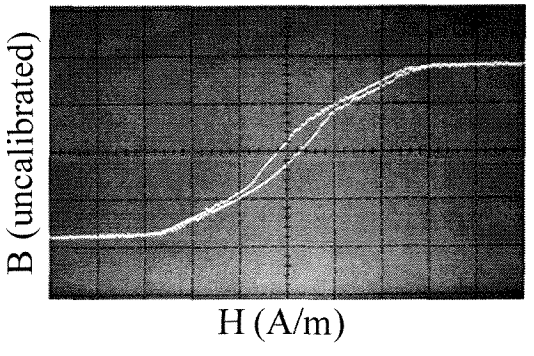

Figure 5-10: BH-loop of type-1b actuator (horizontal axis 1.6 KA/m per div. (20 Oe/div.)).

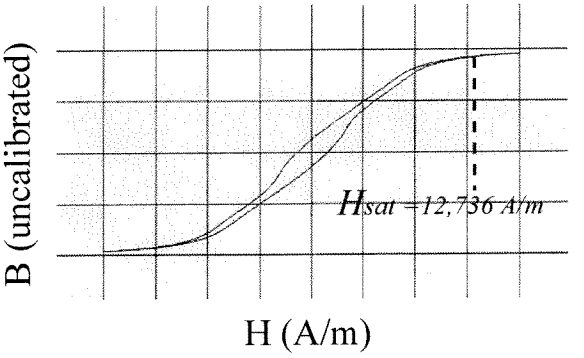

Figure 5-11: BH-loop measurement of type-3 actuator. Horizontal axis 4 KA/m per div. (50 Oe /div.).

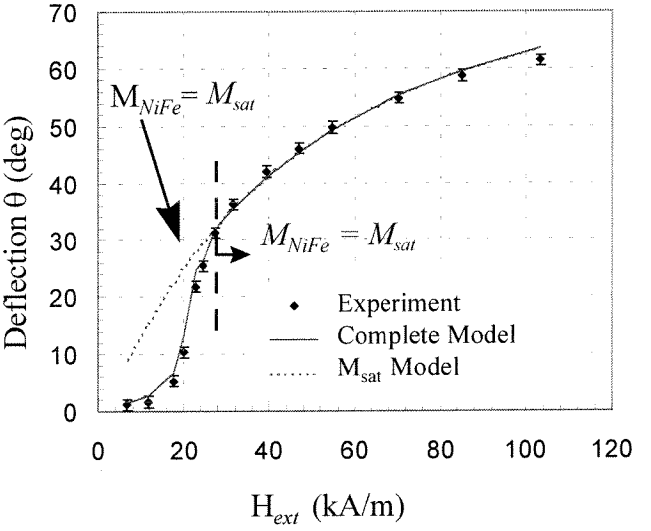

Figure 5-12: Deflection versus applied field for type-3 actuator showing saturated and complete theoretical models.

5.1.2 Static actuation in a non-uniform magnetic field

Experimental setup

In most practical applications, the bulky and inconvenient C-shape electromagnet is not used. Instead, either a small flat electromagnet or a permanent magnet is employed. A flat electromagnet allows a laser beam easy access to the mirror surface of the type-1 actuators while a small permanent magnet can be used to provide a constant bias field for the type-3 actuators which can then be controlled by on-board currents. These flat

magnets, however, produce non-uniform magnetic fields. So the operation of these actuators must be characterized under non-uniform field conditions. This is achieved using the setup shown in Figure 5-13, where the C-shaped magnet of Figure 5-3 is replaced with a flat electromagnet.

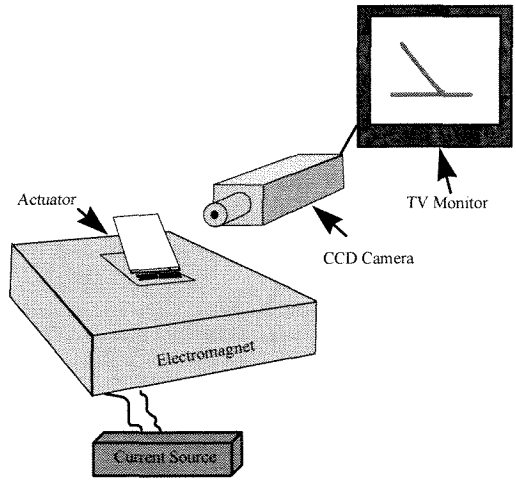

Figure 5-13: Experimental setup for actuators in a non-uniform field.

Electromagnet characterization

Unlike the C-shaped magnet where the magnetic field is easily measured, the magnetic field produced by the flat electromagnet differs for every point in the volume. To reduce the number of measurements, we only characterize the magnetic field at and above a certain region of the electromagnet, where the actuators will be placed. We measured the field at two locations along the Y-axis, at location A and location B which are 3 mm apart, as shown in Figure 5-14. To measure the magnetic field we used a flux meter with a hall effect sensor. First we measured the magnetic fields transverse to the electromagnet, along the Z-axis, and then fields parallel to the electromagnet along the Y-axis. The field along the X-axis is found to be negligibly small.

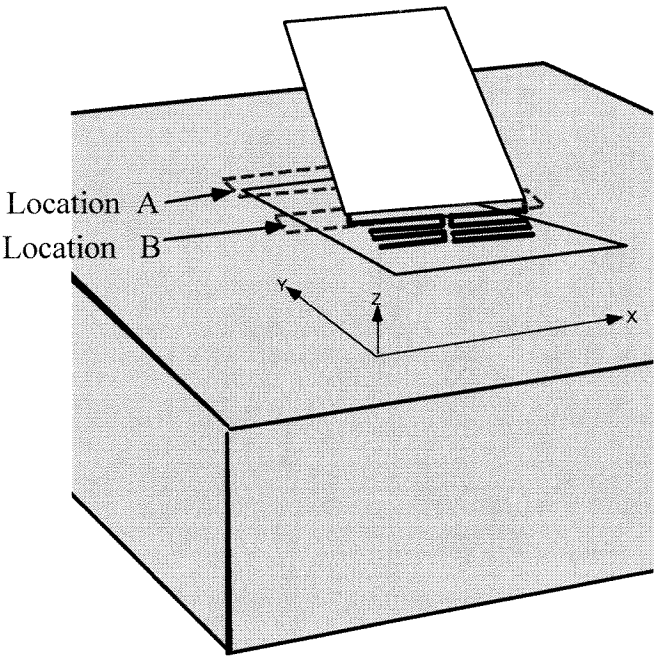

Figure 5-14: Schematic, defining locations A and B on the electromagnet along the Y-axis.

The magnetic field transverse to the electromagnet at location A, as a function of the applied current to the electromagnet, was first measured at a constant height of 1.5 mm above the surface of the electromagnet. In our experiments Z = 1.5 mm is the height between the permalloy layer, on the actuator, and the magnet surface, when no field is applied and the permalloy is lying flat, parallel to the electromagnet. We define this position as h = 0. Figure 5-15 shows that the experimentally measured field strength at h = 0 as a function of applied current. Note the relationship between the current and the magnetic field is linear.

Next the current supplied to the electromagnet is fixed, and the magnetic field is measured as a function of distance from the h = 0 plane. We repeat this for three currents, in this case I = 0.1 A, I = 2.5 A, and I = 5 A, and the results are shown in Figure 5-16. The three curves generated are then fitted, and the magnetic field produced is found to be linearly proportional to the applied currents.

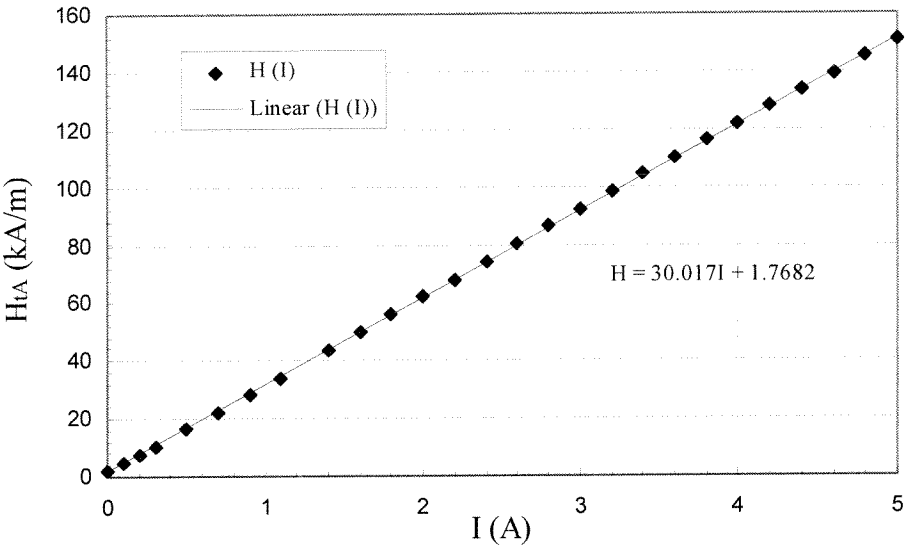

Figure 5-15: Transverse magnetic field, H_{tA}, in the Z+ direction at h = 0, and at location A as a function of applied current to electromagnet.

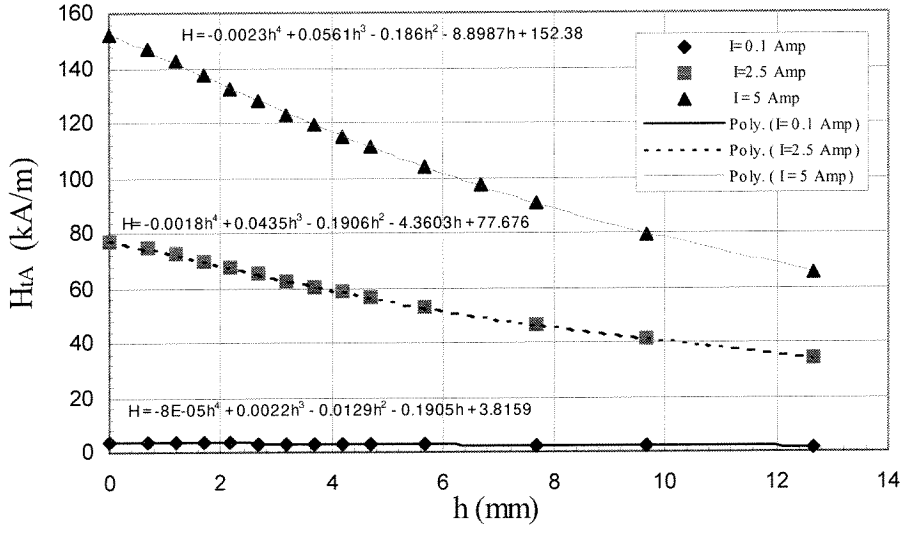

Figure 5-16 : Transverse magnetic field, H_{tA}, in the Z+ direction for different applied electromagnet currents, as a function of height above h = 0, at location A.

We repeat the same measurements as above at location B, and the results are shown in Figures 5-17 and 5-18. Once again the magnetic field is linearly proportional to the applied current.

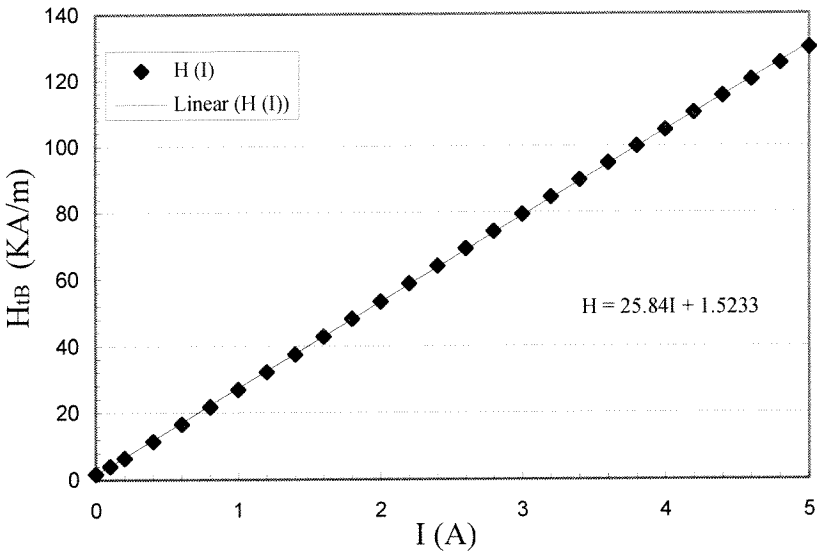

Figure 5-17: Transverse magnetic field, H_{tB}, in the Z+ direction, at h = 0 and at location B, as a function of applied electromagnet current.

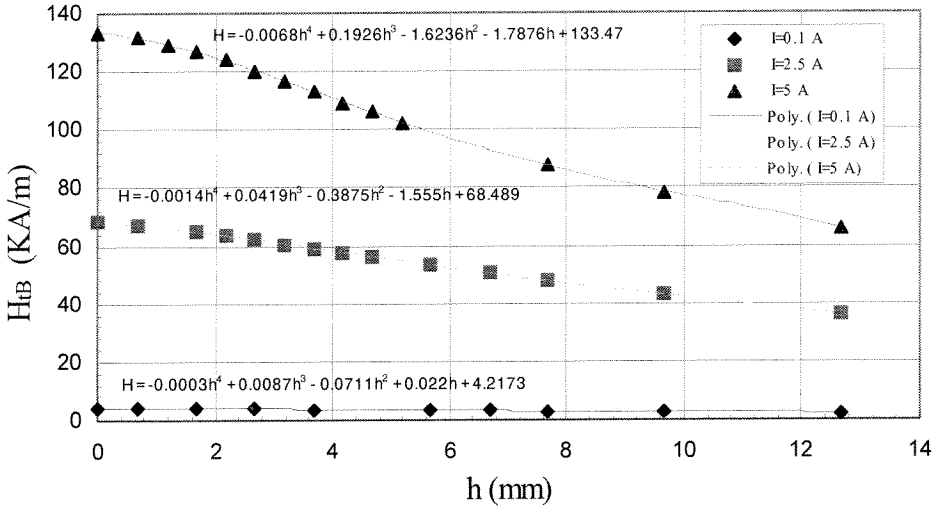

Figure 5-18: Transverse magnetic field, H_{tB}, in the Z+ direction as a function of height above h = 0, at location B on the electromagnet. Measurements were performed for three different currents.

The hall effect sensor is then turned on its side, perpendicular to the magnet, and the magnetic field parallel to the electromagnet, i.e., in the Y-direction, is measured at location A. The sensor is positioned so that its center is located at h = 0, and varying currents are applied to the electromagnet. The result is shown in Figure 5-19. Then the parallel magnetic field as a function of height above h = 0 is measured and plotted in

Figure 5-20. Again, as in the case for the transverse fields, a linear relationship between the applied currents and magnetic fields measured is found; however, the magnitude of the parallel fields is much smaller than the transverse fields.

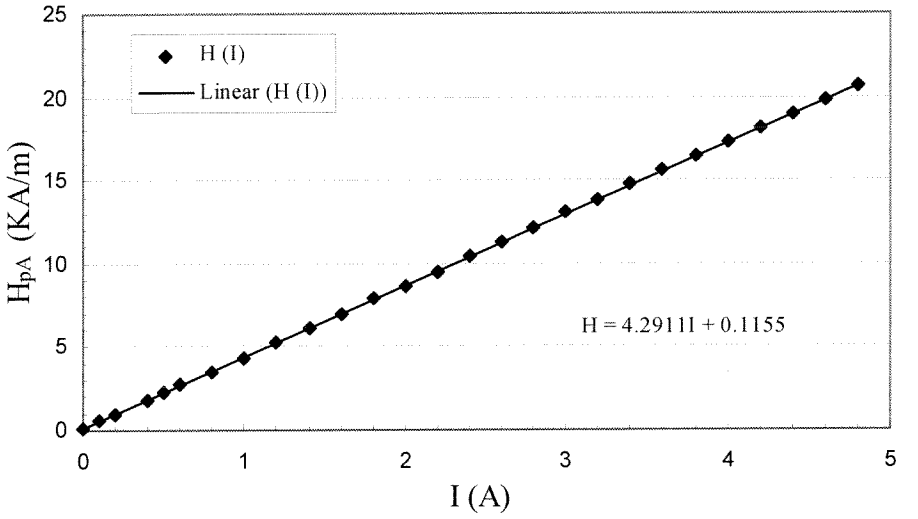

Figure 5-19: Parallel magnetic field, H_{pA}, in the Y+ direction, at h = 0 and at location A, as a function of applied electromagnet current.

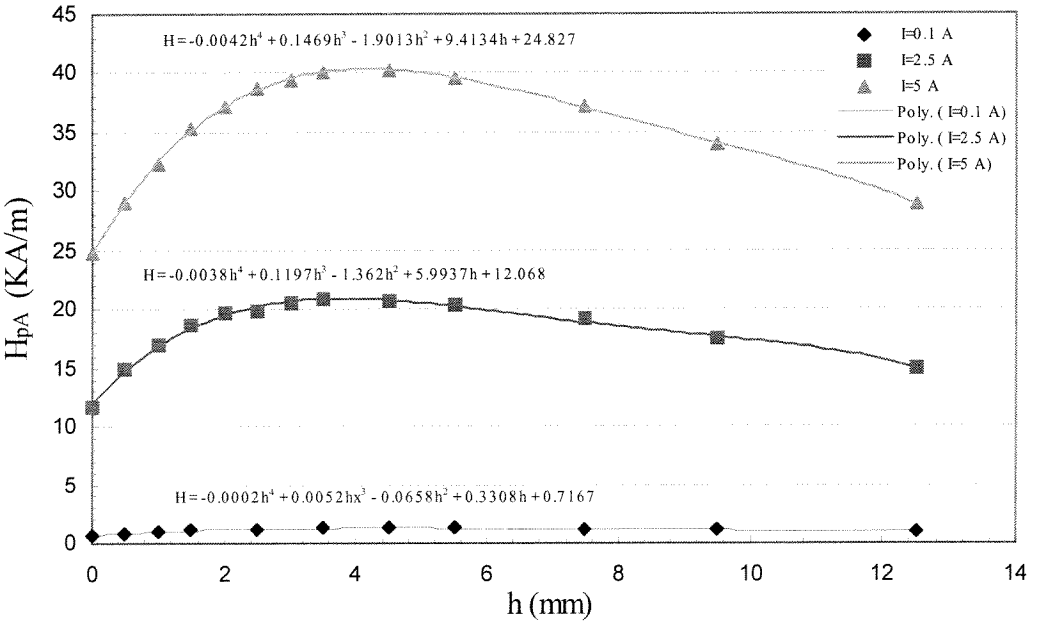

Figure 5-20: Parallel magnetic field, H_{pA}, in the Y+ direction as a function of height above h = 0, at location A, for three different applied currents.

The parallel magnetic field strength, in the Y-direction, is measured this time at location B. The field strengths here are even weaker than at location A. This is expected since in general for magnets, at the center of the magnet the field lines are more vertical. Note, the parallel field lines as a function of height from h = 0 behave in such a manner as to have a clearly defined maximum, as shown in Figure 5-22.

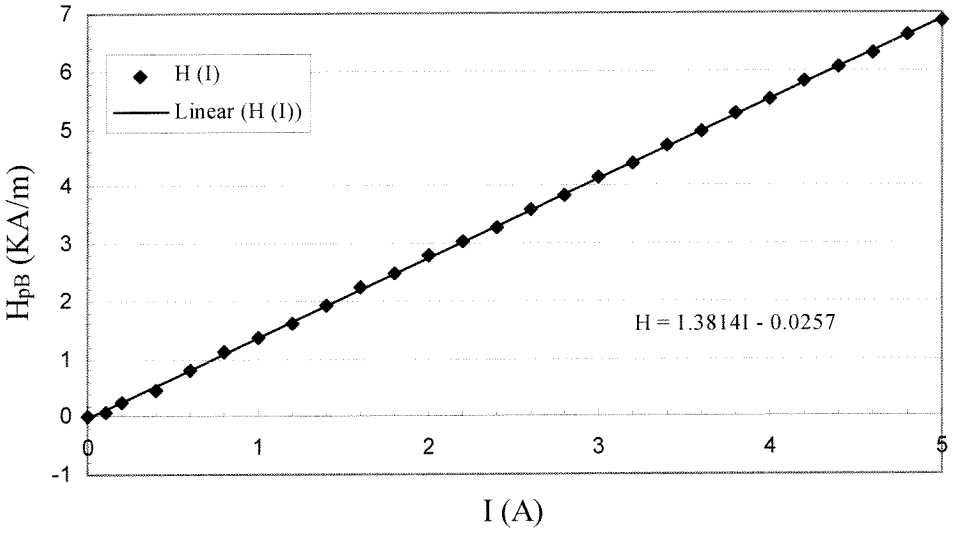

Figure 5-21: Parallel magnetic field, H_{pB}, at h = 0 at location B, as a function of applied electromagnet current, *I*.

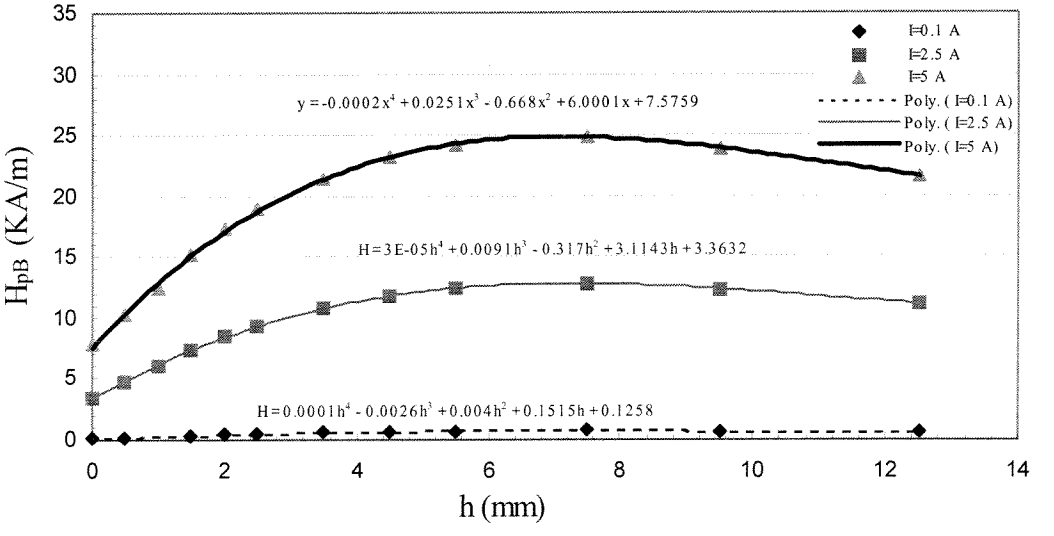

Figure 5-22: Parallel magnetic field, H_{pB}, as a function of height above h = 0, at location B, for three applied currents.

Measurements and theoretical model

In this experiment the deflection angles of the flap versus applied non-uniform magnetic fields are investigated. The non uniformity of the field makes the modeling more complex, but it can be done using the electromagnet characterization performed above. From the above characterization we can generate equations describing the magnetic field at any height above locations A and B for a given applied current.

Here we concentrate on the deflection of the type-1 actuators since the type-3 actuator will behave in an analogous manner. The measured deflections of the type-1a and type-1b actuators in the non-uniform magnetic fields, characterized above, are given in Figure 5-23. From our measurements of the magnetic field as a function of height, we find that the gradient of the field is very small. So when modeling the actuators' deflections, we can assume that the net translational force component is negligible. The actuators' electromagnetically induced deflection is then modeled as being produced by two torques acting on the flap. One torque is due to the transverse magnetic fields and a second torque acting in the opposite direction is due to the parallel magnetic fields, as shown in Figure 5-24.

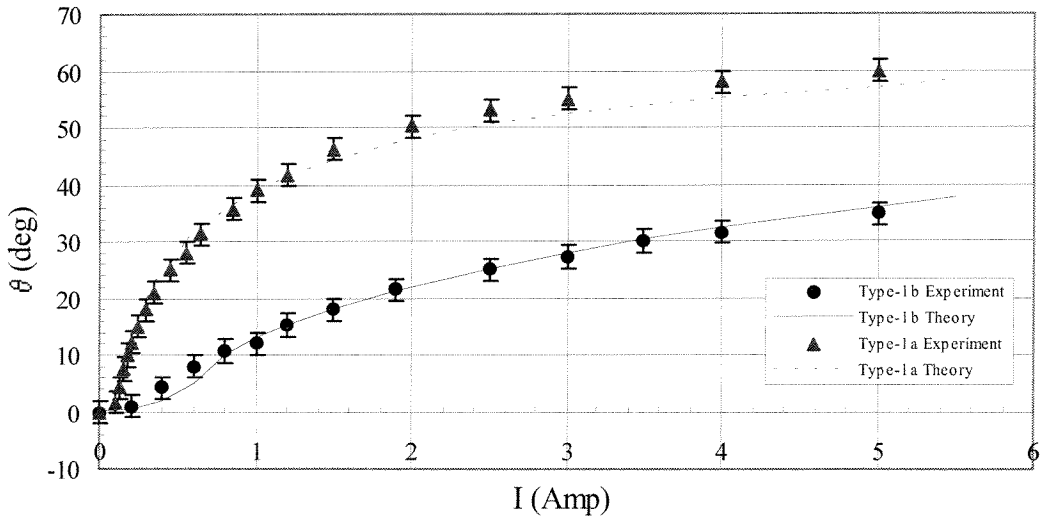

Figure 5-23: Actuator deflection angle versus current supplied to the electromagnet.

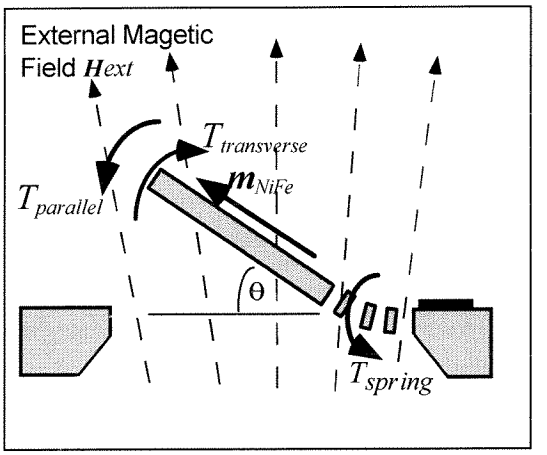

Figure 5-24: Schematic showing actuation concept for actuators in a non-uniform field.

In our model we treat the permalloy as though it were uniformly magnetized with a net magnetization corresponding to the field strength at location B and at height h = 0, producing a magnetic dipole of equal but opposite pole strengths, as shown in Figure 5-25.

First we investigate the behavior of the permalloy in response to the transverse magnetic fields. The poles which are separated by the length of the permalloy (3 mm) experience the forces $F_{tA} = Q\, B_{tA}$ and $F_{tB} = -Q\, B_{tB}$, as shown in Figure 5-25, so the torque can be written as

$$T_{transverse} = (Q\, B_{tA}\, L_a - Q\, B_{tB}\, L_b) \cos\theta \qquad (5.3)$$

where Q is the magnetic pole strength, B_{tA} and B_{tB} are the transverse magnetic flux densities at the location of the permalloy above points A and B on the magnet, L_a and L_b are the lever arm lengths from the pivot point to points a and b respectively, and θ is the angle between the plane and the flap. In chapter 2 we defined the magnetic pole strength as $Q = \frac{MA}{\mu_0}$, where M is the magnetization in Tesla, and A (m^2) is the cross-sectional area of the permalloy layer. Using the relation between the magnetic flux density and the magnetic field in air, $B = \mu_o H$, we can write the above torque expression as

$$T_{transverse} = MA(H_{tA} L_a - H_{tB} L_b) \cos \theta \qquad (5.4)$$

The second torque acting on the permalloy is due to the parallel magnetic field in the Y-direction which produces the forces $F_{pA} = Q B_{pA}$ and $F_{pB} = - Q B_{pB}$. The torque produced by these forces is given as

$$T_{parallel} = (Q B_{pA} L_a - Q B_{pB} L_b) \sin \theta \qquad (5.5)$$

In the same manner the torque as a function of applied magnetic field can be written as

$$T_{Parallel} = MA(H_{pA} L_a - H_{pB} L_b) \sin \theta \qquad (5.6)$$

The total magnetic torque acting on the actuator is the sum of the two torques described above:

$$T_{total} = T_{transverse} - T_{parallel}$$
$$T_{total} = MA(H_{tA} L_a - H_{tB} L_b) \cos \theta - MA(H_{pA} L_a - H_{pB} L_b) \sin \theta \qquad (5.7)$$

Because the permalloy is attached to the silicon plate, which is connected to the bulk silicon by a spring, the torque given in equation (5.7) is countered by a restoring torque due to the springs. We model the torque produced by the springs as linearly proportional to the deflection angle

$$T_{springs} = K \theta \qquad (5.8)$$

This assumption is experimentally verified for deflections of up to 30 degrees, which is the largest deflection angle we can measure using the load-beam-tester. By equating

equations (5.7) and (5.8), we solve for the resultant theoretical deflection angle of the actuator at a given a magnetic field,

$$\theta = \frac{MA}{K}((L_a H_{tA} - L_b H_{tB})\mathrm{Cos}\,\theta - (L_a H_{pA} - L_b H_{pB})\mathrm{Sin}\,\theta) \qquad (5.9)$$

Given in Figures 2-15 through 2-22 are the equations relating the magnetic field strengths at and above locations A and B to the currents applied to the electromagnet. Using these equations in equation (5.9), we obtain a non-linear expression which we can solve for θ, the theoretical deflection angle of the actuator, as a function of the current supplied to the electromagnet. Figure 5-23 shows a plot of the theoretical θ, derived from the above model for both the type-1a and type-1b actuators. The theory shows good agreement with the experimental data for both devices. Note the parameters such as *M*, *Ms* and *K* were defined for these actuators in the previous section. The above model can be further refined by including the translational force and taking into account the fact that the magnetization is not uniform in the permalloy when the permalloy is unsaturated. However, to show that the actuator conforms to conventional electromagnetic theory, the above model is clearly sufficient.

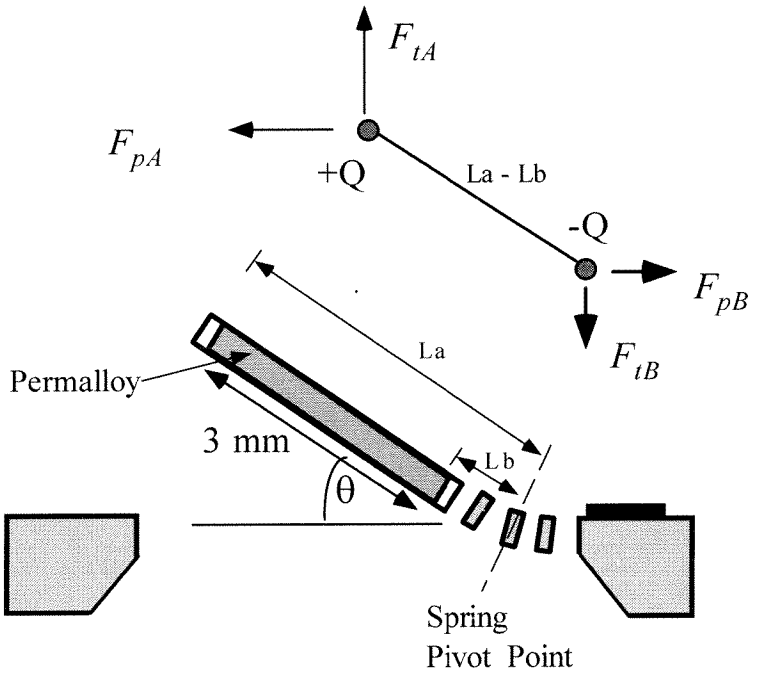

Figure 5-25: Schematic describing the model for the non-uniform magnetic field deflections of the actuators.

5.1.3 Dynamic behavior

The dynamic behavior of the actuators with permalloy are investigated in a magnetic field which is spatially uniform by varies with time. The setup of Figure 5-3 is used, but now the C-shaped electromagnet is driven with an ac current superimposed on a dc bias current. The driving frequency, f_d, of the ac current is varied and the deflection envelope of the actuators is measured. A strobe light assists in the measurement of the deflection envelope. We investigated the type-1 actuators and, in particular the type-1a actuators, since they are representative of the large deflection dynamic behavior of the permalloy actuators. The resonant frequencies for the type-1a and type-1b actuators range from90 - 110 Hz, depending on the exact stiffness of the springs. The observed quality factor for these actuators is low, typically less than 50. Figure 5-26 shows a frequency response plot measured for a type-1a actuator. The angular envelope about a dc deflection of approximately 50 degrees is plotted as a

function of driving frequency. The dc bias field is 27.5 KA/m (345 oe) while the ac field is ± 4.4 KA/m (±55 oe).

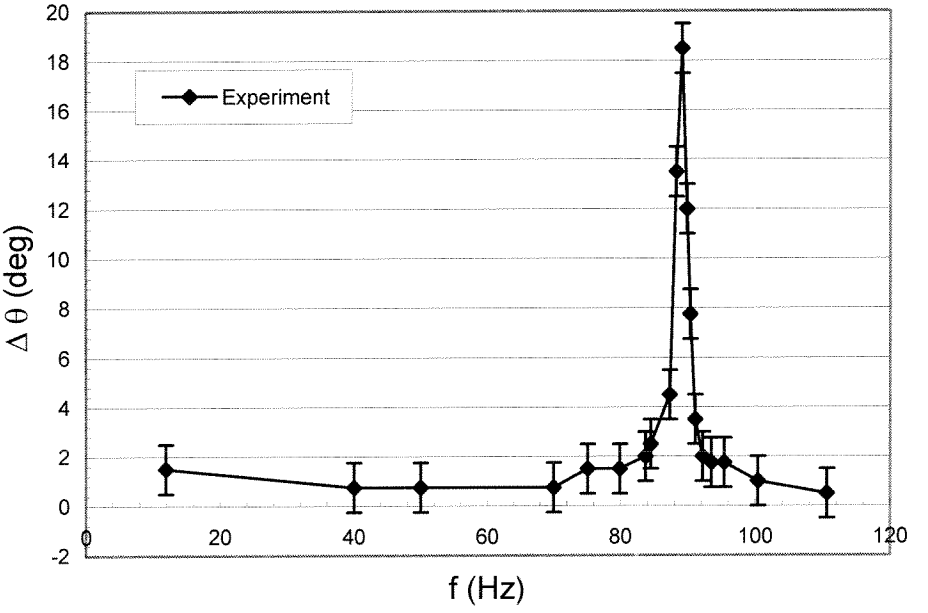

Figure 5-26: Frequency response of type-1a actuator in a spatially uniform but time varying magnetic field.

5.2 Coil actuation

Up to this point we have explored the deflection of actuators due to the interaction of the permalloy layer with a varying external magnetic field. Now let's consider the deflection of actuators in a fixed external magnetic field, produced by applying currents to their on-board coils.

Coil actuation is due to the interaction between an external magnetic field and an effective magnetic moment produced by current flowing in the electrical coils of the actuator. Both the type-2 and type-3 actuators take advantage of this actuation mechanism. For the type-3 actuators which combine both a permalloy layer and copper coils, a constant external magnetic field will first cause the permalloy flap to

deflect to a fixed "bias" angle due to the permalloy-actuation produced by a fixed external magnetic field. Then by changing the magnitude and direction of the current supplied to the on-board coils, variable deflections about this "bias" angle can be produced. Deflections for the type-2 actuators, which don't have a permalloy layer, are produced only by passing current through the on-board coils.

5.2.1 Static actuation in a uniform magnetic field

Measurements and theoretical model

The operation of the type-3 actuator with currents applied to its on-board coils is explored. Figure 5-27 shows the coil-actuated deflection angle of the actuator in a uniform external bias field fixed at 79 kA/m (994 Oe). Without the coil current this magnetic field saturates the magnetic moment in the permalloy and causes a bias angle of $\theta = 58\ °$.

To model the coil actuation, we add two more terms to the torque balance described in section 5.1.1 and shown in Figure 5-8. A schematic of the torques acting on the actuator is shown in Figure 5-28. The T_{coil} term is the torque induced by a current moment, $\boldsymbol{m}_{coil} = I A_{total}$, in a magnetic field, and is given as

$$T_{coil} = |\boldsymbol{m}_{coil} \times \boldsymbol{B}_{ext}| = m_{coil} B_{ext} \sin\theta \qquad (5.10)$$

where I is the current supplied to the coils in amperes, A_{total}=0.000132 m^2 is the sum of 30-turn areas, and $B_{ext} = \mu_o H_{ext}$ is the magnetic flux density in Tesla. The thermal torque is induced by heat generated by this current flowing in the coils, and it is modeled as

$$T_{thermal} = -C I^2 \qquad (5.11)$$

In this case $C = 25.2\text{x}10^{-6}$ Nm/A^2 is a fitting parameter, and I is the applied coil current in amperes. The negative sign in equation (5.11) means that the thermal torque always bends the actuator plate down. As a result, when a current is applied to the coils with a constant external magnetic field, the torque balance equation becomes

$$V_{NiFe} M_s H_{ext} \cos\theta + m_{coil} B_{ext} \sin\theta - C I^2 = K\theta \qquad (5.12)$$

Figure 5-27 shows both the experimental and theoretical data for the type-3 actuator controlled by the coil actuation. A good agreement between experimental data and the theoretical model is obtained. Note that Figure 5-27 also shows that the coil actuation can produce a ± 10° deflection about the bias angle, which allows for fine control of deflections required in scanning mirror applications.

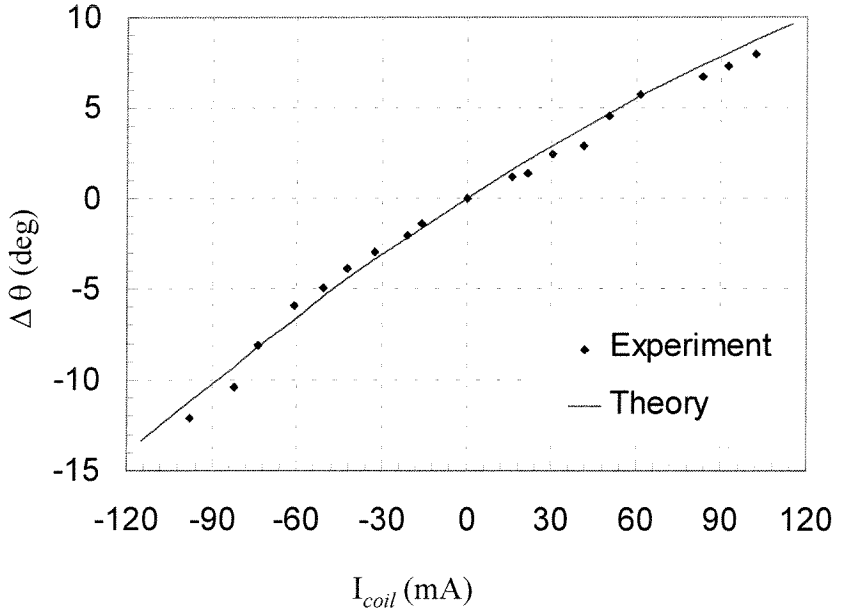

Figure 5-27: Change in deflection angle from "bias" position at variable coil current, with external field of 79 KA/m (994 Oe).

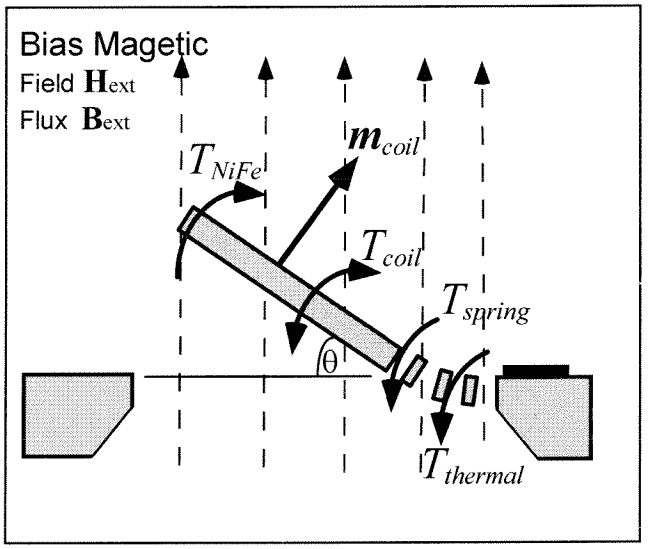

Figure 5-28: Schematic showing torque balance of the actuator with both the permalloy and coil current in an external magnetic field.

5.2.2 Static actuation in a non-uniform magnetic field

Experimental setup

The type-2 actuators are designed for small deflections, less than 5 degrees, so a more accurate measurement setup is needed to determine their deflections. The experimental setup used to measure these deflections is shown in Figure 5-29. It consists of a microscope, with a built in micrometer which has a very short focal depth, a current source, and a rare-earth magnet onto which the actuators are placed. To measure the actuator displacements, we first focus on a particular location on the actuator flap, when no current is supplied to the actuator. Then we apply a current to the on-board coils and adjust the microscope focus by changing the microscope's

height above the flap; this change is registered on a micrometer and directly corresponds to the actuator's displacement. In this manner the deflection of the actuator as a function of applied current can be determined at particular locations of the flap.

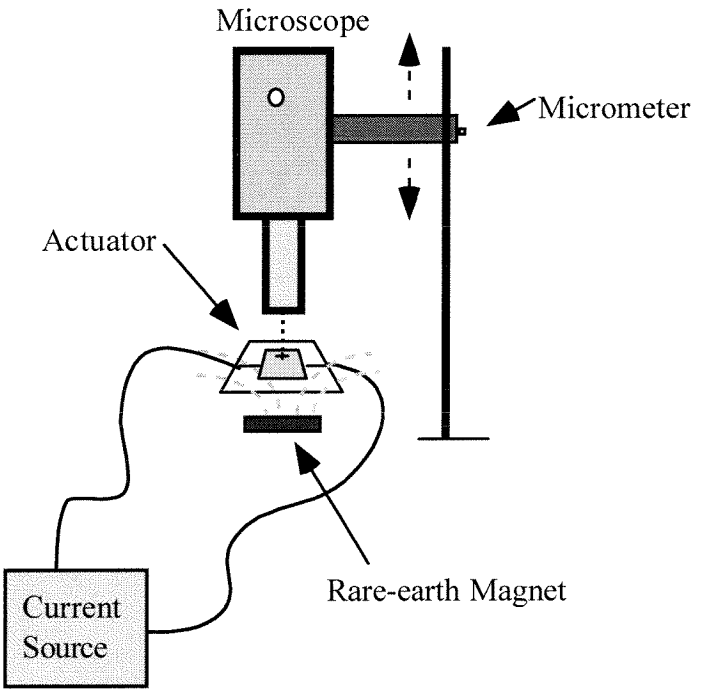

Figure 5-29: Schematic of experimental setup used to measure deflection of the type-2 actuators.

To model the deflection of these actuators, the magnetic flux density produced by the rare-earth magnet must also be characterized. In this case we only measure the magnetic flux density as a function of height above the center of the rare-earth magnet. We call this location D. Figure 5-30 shows the measured magnetic flux density as a

function of height above the rare-earth magnet, at location D. An equation describing the magnetic flux density as a function of height is found by fitting the data.

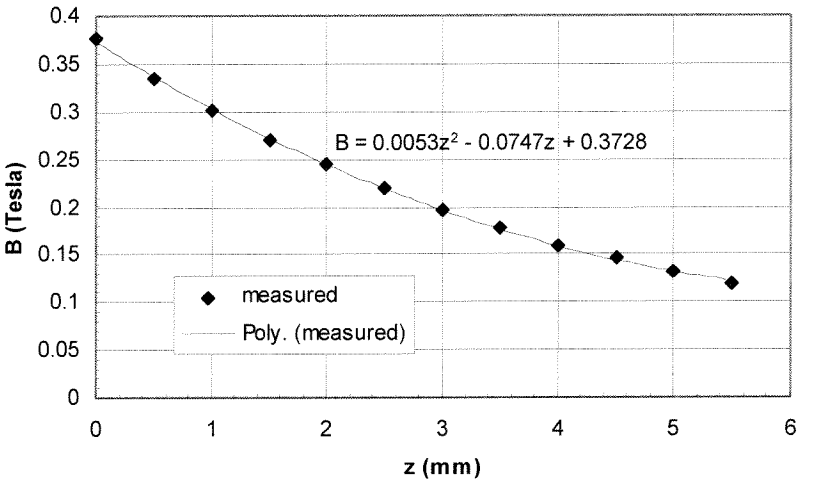

Figure 5-30: The magnetic field at location D on the rare-earth magnet measured as a function of height above the magnet. Note in our experiments location D corresponds to the center of the coils of the type-2 actuators.

Measurements and theoretical model

The non-uniform magnetic field behavior of the type-2 actuators is investigated. When conducting the actuator displacement measurements, each actuator is aligned to the rare-earth magnet so that the center of the on-board coils is 2 mm above the magnet's surface at location D. Note, when we investigate the type-2b actuator, we apply current to only one set of coils, so that we can compare its performance with that of the type-2a actuators. In general, if both sets of coils have currents applied, two locations of the rare-earth magnet must be characterized in order to be able to model the deflections of the type-2b actuators under these conditions.

A definition of the locations on the actuators at which the deflection measurements were performed is given in Figure 5-31, and the experimentally determined deflections of the type-2a and type-2b actuators versus applied current are shown in Figure 5-32.

Large deflections for the type-2a actuators, ranging from 200 and 300 μm, are achieved at a current of approximately 30 mA. The deflection of the type-2b actuator is smaller, only approximately 100 μm; however, this measurement is performed with only one coil operational and can be doubled if the second coil is also working.

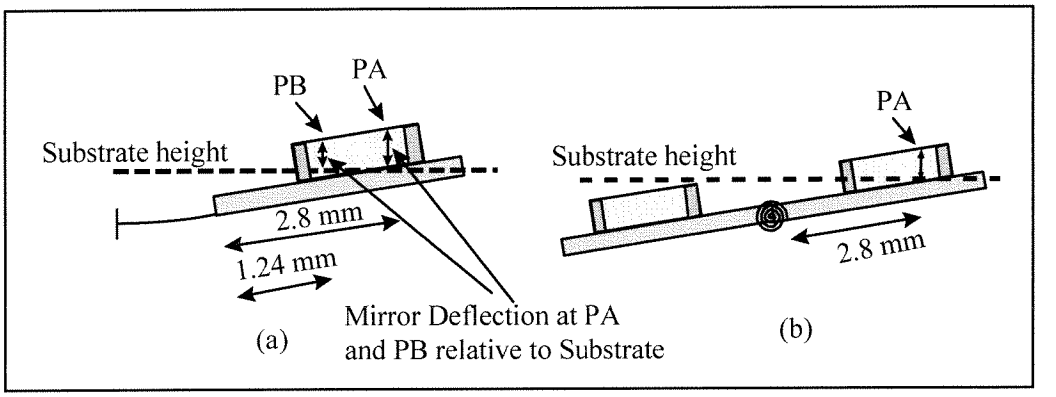

Figure 5-31: (a) Switch deflection measurement locations defined for cantilever, type-2a, switch (b) for torsional, type-2b, switch.

The electromagnetic actuation for the type-2 actuators is modeled as being produced by the interaction between the on-board coil currents and the magnetic flux density gradient, as discussed in chapter 2. In this section we first concentrate on modeling the deflection of the type-2a actuator, and later we will discuss the simpler model for the type-2b actuator. The deflection of the type-2a actuator is the result of several forces acting on the plate as shown in Figure 5-33a. The first force is the electromagnetic force acting on the type-2a actuator. It is assumed to be acting at the center of the silicon plate, which corresponds to the center of the copper coils. This force is modeled by

$$F_{coils} = m\frac{dB}{dz} = I_c A \frac{dB}{dz} \qquad (5.13)$$

where m is the magnetic moment produced by the coils and is equal to the current in the coils times the sum of the areas enclosed by the coils, $m = I_c A$, and $A = 3.36 \times 10^{-4}$ m^2, $\frac{dB}{dz} = 86.7$ Tesla/m at z = 2 mm which is the height of the coils above the magnet. A second force acting on the silicon plate is the force of gravity which is given as

$$F_{gravity} = g(\rho_{si} V_{si} + \rho_{cu} V_{cu}) \qquad (5.14)$$

where ρ_{si} and ρ_{cu} are the density of silicon and copper respectively, V_{si} is the volume of the silicon plate and the mirror mounted on top, and V_{cu} is the volume of the copper coils. For better accuracy we experimentally measure the actual weight of the flap rather than estimate it theoretically. The force due to gravity, acting on the silicon plate, is found to be

$$F_{gravity} = 49\ \mu\text{N} \qquad (5.15)$$

The silicon plate is assumed rigid, and the gravitational force and the coil force are assumed acting at the center of the plate as shown in Figure 5-33.

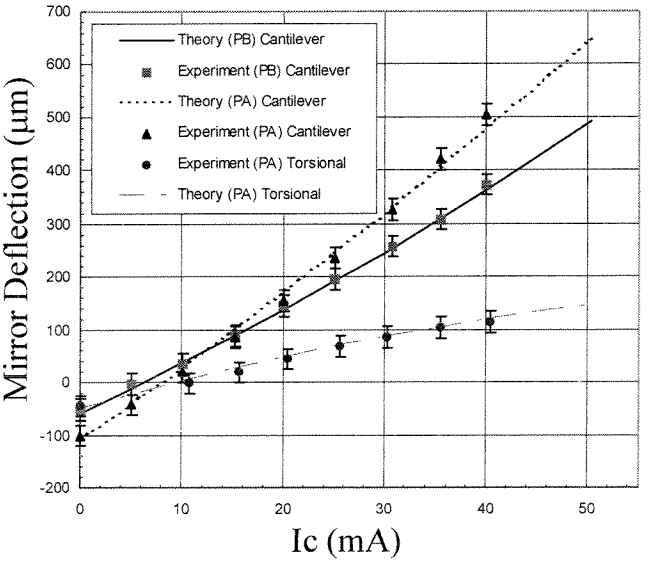

Figure 5-32: Experimental data and theoretical models of the type-2a and type-2b actuator deflections at locations PA and PB.

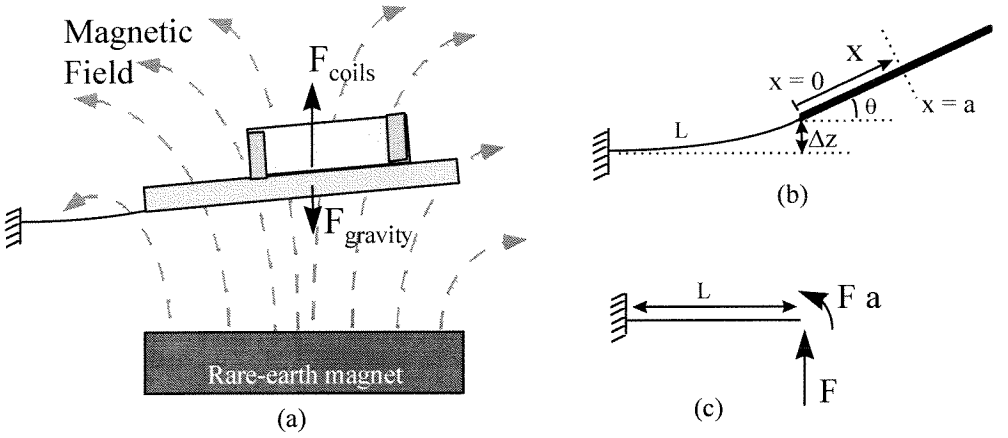

Figure 5-33: (a) Schematic showing forces acting on type-2a actuator. (b) Definition of deflection parameters. (c) Mechanical representation which is used to model deflections of actuator. F is the sum of all the forces acting on the actuator, and the torque is the force times the distance from the tip of the beams to the location at which these forces act.

The silicon plate is attached to the bulk silicon by four cantilever beams, and the magnetic and gravitational forces acting on the actuator cause the cantilever beams to bend. The deflection of the actuator plate at the point where it is attached to the beams, $X = 0$ as shown in Figure 5-33b, is given by the following expression:

$$\Delta z = \left(\frac{L^3}{3EI} + \frac{aL^2}{2EI}\right)\left(F_{coils} - F_{gravity}\right) \qquad (5.16)$$

where a is the distance from the tip of the beams to the center of the silicon plate, L is the length of the beam, E is Young's modulus for silicon, and I is the moment of inertia of the four combined beams, and Δz is the deflection at the tip of the beams as shown in Figures 5-33b and 5-33c. Equation (5.16) utilizes the small deflection model for cantilever beams, which assumes that the deflections are linearly proportional to the applied forces. We validate the use of this model by experimentally finding that the spring constant in the range of operation is linear. Figure 5-34 shows the experimental measurements of force versus displacement for the type-2a actuator measured using the load beam deflector; as can be clearly seen the dependence is linear in the range of

operation. An expression for the slope at the tip of the beams as a function of the forces acting on the actuator plate is calculated as

$$\theta = \left(\frac{L^2}{2EI} + \frac{aL}{EI}\right)(F_{coils} - F_{gravity}) \qquad (5.17)$$

Because the silicon plate is rigid, the slope at the tip of the beams is also the slope of the plate. Using equations (5.16) and (5.17), we can then find a theoretical expression for the displacement at any location on the silicon plate; we have chosen locations PA and PB.

We find that the above model is not quite complete since the flowing current heats the conductors and produces a thermally induced deflection as a result of thermal mismatch between expansion coefficients of the copper and silicon. To determine the thermally produced deflections, we measure the deflection of the actuators at locations PA and PB as a function of the applied current in the absence of a magnetic field. We found that this deflection is proportional to $C\, I_c^2$ where C is a device constant. At PA C = 0.067 m/Amp^2 while at PB C= 0.038 m/Amp^2. This thermally induced deflection is negligibly small for currents below 35 mA; however, it rapidly becomes more significant as the currents are further increased. By using equations (5.16) and (5.17) and adding the thermally induced deflection term, theoretical expressions for the displacement of the actuator at locations PA and PB can be found. These expressions are plotted in Figure 5-32 and show good agreement (better than 5%) with the experimentally measured data. Note, the displacements are plotted relative to the silicon substrate height as illustrated in Figure 5-31.

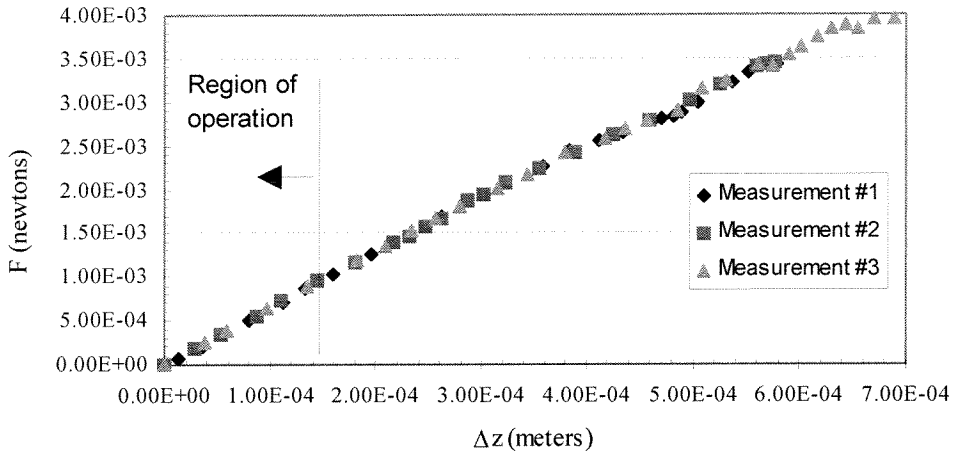

Figure 5-34: Experimental measurement, repeated three times at tip of cantilever beams, showing the deflection at the tip of the beams versus applied force. The deflections are linear with force, in the region of actuator operation.

The model for the type-2b actuator actuated by using only one coil is simpler than the type-2a actuator since the spring is a torsional beam. The electromagnetic force is given by the same expression as above,

$$F_{coils} = m\frac{dB}{dz} = I_c A \frac{dB}{dz}, \tag{5.18}$$

but now $A = 3.29 \times 10^{-4}$ m^2 is the area enclosed by the 70 turn coil. The torque acting on the flap due to the current in the coils is approximately the force time the lever arm, a, which is the distance from the torsional beam to the center of the coils. Since the deflection angle of the flap is so small, the torque can be written as

$$T_c = F_{coils}\, a = I_c A\, a \frac{dB}{dz} \tag{5.19}$$

The torque terms due to gravity on each side of the plate cancel each other out, and the coil torque is balanced by a restoring torque, T_s, from the spring, which is found experimentally to be linearly proportional to the deflection angle of the actuator for the range of angles at which the actuator is used.

$$T_s = K\,\theta \qquad (5.20)$$

where K is the torsional spring constant and it is measured to be 4.9×10^{-7} Nm/deg. Once again it is found that the current produces a deflection due to heating. As in the case for the cantilever actuators, the deflection can be approximated as being proportional to the current squared; C = 0.032 m/Amp^2 is the proportionality constant at PA. The theoretical model based on equations (5.19) and (5.20) and the thermal deflection taken into account is shown in Figure 5-32. Again it agrees well with the experimental data.

5.2.3 Dynamic actuation

In this section we consider the dynamic behavior of the actuators when they are driven with only on-board ac currents. As an example we present the operation of the type-3 actuators.

The experimental setup to measure the frequency response requires the use of a laser-vibrometer-system. This system consists of an HP3563A control system analyzer, and a 55X laser vibrometer. We connect both the type-3 actuator and the laser vibrometer to the HP3563A instrument. The control system analyzer provides the driving currents required to excite the actuator and measures the output signal corresponding to the amplitude of deflection of the actuator measured using the laser vibrometer. Note, the experiment is conducted in a non-uniform field, but one which is sufficiently large to fully saturate the permalloy; also the actuator is configured so that the bottom silicon plate of the actuator is facing up and the magnet is positioned beneath the actuator. The small signal frequency response of the type-3 actuator is measured and is shown in Figure 5-35. The permanent magnet provides a constant magnetic flux density of B = 0.13 Tesla at the permalloy. This causes the flap to deflect towards the magnet about 15 ° because of the permalloy layer.

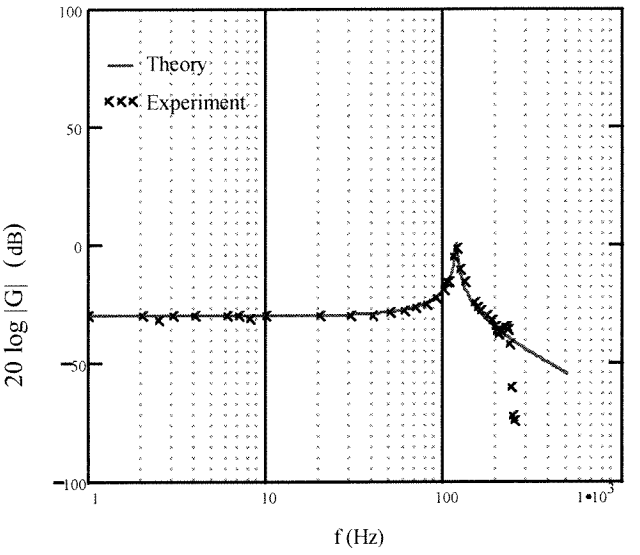

Figure 5-35: Frequency response plot for the type-3 actuator.

The dynamic deflection of the actuator can be modeled by

$$J\ddot{\theta} + \beta\dot{\theta} + K\theta = I_c AB\sin\theta + M_S B\cos\theta \qquad (5.21)$$

where $J = 7.85\text{x}10^{-12}$ kgm^2 is the calculated angular moment of inertia, $K = 2.5\text{x}10^{-7}$ Nm/deg is the measured torsional spring constant, β is the damping coefficient, I_c is the current supplied to the coils, A is the sum of the calculated areas enclosed by each of the coil turns, and M_s is the saturation magnetization of the permalloy. Since we are considering the small angle deflections of the actuators, we can define θ as

$$\theta = \phi_O + \phi(t) \qquad (5.22)$$

In this case ϕ_o is the bias angle produced by the permalloy magnetic field interaction and is equal to 15 °. $\phi(t)$ is the time varying angle change caused by the current. Substituting equation (5.22) into equation (5.21), we obtain a differential equation for the time dependent angle

$$\ddot{\phi} + \gamma\dot{\phi} + \frac{K}{J}\phi = \frac{I_c AB\sin\phi_o}{J} \qquad (5.23)$$

where $\gamma = \beta/J$ is the damping coefficient. Note, since $\phi(t) << \phi_o$ we can approximate $\sin\theta \approx \sin\phi_o$. By taking the Laplace transform of equation (5.23), we obtain an expression for the theoretical frequency response,

$$G(s) = \frac{\phi(s)}{I_c(s)} = \frac{AB\sin\phi_o}{J(s^2 + \gamma s + \frac{K}{J})} \tag{5.24}$$

which is plotted in Figure 5-35. The resonant frequency is found to be 118 Hz, and the quality factor Q = 35.

REFERENCES

[1] J. W. Judy and R. S. Muller, "Magnetic Microactaution of Torsional Polysilicon Structures," *Proceedings, 8th International Conference on Solid-State Sensors and Actuators*, Stockholm, Sweden, Vol. 1, pp. 332 - 335, 1995.

[2] C. Liu, T. Tsao, Y.C. Tai, J. Leu, et al., "Out-Of Plane Permalloy Magnetic Actuators for Delta-Wing Control," *Proceedings, IEEE Micro Electro Mechanical Systems Meeting, MEMS'95*, pp. 328-331, 1995.

Chapter 6

Applications

Two applications for the electromagnetic flap actuators which were described in chapter 5 are demonstrated in this chapter. In one application the actuators are used as laser beam scanning mirrors for holographic data storage, and in the other they are used as fiber optic bypass switches. For both of these applications electromagnetic actuation provides an elegant way to achieve large deflections. However, the electromagnetic technology developed for the flap actuators is not restricted to the fabrication of these actuators alone, but can also be used for many additional applications, such as actuators for disk-drive head positioning, micro-relays, switches, and on-chip micro-inductors and transformers.

6.1 MEMS scanning mirrors for holographic data storage

6.1.1 Principle of holographic data storage

Volume holographic data storage is a very promising technology. In a volume roughly that of a compact disk, it offers the potential of large data storage capacity, approaching one terabyte, with a bit rate as high as a billion bits per second, and a random access time of less than 100 μs [1].

Volume holographic data storage is achieved by using two laser beams, one reference beam and one signal beam, which interfere with each other and form a 3-D interference pattern in a light-sensitive crystal; this procedure is illustrated in Figure 6-1. An example of a crystal that can be used is Fe-doped $LiNbO_3$. The interference pattern changes the optical properties of the crystal and produce a 3-D refraction grating, called a hologram, which is then stored by the crystal. Writing the information to the crystal requires both the reference and image beams, but when reading only the reference beam is needed. The reference beam is shone through the crystal and the pre-stored 3-D grating inside the crystal reproduces the image beam, which can then be read by a CCD camera.

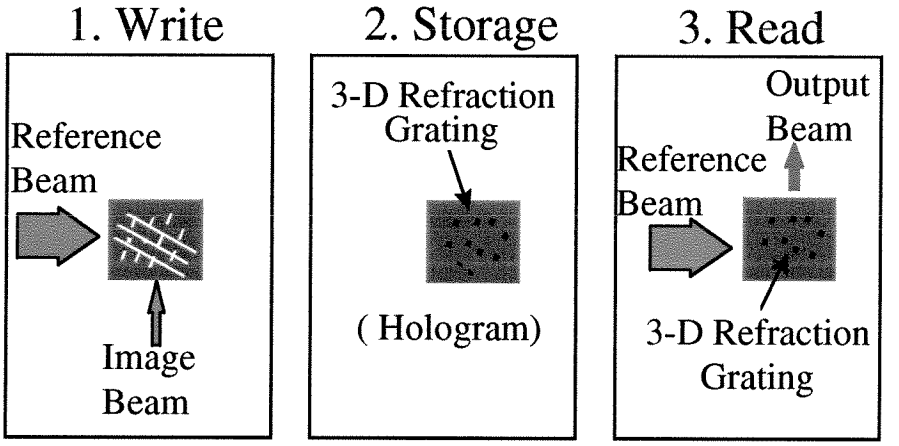

Figure 6-1: Major steps to achieve holographic data storage.

Many multiplexing methods, such as angular, spatial, and wavelength multiplexing, can be used to store a high density of 3-D gratings, in a limited crystal volume. Angular multiplexing is the most common and successful technique allowing up to 10,000 holograms to be stored at a single location in a 1 cm^3 crystal [2]. For each hologram stored, a unique reference laser beam incident angle θ_R, is used. Changing the angle of the reference laser beam produces a new interference pattern that corresponds to a new grating, stored in the crystal. To ensure that two holograms do not interfere with one another, the difference in angles used to store neighboring holograms must be

sufficiently large. The angular selectivity determines the minimum angular difference that can be used. The intensity of the output beam produced when we shine the reference beam through a particular hologram depends on how closely the angle matches the original angle with which the hologram was stored. If the angle of the reference beam matches the original angle exactly, the power of the output beam is maximum; if the reference beam angle is slightly offset, the output beam will still be reproduced but its intensity will be lower. This intensity as a function of angle about the original angle of the reference beam has the form of a sinc function as shown in Figure 6-2. The angular spacing between the central peak and the first null of the function is referred to as the angular selectivity and is given by the following expression,

$$\Delta\theta = \frac{\lambda}{L}\frac{\cos\theta_S}{\sin(\theta_R + \theta_S)}, \tag{6.1}$$

where θ_S and θ_R are the incidence angles of the image and reference beams respectively, L is the smaller of either the thickness of the crystal or the width of the reference beam, and λ is the wavelength of the laser beam. In holographic data storage we want the angular selectivity to be small, so that we can maximize the number of holograms within a given angular range. In theory the next hologram can be stored at the first null location; however, in practice to minimize "overlapping" the images, the next hologram is usually stored at least 3 to 4 nulls away.

The holographic system configuration which gives the smallest angular selectivity is the 90 ° geometry, which has an angular selectivity of about 0.007° for L of 4 mm. In this geometry the reference and image beams enter through orthogonal faces of the crystal, so $\theta_S = 0$ ° and $\theta_R = 90$ ° and the angular selectivity is given as

$$\Delta\theta = \frac{\lambda}{L}$$

Because of the high angular selectivity of the 90 ° geometry, we have chosen to use it in our experiments. A photograph of a holographic system configured using this geometry is shown in Figure 6-3.

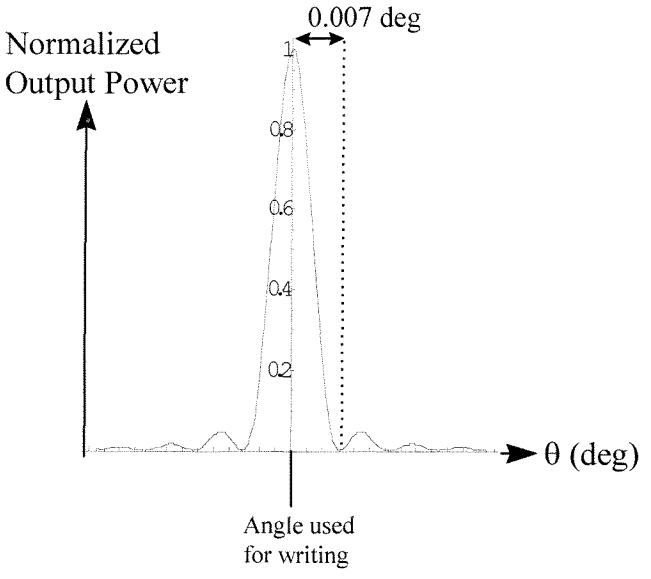

Figure 6-2: Output power of reproduced image beam as a function of reference beam angle away from the original reference beam angle used to write the hologram.

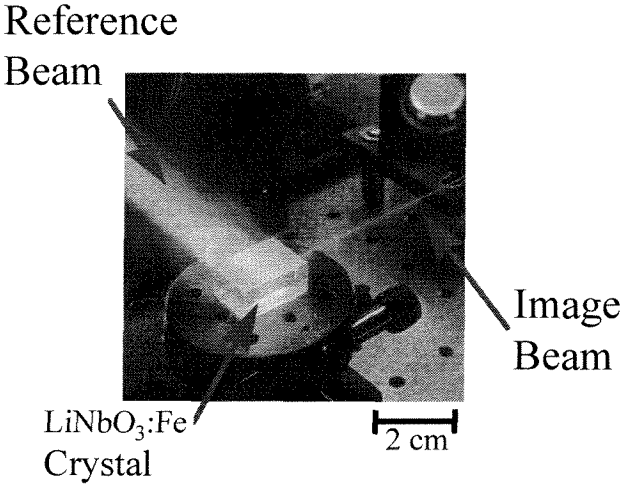

Figure 6-3: Photograph of hologram being written to crystal using the 90 degree geometry.

6.1.2 Scanning devices

To change the incident angle of the reference beam on the crystal, a scanning device is required. Conventional scanners that can achieve high accuracy are bulky and expensive. Two examples of such devices are mechanically rotated conventional mirrors, Figure 6-4, and acousto-optic deflectors (Figure 6-5). While current volume holographic storage systems are large in size, future applications will definitely require smaller holographic systems. Most components of current systems such as lenses and lasers can be readily reduced in size, but at present there are no commercial beam-steering devices that have the combined merits of low cost, small size and large angle of deflection. An emerging deflector technology which is based on liquid crystals addresses some of these limitations but is not well suited for providing a large number of deflection angles. Our devices, on the other hand, offer small size, low mass, large scanning angles, and potentially low cost. In addition, new holographic storage system configurations are possible using these actuators because they can be fabricated in arrays. Here we report results on the first use of flap actuators in holographic storage.

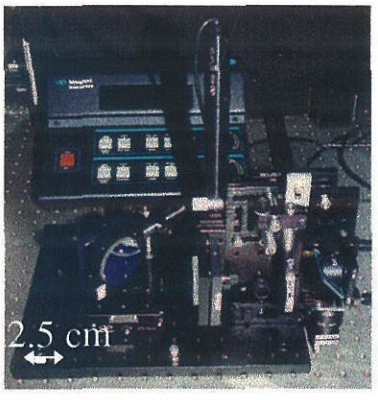

Figure 6-4: Inchworm scanning mirror.

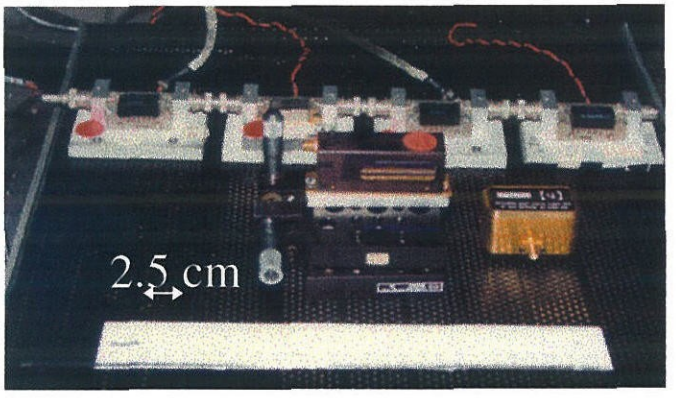

Figure 6-5: Accousto-optic deflector.

6.1.3 Actuator operation as scanning mirror

Two types of actuators were investigated as scanning mirrors for holographic data storage: the type-1a actuators and the type-3 actuators. Even though the type-1b actuators could be used for this application, we choose to concentrate on the type-1a actuators because they required smaller electromagnet currents.

Type-1a actuators:

The type-1a actuators' performance as deflectors in the angle multiplexing holographic data storage system shown in Figure 6-6 is investigated in this section. The actuator is placed on a solenoid electromagnet, which is driven by a current source to generate the desired magnetic field. In this system configuration a single argon laser beam is divided into a reference beam and an image beam. The information, to be stored in the crystal, is transferred to the image beam when the laser passes through a small liquid crystal display (LCD), which holds the image. The reference beam is deflected by the actuator, serving as a scanning mirror, and then passes through a lensing system which keeps the beam focused on the same location of the crystal, but with different incident angles determined by the actuator's deflection angle. The two laser beams intersect at the storage crystal, and the output beam is detected by a CCD camera. The volume nature of the holograms allows a page of data to be stored for each different deflection angle, provided that these angles are sufficiently separated. In this demonstration, we stored 100 holograms using a type-1a actuator. Some hologram reconstructions are shown in Figure 6-7. The hologram reconstructions are good quality reproductions of the original image. The evident concentric circles that show up on the retrieved images are an artifact of the crystal surface not being polished well, and not a product of the mirror surface quality. Although, in this case, each hologram was spaced from its neighbor by 0.143^{o}, deflections as small as 0.007^{o} could be generated with this actuator and the control circuit used. In practice, therefore, many more holograms can be stored using this setup.

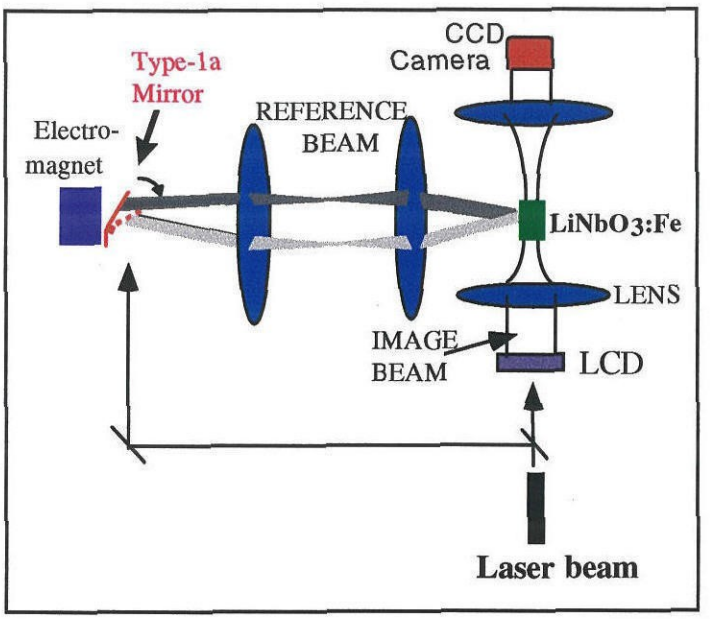

Figure 6-6: Angle multiplexing storage system using type-1a mirror.

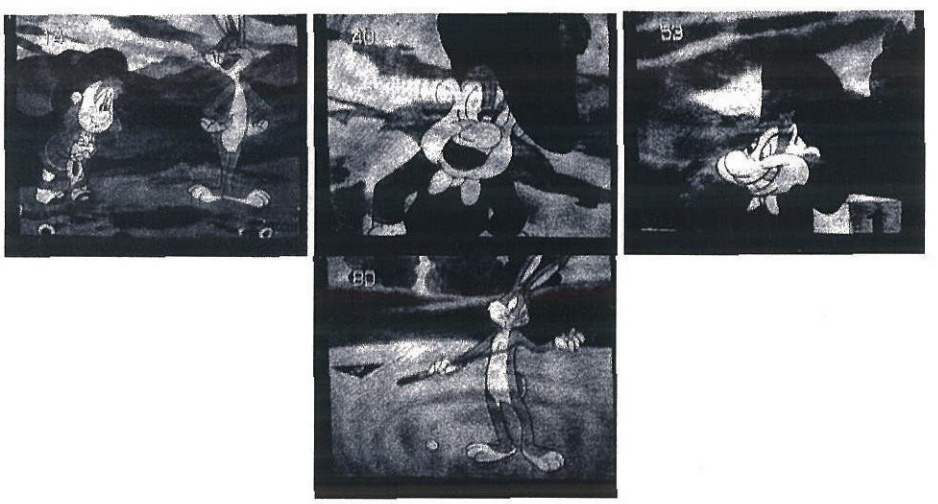

Figure 6-7: Four retrieved images stored as holograms using the type-1a actuator.

In this experiment we found that to improve the actuators response time, the actuator should be deflected in small angular steps by incrementally providing additional current to the electromagnet until reaching the desired actuator deflection angle. These small angle increments minimize the over-shoot and produce an overall faster mirror response. As an example, a deflection of 10.7 ° (0.187 rad), incremented

in steps of 0.7 ° (0.012 rad), could be performed in about 200 milliseconds. If the 10.7 ° jump was executed in one step, the actuator would ring for more than 400 milliseconds. We also investigated the angular repeatability of the actuator, that is, how accurately the actuator could return to a specific deflection angle. The type-1a actuator was deflected from 0 to 53 ° more than 20 times. Each time we found that the actuator returned to within 0.003 ° (64 μrad) of the 53 ° deflection angle. The angular stability of the actuator was also measured. The actuator was deflected to 53 °, and any change from this deflection angle over a 5 minute period was noted. The measured angular fluctuation of this actuator was less than 0.0006 ° (10 μrad). These last two measurements were performed using a STAR camera, a CCD camera with a pixel size of 23 μm. By locating the actuator 1.6 meters from the camera, and deflecting a laser beam off the mirror onto the camera, we were able to measure fine displacements, which were then converted to angular fluctuations.

Type-3 actuators:

To investigate the type-3 actuator, the device was first deflected to approximately 45 ° in a constant but non-uniform external field of about 200 Oe at the actuator, provided by a permanent magnet located 2 mm above the surface of the mirror. Deflections about this angle were induced by varying the coil current; a schematic of this process is shown in Figure 6-8. Two multiplexing schemes were explored. First the type-3 actuator was used in the same angle multiplexing storage system as the one in which the type-1a actuator was used. See Figure 6-6. The results were as successful as for the type-1a actuator, and Figure 6-9 shows some typical holograms stored and then retrieved using the type-3 actuator. In addition to the angular multiplexing scheme, the actuator was also used in a combined spatial/angular multiplexing configuration, Figure 6-10. Here, not only was the incident angle of the reference beam changed, but so was its position on the crystal. The primary advantage of this configuration is that two lenses can be eliminated and the actuator placed right

at the crystal surface. Once again for demonstration purposes we stored 100 holograms; all were of good quality.

Fixed angular increments of about 0.3 ° (5 mrad), for the type-3 actuator, were found to provide the shortest time to reach and settle on a particular hologram. Each 0.3 ° angle increment took ~ 25 milliseconds. In future work we plan to investigate other methods to improve the actuators response. Some possibilities include increasing the mechanical damping of the springs by coating them with "lossy" materials such as polyimide, increasing the spring stiffness, or shaping the driving input signals so as not to excite resonant modes. The type-3 actuator returned to within 0.002 ° (40 μrad) when the actuator was deflected multiple times, in this case from 0 to 2 °. Once the actuator was deflected to the above deflection angle, its angular stability was also measured. Any change from the above deflection angle over a 5 minute period was noted. Angular fluctuation for this actuator was less than 0.0006 ° (10 μrad).

As a conclusion, the flap actuators acting as MEMS scanning mirrors are a promising angle-multiplexing technology for holographic data storage. They possess a very large continuous deflection range, are compact, and use only moderate power. Though the two types of actuators performed equally well in their ability to store and retrieve holograms, in terms of operational versatility the type-3 actuator is more advantageous.

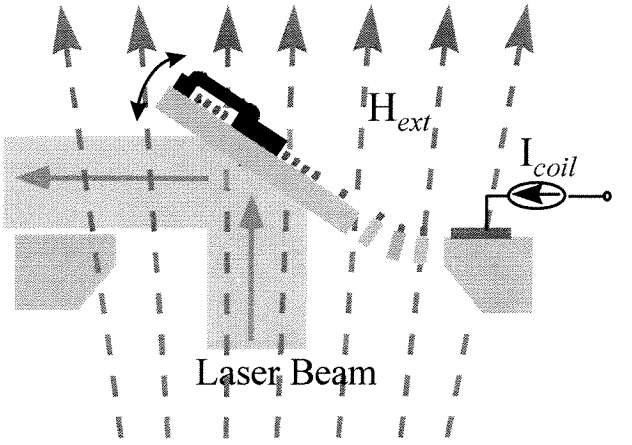

Figure 6-8: Schematic of type-3 actuator operating as a laser beam deflector. At a fixed external field, the mirror deflects to a fixed angle due to the permalloy. Deflections about this angle are then controlled by the applied current.

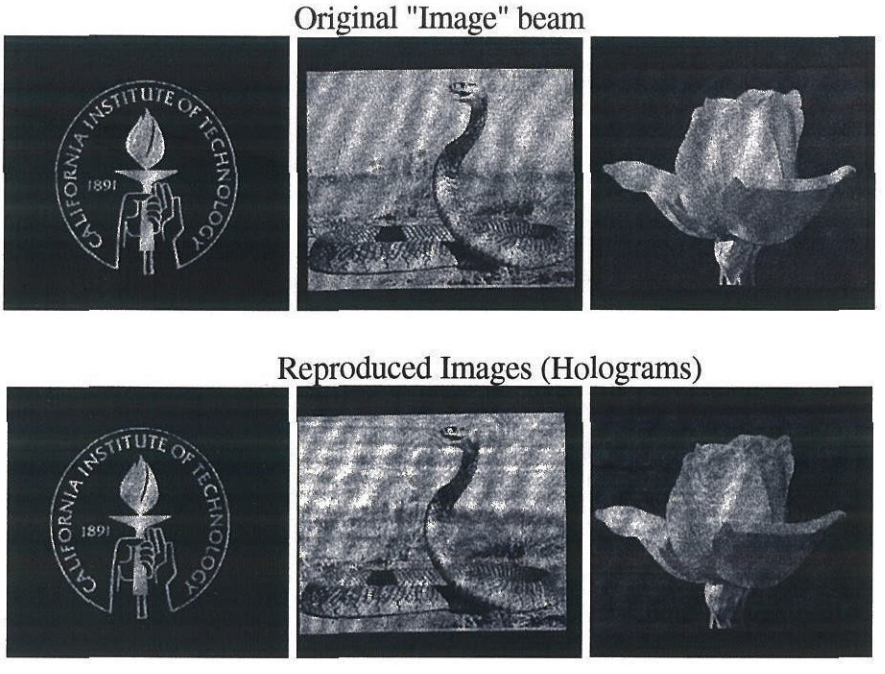

Figure 6-9: Original images and reproduced images which were stored as holograms in the crystal.

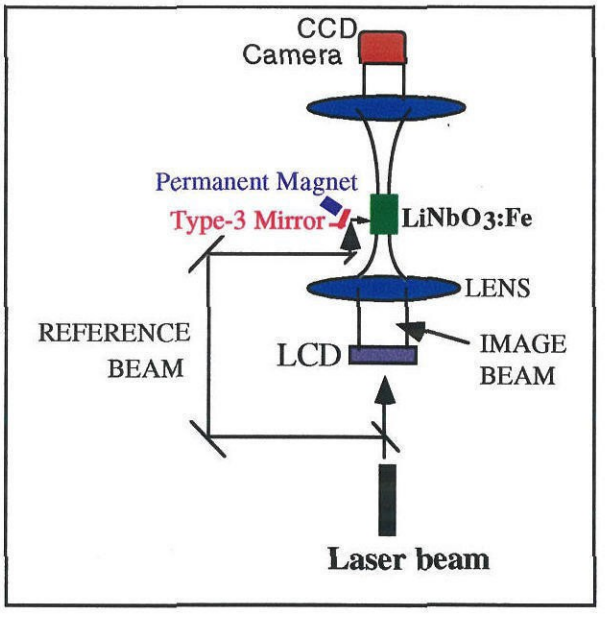

Figure 6-10: Compact holographic system configuration using the type-3 actuator.

6.1.4 Mirror quality and performance

For the type-1a actuator, the actuating permalloy layer is located on the bottom side of the plate. We designed it this way so the original silicon top surface can be used as the mirror surface. The highly polished silicon has a very small surface roughness of less than 10 nm over the entire mirror. However, the stress in the permalloy layer does cause the mirror to become slightly convex. This curvature depends on the magnetic field. While the measured horizontal radius of curvature is a constant of 7.5 cm, the vertical radius of curvature varies from 20 to 25 cm corresponding to a magnetic field from 0 to 20 kA/m. For thinner permalloy layers the radius of curvature is larger (greater than 75 cm for 5 μm thick permalloy) but does not change with field strength.

In the type-3 actuator, the top side of the silicon plate is occupied by the permalloy and coils so the bottom side of the silicon plate is used as the mirror. The bottom surface is slightly rougher, about 45 nm, because we use an epitaxy wafer in our process. It is found that this mirror is also convex with a curvature radius of 1 cm. Interestingly though, we observed no change in radius of curvature at field strengths up to 23 kA/m (300 Oe). Nevertheless, if necessary, the surface roughness and the curvature of the mirrors can be easily reduced using silicon-on-insulator (SOI) wafers. For our use of the actuators in laser holographic data storage, the imperfection of the mirror is not important. As long as the reflected beam off the mirror for a given angle is consistently reproducible, good quality holograms can be written and retrieved, as demonstrated above.

For evaluation purposes the flap actuators, acting as MEMS scanning mirrors, are compared with some commercial scanning devices as shown in table 6.1. The indicated hologram spacing for the commercial devices is better than the MEMS scanning mirrors. However, the objective of this study has been simply to demonstrate that the storage of approximately 100 holograms using the flap actuators is practical. Future work should be done to determine how closely, in angle, these holograms can be spaced using the actuators. The deflection range for both actuator types is larger than

either of the commercial devices. To reduce thermal effects produced by flowing current in the type-3 actuators, we can reduce the range of angular deflections produced by the on-board currents, and deflect the actuators to a larger extent by controlling the external magnetic field. The time response of the MEMS mirrors is significantly better than the commercial motorized inch-worm mirror, but worse than that of the acousto-optic deflector. MEMS scanning mirror response times can be further improved by increasing the resonant frequency of the actuators, which would compromise some of the large deflection range, or by increasing mechanical damping as mentioned previously. From table 6.1 it is apparent that using the MEMS scanning mirrors does significantly reduce the overall volume of the demonstrated holographic storage system. To further improve storage capacity, future work may include a design for a multi-MEMS-scanning-mirror array storage system.

Device	MEMS scanning mirror using type-1a actuator	MEMS scanning mirror using type-3 actuator	Commercial Motorized Inch-worm Mirror	Acousto-optic Deflector
Achieved hologram spacing	0.143°	0.03°	0.002°	0.0015°
Deflection range	60°	60°	35°	1.5°
Access time for 0.3° deflection	33 msec	25 msec	130 msec	70 μsec
Reference beam path volume*	100 cm^3	1 - 10 cm^3 **	686 cm^3	1372 cm^3
Device volume	5 cm^3	1 cm^3	60 cm^3	30 cm^3
Cost	Potentially low	Potentially low	Expensive	Expensive

* Not including laser.
** For compact configuration as in Figure 6-10.

Table 6.1: Comparison of the MEMS mirrors using flap actuators with commercial laser beam steering devices.

6.1.5 Summary and future work

Large angle deflection scanning MEMS mirrors have been successfully developed. The operation of scanning mirrors with permalloy only, and scanning mirrors combining permalloy and coils, has been demonstrated. The use of the mirrors has been successfully demonstrated in a holographic storage application demonstrating the feasibility of combining bulk micromachining with magnetic thin film actuation technology. A significant reduction in holographic system volume is achieved using the MEMS mirrors.

Future work issues include reducing the curvature of the MEMS scanning mirrors and improving the surface quality. The curvature of these scanning mirrors can be reduced by making the silicon plate thicker relative to the magnetic actuating layers, or by balancing the electromagetic actuating components so that they are symmetrically placed on both the top and bottom of the silicon plate, to provide stress compensation. Another way to reduce the curvature is to use a layer of elastic material such as silicon rubber between the plate and the electromagnetic components.

Another issue to investigate is how to configure the actuators for operation in arrays, positioned right up against the crystal. A conceptual drawing is shown in Figure 6-11. In this case, the design would be such that there would not be any permalloy on the actuators, only current carrying coils, so an individual actuator can be accessed by applying current only to it.

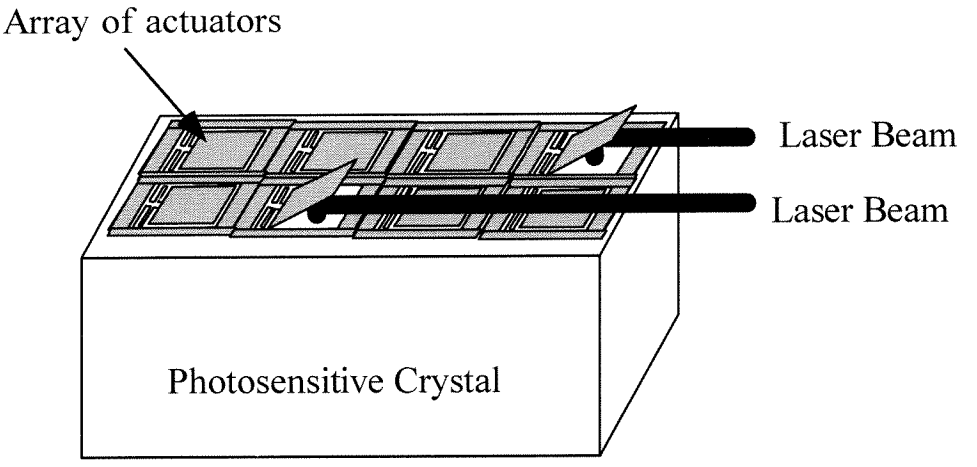

Figure 6-11: Conceptual drawing of future system configuration using an array of scanning mirrors positioned at a photosensitve crystal.

6.2 Electromagnetic MEMS 2 x 2 fiber optic bypass switch

6.2.1 Introduction

The emergence of high speed optical data communication networks and reliable compact optical sensor systems is creating a strong demand for fiber optic devices, particularly for fiber optic switches. At present, there is a strong need for small, fast, reliable, and low cost fiber optic bypass switches that can be used in high performance optical networks and systems. Fiber optic bypass switches are critical components that are used in optical networks to bypass one or more devices connected to the network without compromising network performance [3]. Commercial mechanical fiber optic bypass switches have existed for about 20 years but they are bulky, slow, sensitive to shock, and unreliable for high performance applications such as in aircraft and ship sensor networks and phased-array antennae control networks. The goal of this work is to develop a reliable bypass switch using MEMS technology. In the following, we show that this MEMS switch has been designed, fabricated, tested, and modeled. When compared to a DiCon switch, this MEMS switch is small (< 1 cm^3), fast (< 10 msec), and low power.

6.2.2 Switch design

The operating concept of the MEMS 2 x 2 fiber optic bypass switch is shown in Figure 6-12. A MEMS actuator, capable of large deflections, moves a thin double sided micromachined mirror up and down between the fibers. The four fibers (2 input, 2 output) are then positioned so that when the switch is activated (switch "on",) the MEMS actuator moves up about 300 μm, and places the mirror between the fibers, Figure 6-12a. In the "off" position the actuator is not activated and the mirror rests below the plane formed by these fibers (Figure 6-12b). This "off" position is called the "insertion" state. In this state, the optical signal from each input fiber is transmitted to the output fiber in front (Figure 6-12a). The activated state of the switch (switch on) is called the "bypass" state; now the optical signal from each input fiber is reflected off the mirror into the neighboring output fiber (Figure 6-12b). In this state two light paths each reflecting off the double-sided mirror are formed. The optical path that is connected to the device to be bypassed is called the loopback path, while the path connected to the rest of the network is called the bypass path.

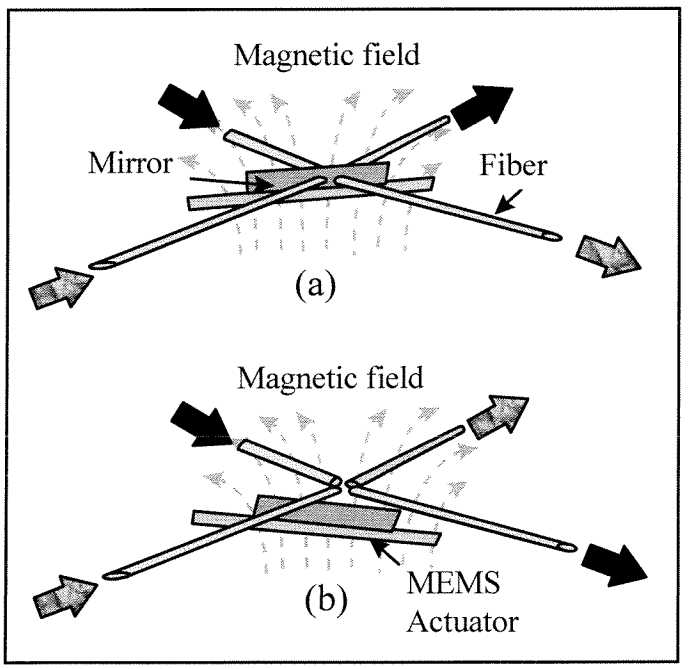

Figure 6-12: Bypass switch operation concept.

6.2.3 Switch fabrication

This novel switch requires the separate fabrication of an electromagnetic MEMS flap actuator and a micromachined double-sided mirror. The actuators used are the type-2 actuators, their fabrication was discussed in chapter 4, and the characterization of their operation was described in chapter 5. Although we detailed the fabrication of the actuator structure in chapter 4, we did not discuss the mirror fabrication process in detail. Here we describe the process steps required to fabricate the mirror.

The micromachined mirror, Figure 6-13, is fabricated from a <110> wafer. <111> planes in the wafer serve as the walls making up the mirror surface. In order to ensure that smooth <111> side walls are obtained, the mask used to define the mirror (mirror-mask) must be aligned to the <111> planes. The mirror-mask alignment to the <111> planes is done in two steps: first, alignment marks, aligned to the <111> plane, are made in the wafer as described in table 6.2, and then the mirror-mask is aligned to these alignment marks. Table 6.3 lists the processing steps for the mirror.

1) Coat wafer with a 5000 angstrom thick LPCVD silicon nitride layer.
2) Coat wafer with photoresist and pattern with alignment marks (see Figure 6-14). (These alignment marks consist of a series of grooves in the photoresist positioned at an angle of 0.1 degrees relative to each other as shown in Figure 6-14b.)
3) Reactive ion etch exposed silicon nitride until the silicon beneath is exposed.
4) Remove photoresist.
5) Etch exposed silicon in KOH for 90 minutes. (The silicon nitride serves as a protective mask while the silicon is etched. During etching the various planes of the silicon wafer are exposed, and some silicon under the nitride is also etched the silicon nitride will be undercut, as shown in Figure 6-14c. The smallest undercut will occur for the alignment mark closest aligned with the <111> silicon planes.)
6) Use alignment mark with least amount of undercut to fabricate the mirror.

Table 6.2: Steps to create alignment marks aligned to the <111> plane.

1) Once above alignment marks have been made, coat wafer with photoresist.
2) Align the mirror-mask to the alignment mark with least undercut and pattern the photoresist.
3) Etch the exposed silicon nitride until silicon is reached.
4) Remove photoresist.
5) Etch exposed silicon in TMAH to form a vertical ~ 270 μm high, 1.8 mm long, and 5μm thick, smooth silicon mirror.
6) Dice wafer into 1 mm × 3 mm rectangles each containing a mirror.
7) Coat the mirrors with a 30 nm gold layer to improve reflectivity.

Table 6.3: Mirror fabrication steps.

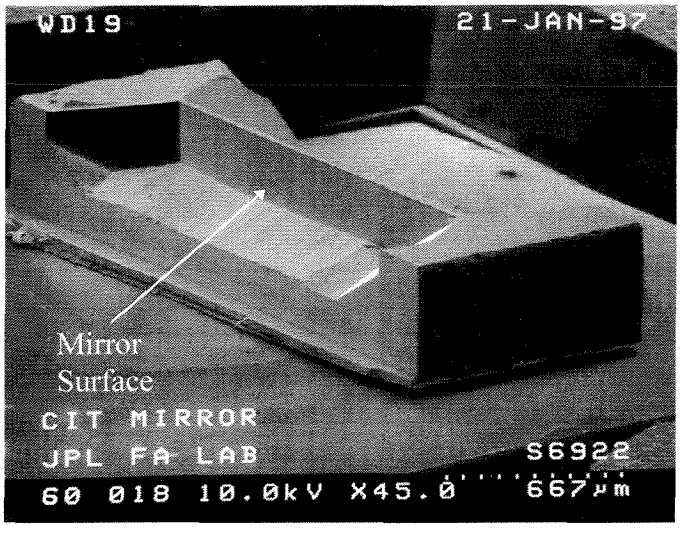

Figure 6-13: SEM of a fabricated micromachined mirror.

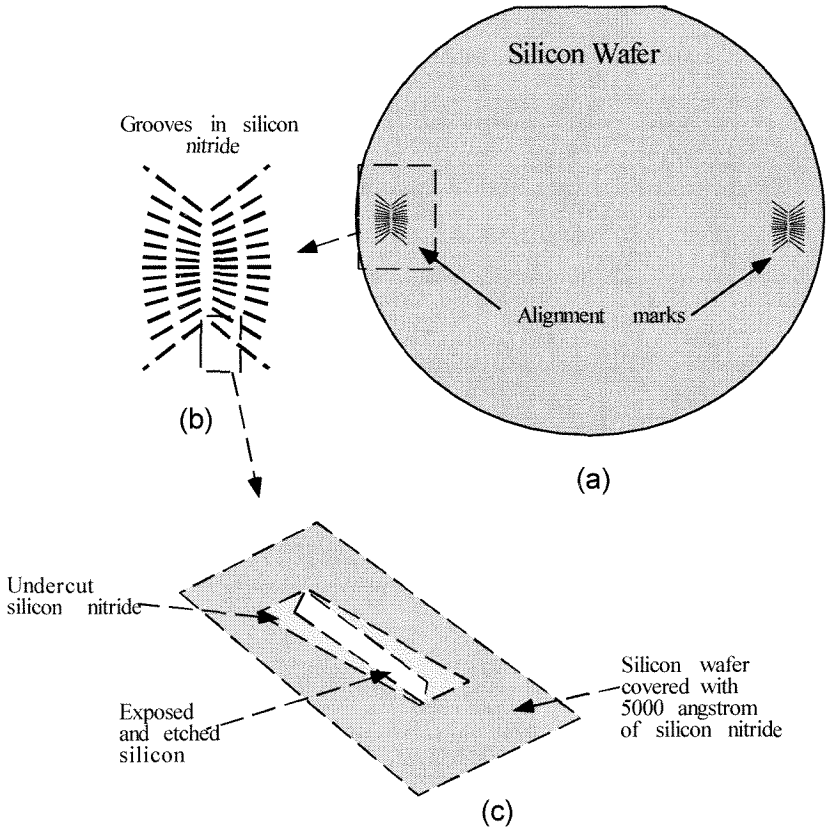

Figure 6-14: Alignment marks, for alignment of mask to silicon wafer's crystal planes. (a) Overall view of silicon wafer patterned with alignment marks. (b) The grooves formed in the silicon nitride are offset 0.1 degrees relative to each other. (c) Close up view of alignment mark after KOH etching. The amount of silicon undercut indicates how well the alignment mark is aligned with the <111> plane. The alignment mark with the smallest undercut is best aligned to the <111> plane.

Switch assembly entails attaching the mirror to the top side of the flap-actuator plate. Only one mirror is attached to the typ-2a (Figure 6-15) actuator while two mirrors are attached to the type-2b actuator as shown in Figure 6-16. The flap-actuators are placed coils down onto a rare-earth magnet and then put into custom packages. The custom packaging chosen, is glass garolite, a light weight, reliable, low cost material. Four multi-mode fibers, which have been lensed (fiber lens radius 62.5 μm), are aligned to the mirror and fixed to the package (figures 6-17 and 6-18). A photograph of a fully assembled and packaged switch is shown in Figure 6-19.

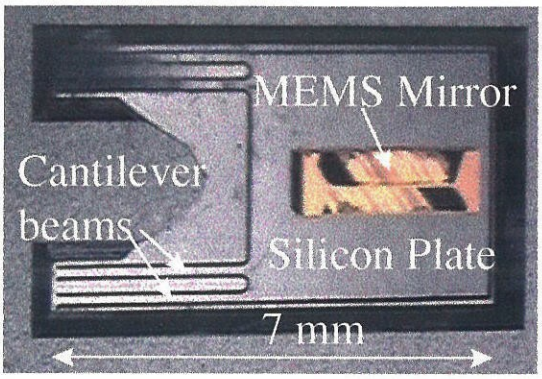

Figure 6-15: Photograph of cantilever, type-2a, actuator with mounted MEMS mirror.

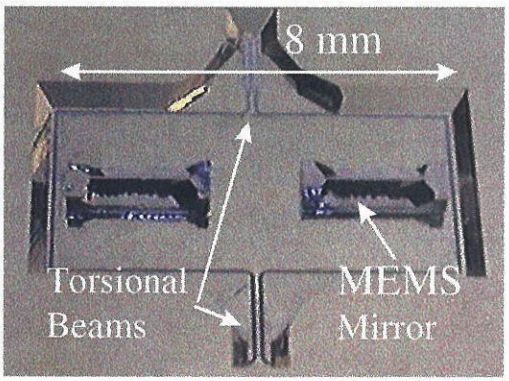

Figure 6-16: Photograph of torsional, type-2b, actuator with mounted MEMS mirror.

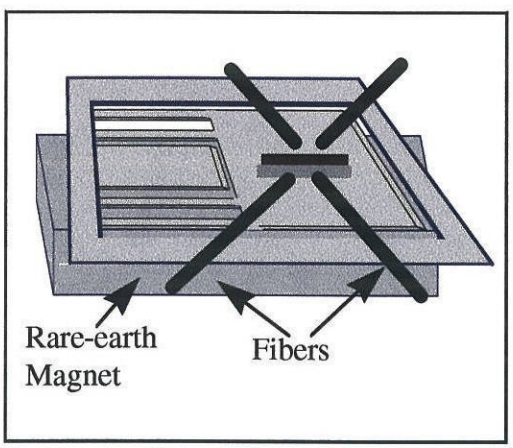

Figure 6-17: Schematic of assembled switch components.

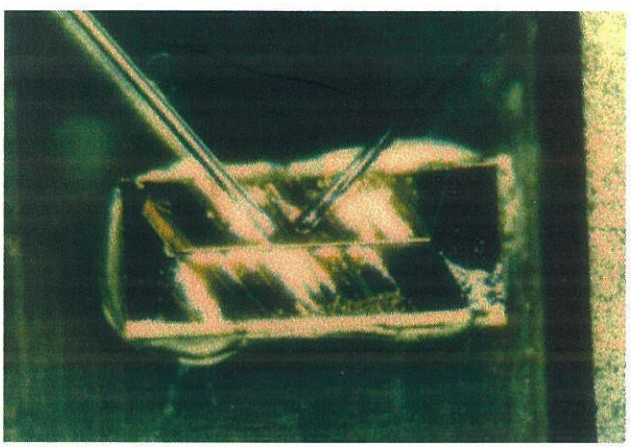

Figure 6-18: Photograph showing two fibers aligned to a 5 μm thick MEMS mirror.

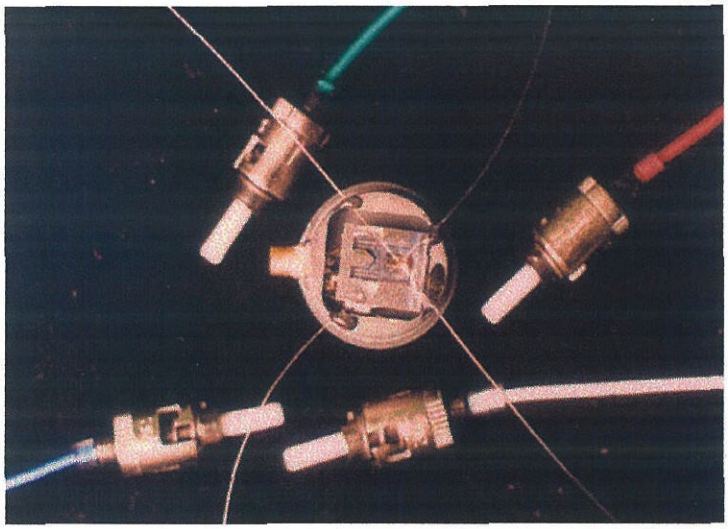

Figure 6-19: Fabricated and packaged bypass switch.

6.2.4 Switch performance

The deflection of the type-2 switches were characterized in chapter 5. The 200 to 300 μm deflections required for switch operation are achieved for the type-2a actuators at an applied current of about 30 mA. The currents required to produce these deflections using the type-2b actuators are also about 30 mA, with both coils operating. Note that in the case of the type-2b actuator the deflections shown in Figure 5-31 were obtained with only one set of coils actuated; these deflections can be doubled when two sets of coils are working.

The power required to activate the type-2a switch is between 17 and 38 mW. The type-2b actuator, by comparison, has a higher power consumption, around 110 mW, with two sets of coils working. When these switches are compared to a commercial fiber optic bypass switch made by DiCon, however, they still use less power. The DiCon switch requires about 130 mA when activated. The power consumption of the type-2 switches can be further reduced by using a stronger permanent magnet so the same deflections can be obtained at lower currents, or by making the coils thicker to reduce their resistance. The type-2b actuators power consumption can also be reduced by decreasing the stiffness of the torsional beam support.

The switching time was measured using the setup shown in Figure 6-20. Two fibers are positioned across the mirror at location PA, defined in Figure 5-31. A semiconductor laser is connected to one of the fibers. The second fiber is connected to a power detector, which is in-turn connected to an oscilloscope. The two fibers are aligned so that when the switch is off the light passes from one fiber to the other; when the switch is on the mirror moves up and blocks the laser light to the detector. This experiment was conducted only for the type-2a switch, and future measurements must be performed on the type-2b switch. The type-2b switch is stiffer than the type-2a switch. Therefore, it should have an even shorter switching time. The switch is driven with a square wave input signal at a frequency of 0.9 Hz. Figure 6-21 shows the turn-on and turn-off oscilloscope traces for the switch. The switch experiences some bounce during switching which limits the switching time for the type-2a switch to about 10 msec. However, this 10 msec switching time is a significant improvement over the DiCon switching time.

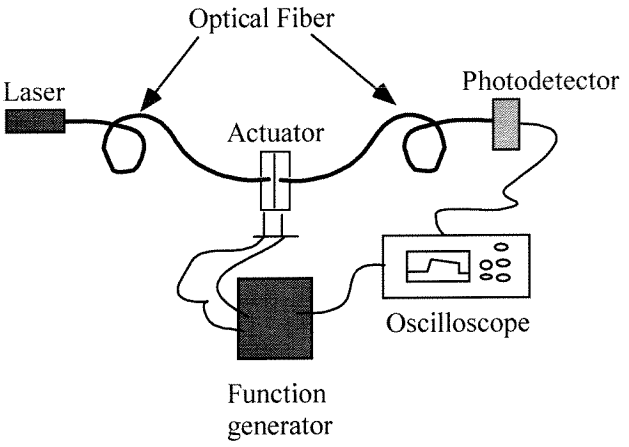

Figure 6-20: Switching time measurement setup.

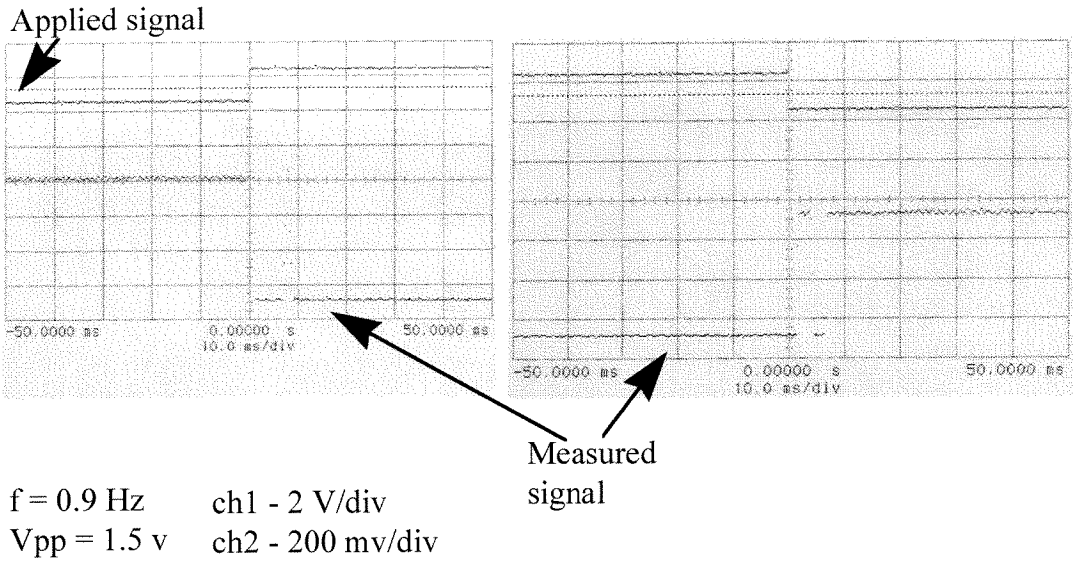

Figure 6-21: Oscilloscope traces of switching time measurements.

The signal power efficiency of the type-2a switch is measured using the setup shown in Figure 6-22. An 820 nm laser diode driven by either a DC current or a pulse modulated current is connected to one of the fibers as a light source, and a photodetector is connected to one of the remaining fibers to measure the received light. By properly changing the source and detector connections, the insertion losses and cross talk for all channels can be measured. At the same time, the switch conditions in either the insertion or bypass states are controlled by a DC current supply. Initial results are promising, as the maximum insertion loss measured is 3 dB while the bypass path loss is 2.3 to 2.5 dB. The loop back path loss is measured to be as high as 11 dB. A high loop back path loss is desired in order to eliminate any positive feedback effects, when the device to bypass is connected to itself.

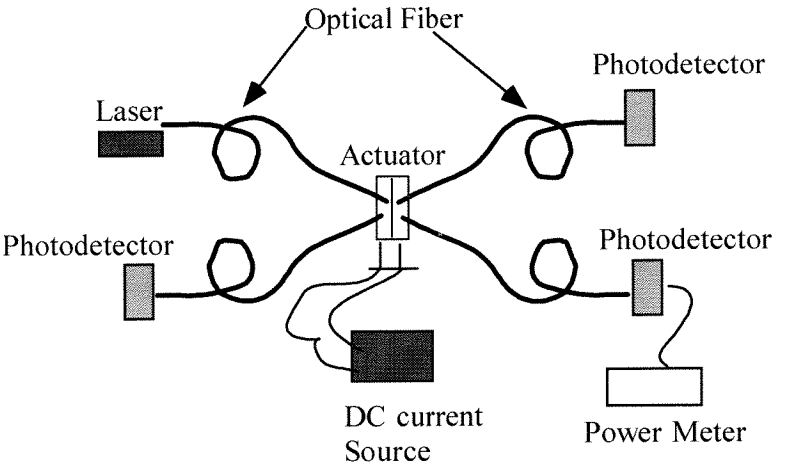

Figure 6-22: Experimental setup used to measure switch signal power efficiency.

In the future we hope to reduce the bypass path and insertion losses to less than 1 dB. There are several reasons that the current signal losses are relatively high these are due to the quality of the fiber lensing, the fiber alignment, and the roughness of the mirror. At present we are using relatively coarse fiber positioning tools to align the fibers. In the future we hope to improve the alignment using better tools. Although we expected that the mirrors would have a roughness of about 10 nm, the actual mirror roughness is higher, as is evident in the SEM photograph of the mirror shown in Figure 6-23. The roughness of the mirrors is around 80 nm. Further adjusting the etching parameters might help reduce the mirror roughness.

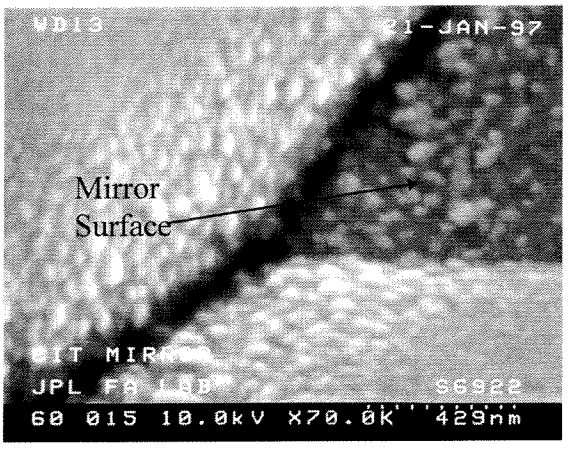

Figure 6-23: SEM picture showing roughness of mirror surface.

6.2.5 Discussion and future work

In Table 6.4 we compare the type-2a MEMS bypass switch to a commercial DiCon switch. In terms of switching time, power consumption, and switch size the MEMS switch is much improved over the DiCon device. Nevertheless, the loopback path and bypass path losses can and should be further optimized. Improvements in switch signal power efficiency involve increasing the alignment accuracy of the fibers, better fiber lensing, as well as developing even thinner and smoother mirrors. Shock resistance is another important consideration for these switches. Specifications require the switches to survive 20 g. While the cantilever type switch has difficulty meeting this specification, the torsional type switch easily survives 20 g. In conclusion, the fiber optic bypass switch presented here offers a practical MEMS solution for the development of small, inexpensive, fast bypass switches which are imperative for high performance optical networks.

	MEMS Fiber Optic Bypass Switch	Commercial DiCon 2x2 Multimode Fiber Optic Switch
Switching Time	8 msec	20 msec
Switching Current	20-30 mA	130 mA
Switching Power	17- 38 mW	650 mW
Switch Size	$< 1\ cm^3$	$23\ cm^3$
Insertion Loss	62×10^{-3} dB - 3dB	0.5 dB - 1 dB
Loopback Path Loss	2.5 dB - 11 dB	2 - 6 dB
Bypass Path Loss	2.3 dB - 2.5 dB	0.5 dB

Table 6.4: Comparison between a commercial DiCon fiber optic switch and our micromachined switch.

6.3 Additional applications

The technology used to fabricate the flap type actuators can be applied to many additional devices. Some possible applications are discussed in this section.

One device based on a variable reluctance magnetic circuit is a micro-motor for disk-drive head positioning. The motivation for developing this actuator is the ever increasing demand for higher data storage densities. Since 1991, track densities of magnetic recording rigid disk drives have gone up approximately 30% each year. In 1995 the track density was around 5,000 tracks per inch, and it is projected to be around 25,000 by the year 2001 [4]. Such a high density requires track to track spacing of 1 μm, with the allowable off-track error less than 120 nm. Figure 6-24 shows a schematic of the components of current hard disk-drives. These include a voice-coil motor, a suspension (load beam) and slider bearing, composed of a slider and gimbal. The gimbal provides a spring suspension for the slider while the slider holds the read/write head. Tracking bandwidth for these drives is less than 600 Hz limited primarily by the voice-coil motor. For 25,000 TPI, the estimated tracking bandwidth will need to be higher than 3 kHz. This level of performance, however, can not be achieved by using or improving on existing hardware. One way to increase the tracking bandwith is to add a dual-stage, piggyback, microactuator, so that a voice coil motor is used to do coarse positioning, while a micromachined actuator mounted above the head can provide fine position control, as shown in Figure 6-25.

Some initial work was done towards developing a prototype actuator. The actuator proposed uses electromagnetic actuation to provide the fine positional control for the disk drive head. This actuator is based on a variable reluctance magnetic circuit. Two U-shaped permalloy cores are located on either side of a movable permalloy core, which is supported by planar serpentine springs. One set of current carrying copper coils wraps around each of the U-shaped cores. When current is passed through one set of coils, the movable permalloy core is pulled towards this U-shaped core, minimizing the reluctance

of the circuit. When the slider is then attached to the movable permalloy core, the read/write head position can be controlled.

Due to technology constraints at the time, a working device was not achieved. The major difficulty was in forming the spring structure, and in preventing the photoresist from cracking. The spring design for these actuators required that the spring be stiff out of plane and soft in-plane. This requires the springs be much thicker than they are wide, an aspect ratio which could not be achieved, under the given geometrical constraints, using standard RIE etching. Today with the development of new techniques known as deep RIE, the desired spring aspect ratios can be achieved. With further effort these actuators should be realizable, and if successfully fabricated the market for these devices is huge.

A second possible application of the electromagnetic MEMS technology is towards developing electromagnetically actuated relays and switches. The idea is again to form a variable reluctance circuit, consisting of a permalloy core with copper coils wrapped about it, and a moveable permalloy piece which can serve to open or close an electric contact providing a path for current to flow. The advantage of using MEMS to make the relay is improved reliability, reduced cost, and ability to directly integrate these relays with controlling electronics. The electromagnetic actuation provides the device with large forces which reduce the contact resistance and permit high standoff voltages.

A third possible application is the development of on chip inductors and transformers, which can be useful in many analog applications. These integrated inductors and transformers should reduce the noise in as well as the physical size of the circuit.

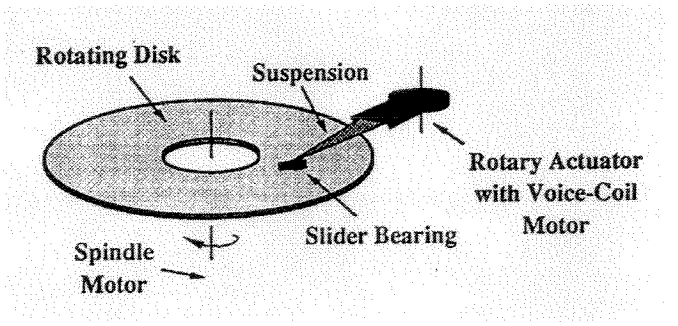

Figure 6-24: Electromechanical components for a commercial magnetic recording rigid disk drive.

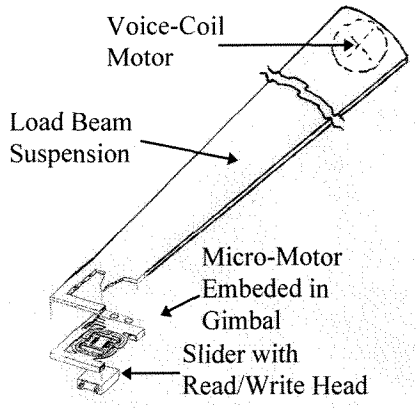

Figure 6-25: Dual-stage actuator disk drive configuration.

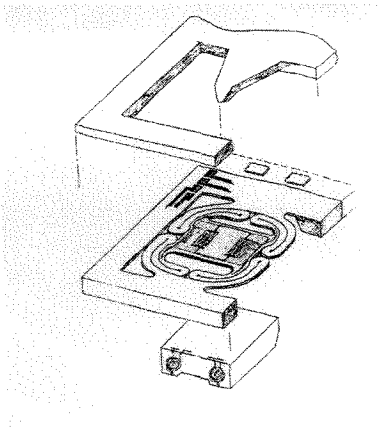

Figure 6-26: Enlarged view of micro-motor assembly.

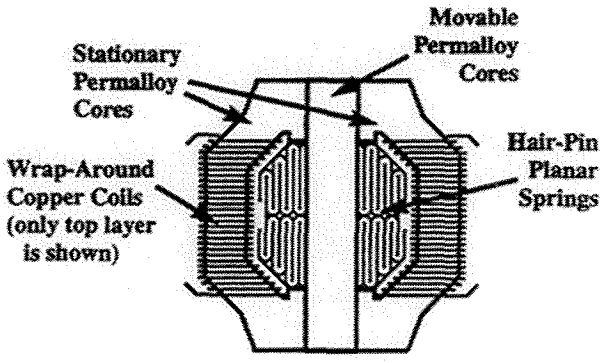

Figure 6-27: Proposed design for micro-motor.

Figure 6-28: SEM of fabricated micro-motor.

References

[1] D. Psaltis and F. Mok, " Holographic Memories," *Scientific American*, pp. 70 - 76, Vol. 273 (5), 1995.

[2] G. W. Burr, F. H. Mok and D. Psaltis "Large scale volume holographic storage in the Long Interaction Length Architecture," *SPIE proceedings, paper 2297-47*, (1994).

[3] S. E. Miller and I. P. Kaminow, *Optical Fiber Telecommunications II, Academic Press*, 1988.

[4] W. Tang, V. Temesvery, R. A. Miler, et al., "Silicon Micromachined Electromagnetic Microactuators for Rigid Disk Drives," *IEEE Transactions On Magnetics*, Vol. 31 (6), November 1995.

Appendix A

Fabrication Processes Of Selected Flap Actuators

A.1 Type-1b actuator fabrication steps

1. Wafer preparation

- Make double side alignment marks using double side alignment jig.
- Standard wafer cleaning using piranha (H_2SO_4: H_2O_2 = 5:1) 120 °C 10 min.
- 5% HF dip (100 ml H20: 10 ml HF).
- Oxidize wafers1050 °C 7 drops/min H_2O (5000 Angstrom).

2. Backside oxide patterning and etching

- 2 min HMDS priming.
- Spin AZ 1350J photoresist at 3 Krpm for 40 sec, resist thickness 2 μm.
- Softbake 30 min in convection oven at 90 °C.
- Expose 0.5 sec using **mask #1**.
- Develop wafer 2 min 100% AZ developer.
- Hardbake wafers 120 °C 30 min.
- BHF etch oxide to expose silicon (~ 1000A/min) (~ 7 min).
- Strip photoresist in acetone alcohol and DI water (spin dry).

3. Membrane formation

- EDP etch to form membrane.
- Strip B+ layer with HNA (1-3-8).
- Strip Oxide in BHF.

4. Oxidation and permalloy mold formation

- Reoxidize wafer to get 5000A of SiO_2.
- Evaporate seedlayer on front side of wafer: Ti / Cu seedlayer (100A / 800 A).

- Pattern front side of wafer with AZ 4400 photoresist (in two coats) **mask #2**.

5. Permalloy electroplating

- Electroplate permalloy, 5 micron thick, 8-10 mA/cm^2, 23 °C.
- Remove photoresist, globally UV expose wafer and develop for 2 min in AZ developer.
- Remove seedlayer using copper and titanium etchants.

6. Wafer patterning for RIE etching

- Coat wafer with AZ 4620 photoresist, ramp from 0 => 2 Krpm over 1 min.
- Bake 100 °C for 30 min.
- Cool 5 min.
- Repeat for second coat.
- Expose photoresist for 4 seconds (**mask #3**).
- Develop in 1:3 AZ 400K / H_20 for < 3 min.
- Rinse 1.5 min in DI water.
- Before drying, BHF etch exposed oxide.

7. RIE etch wafer in SF_6+ O_2

8. Dice wafer.

A.2 Type-2b actuator fabrication steps

1. Wafer preparation

- Start with a double side polished <100> silicon wafers.
- Make double side alignment marks using double side alignment jig.
- Standard wafer cleaning using piranha (H_2SO_4: H_2O_2 = 5:1) 120 °C, 10 min.
- 5% HF dip (100 ml H20: 10 ml HF).
- Oxidize wafers (9 Hours) 1050 °C, 7 drops/min H_2O. 2 micron thick.

2. Backside oxide patterning and etching

- 2 min HMDS priming.
- Spin AZ 4400 3krpm for 40 sec.
- Bake 5 min on hot-plate at 90 °C.
- Expose 1.5 sec using **mask #1**.
- Develop wafer 1 min 30 sec. 1 part (40ml) AZ 351 : 3.5 parts (140ml) H20.
- Hardbake wafers 120 °C for 15 min.
- BHF etch oxide to expose silicon (~ 1000A/min) (~ 24 min).
- Strip photoresist in acetone alcohol and DI water (spin dry).

3. Membrane formation

- KOH etch wafer to form 30 micron thick membrane.
- KOH etch at 58 °C for ~ 20 hours.
- Strip Oxide in BHF.

4. Electrical isolation and mold formation for copper coils

- LPCVD Si_xN_y deposition 2000A.
- Evaporate Cr / Cu seedlayer (100 A / 800 A).
- HMDS priming for 2 min.
- Coat AZ4400 spin 2 krpm 40 sec.

- Bake on hot-plate 5 min at 90 °C.
- Allow to cool for 3 min, then repeat above photoresist steps.
- Expose 3.2 sec and develop for 2 min.

5. 1st layer copper coil electroplating

- Electroplate 3-6 micron copper (I = 192 mA).
- Globally expose wafer and develop, DI water rinse.

6. Seedlayer etch

- Etch seedlayer: 100ml H2O :50ml HCL ~ 30 sec.

7. Insulator deposition and patterning

- Deposit 1.6 micron LTO.
- Deposition time 200 min. (adjust time for 1.8 micron).
- Pattern both front and backside LTO (**mask #3 and mask #4**).
- Coat wafer backside with PR and coat wafer with AZ 4400 @ 2000 rpm 40 sec. Bake on Al plate @ 90 °C 5 min. Cool 5 min. Expose 3 sec. Develop in AZ 351 40ml: 140ml H20. Expose 3.2 sec. Develop 1 min 45 sec.
- Hardbake by placing in oven 90-120 °C (for 6 min).
- Do descum, 200mtorr O_2 : 45 sec : 200mWatts.
- HMDS 2 min for wafer.
- Place wafer backside up and spin AZ4400 2k 40 sec.
- Bake 90 °C 5 min on hot plate.
- Etch LTO for backside.
- Etch LTO 12 min.
- Pattern front side of wafer: HMDS 2 min.
- Spin AZ 4400 2krpm 40 sec.
- Bake on hot plate at 90 °C for 5 min.
- Expose 2 sec develop 2 min in AZ351 40ml: 140ml H_2O.
- DESCUM Wafer 200mtorr O_2 for 45 sec 200mW.

8. 2nd layer copper coils formation

- Evaporate Ti/ Cu seedlayer.
- HMDS priming 2 min.
- Spin on AZ 4400 2krpm 40 sec bake on hot plate 5 min 90 °C, repeat.
- Expose 3.2 sec using (**mask #5**), develop 1 min 50 sec in AZ351 1part: H20 3.5 parts.
- Etch exposed copper in 100 ml H_20 : 5 ml H_20_2: 5ml acetic acid.
- Etch exposed Titanium in HF.
- Re-expose wafer to pattern conductors (**mask #6**). Expose 3.2 sec, develop 1 min. 50 sec.
- Electroplate top copper conductors 9 microns thick
- Strip seedlayer (etch Ti / Cu). Use standard recipes.

9. Preparation steps for RIE etching

- HMDS 2ml 2 min.
- Spin on AZ 4620 photoresist, ramp from 0 to 2krpm over 1 min.
- Bake at 98 °C for 28 min.
- Do EXPO (possible starting exposure ~10sec) (**mask #7**).
- Develop 3.2 min. In AZ 351 40 ml: H_20 140ml.
- Plasma descum 5 min. 300mtorr 300 Watts.
- Hardbake wafer 90 °C 20 min, and then at 95 °C for 20 min, at 100 °C for 20 min, 105 °C 20 min, and 110 °C for 10 min.

10. RIE etching using SF_6 and O_2.

11. Dice wafer.

12. Strip Photo Resist.

A.3 Type-3 actuator fabrication steps

1. Wafer preparation

- Make double side alignment marks using double side alignment jig.
- Standard wafer cleaning using piranha (H_2SO_4: H_2O_2 = 5:1) 120 °C 10 min.
- 5% HF dip (100 ml H20: 10 ml HF).
- Oxidize wafers1050 °C 7 drops/min H_2O (5000 Angstrom).

2. Backside oxide patterning and etching

- 2 min HMDS priming.
- Spin AZ 1350J photoresist at 3 Krpm for 40 sec, resist thickness 2 μm.
- Softbake 30 min. in convection oven at 90 °C.
- Expose 0.5 sec using **mask #1**.
- Develop wafer 2 min 100% AZ developer.
- Hardbake wafers 120 °C 30 min.
- BHF etch oxide to expose silicon (~ 1000A/min) (10 min).
- Strip photoresist in acetone alcohol and DI water (spin dry).

3. Membrane formation

- EDP etch to form membrane.
- Strip B+ layer with HNA (1-3-8).
- Strip Oxide in BHF.

4. Electrical isolation and mold formation for copper coils

- Reoxidize wafer with 5000 Angstrom SiO_2.
- Evaporate Ti / Cu seedlayer (100 A / 800 A).
- HMDS priming for 2 min.
- Coat AZ4400 spin 2 Krpm 40 sec.
- Bake on hot plate 5 min at 90 °C .

- Allow to cool for 3 min, then repeat above steps.
- Expose 3.2 sec and develop for 2 min using **mask #2**.

5. copper coil electroplating

- Electroplate 9 micron copper (I = 192 mA).
- Globally expose wafer and develop, DI water rinse to remove photoresist mold.

6. Seedlayer etch

- Etch Cu in 100ml H_2O: 5 ml acetic acid: 5 ml H_2O_2.
- Etch Ti in BHF

7. Insulator deposition and patterning

- HMDS priming.
- Spin on AZ 4400 photoresist at 2 krpm for 40 sec.
- Softbake 30 min in convection oven at 90 °C .
- Allow to cool for 5 min.
- Expose using **mask #3**.
- Hardbake in nitrogen oven.

8. Seedlayer and mold formation for permalloy electroplating

- Evaporate seedlayer on front side of wafer: Ti / Cu seedlayer (100A / 800 A).
- Pattern with photoresist (same as step 5) using **mask #4**.

9. Permalloy electroplating

- Electroplate permalloy 8-10 mA/cm^2, 23 °C (11 μm thick).
- Remove photoresist, globally UV expose wafer and develop for 2 min.
- Remove seedlayer.

10. Wafer patterning to define springs and plate

- Coat wafer with AZ 4620 photoresist, 2 Krpm over 1 min.
- Bake 100 °C for 30 min.
- Allow to cool for 5 min.
- Repeat for a 2nd coat.

- Expose for 4 seconds using **mask #5**.
- Develop in 1 : 3 AZ 400K : H_2O for < 3 min.
- Rinse 1.5 min.
- BHF etch for 8 min to remove exposed oxide.

11. RIE etch wafer in O_2 and SF_6.

11. Dice wafer.

12. Strip AZ 4620 Photo Resist.